Tel-Aviv University

Raymond and Beverly Sackler Faculty of Exact Sciences

Diffusing Alpha-emitters Radiation Therapy (DART)

Comparative Study of different Experimental Models of treated solid tumors

Thesis submitted as part of the requirements for the M.Sc degree at Tel-Aviv University, School of Physics and Astronomy

By:

Hadas Raviv (Bittan)

Carried out under the supervision of:

Prof. Kelson Itzhak, School of Physics and Astronomy, Raymond and Beverly Sackler Faculty of Exact Sciences, Tel-Aviv University, Tel-Aviv, Israel

Prof. Keisari Yona , Department of Clinical Microbiology and Immunology, Sackler Faculty of Medicine, Tel-Aviv University, Tel-Aviv, Israel

September 2009

Contents

List of Figures

List of Tables

Abstract

Alpha-particles are a form of high-LET radiation, depositing several MeV over a range of 40-90 μm. This makes them highly effective against cancer cells, with only a few alpha particle traversals through the nucleus required to induce cell death. However, alpha-radiation is not used clinically for treating solid tumors today. The reason is that the particles short range requires a direct insertion of closely spaced alpha sources into the tumor which is generally impractical.

Diffusing Alpha-emitters radiation therapy (DART) is a new proposed method which was developed in our group and allows the treatment of solid tumors by alpha particles. Rather than a source that emits alpha-particles, we insert into the tumor a source that continuously releases alpha emitting atoms. These atoms spread in the tissue, leading to the formation of a region of a therapeutic high-LET dose through their alpha decays.

Experimental work conducted in our lab showed that the response for DART treatment might differ between tumor types. Specifically, treatment of mice bearing a squamous cell carcinoma tumor model (SQ2) with a single DART source resulted in a significant tumor growth retardation while treatment of mice bearing a pancreatic tumor model (PANC2) showed poor response.

The purpose of the present work was to measure the intra-tumoral spread of radioactivity, the resultant necrotic damage and the radioactive atoms leakage out of three mouse tumor models - SQ2, PANC02 and LL2. It was found that the distribution of the alpha-emitting isotopes released from DART source and the necrotic damage correlate with the degree of the tumor growth retardation as a result of treatment. The widest radiation distribution and necrotic areas were observed in SQ2 tumors and the smallest in PANC02 tumors. In addition, the leakage of the radioactive isotopes out of the tumors was found to be highest in PANC02 tumors.

Chapter 1

Introduction

1.1 Radiation therapy for solid tumors

Cancer is one of the leading causes for mortality over the world these days. In the United States, cancer accounted for nearly one quarter of deaths in 2006, exceeded only by heart diseases [9]. In the UK one in four people died from cancer in the last few years and in Israel, one in five. Treating cancer is therefore one of the biggest challenges of medicine today. Many different treatment methods ranging from local treatment procedures such as surgery and radiation therapy to systemic procedures such as chemotherapy already exist. Still, due to the high mortality rate, the ongoing research is very extensive and broad, aiming to develop new approaches for treatment or to improve existing ones.

Cancer is actually a collection of diseases with a common feature of uncontrolled growth. Lung, prostate, colon, pancreas and breast cancers are examples of the most familiar and lethal cancer types. The diversity of cancer types is one of the reasons that cancer treatment is such a major challenge. The reaction of different tumor types to the same treatment can vary between complete cure and total failure. Moreover, the same tumor type in different disease stages may require a completely different treatment approach. For example, pancreatic tumor is resistant to many types of chemotherapy drugs that are used in curing other tumor types. The treatment of this cancer with chemotherapeutic drugs is limited to gemcitabine and 5-Fluorouracil (5-FU). In addition, complete removal of this tumor at its early stages by surgery is possible by using a special procedure. In later stages, when the tumor invades its surroundings, surgery might improve the quality of life but does not usually result in cure [20, 5].

Radiation therapy is one of the major modalities in cancer treatment representing the use of ionizing radiation to destroy the cancerous cells. It is primarily used for treating solid tumors. Radiotherapy may be used as a curative treatment, adjuvant treatment, palliative treatment (where cure is not possible and the aim is for local disease control or symptomatic

relief) or as therapeutic treatment (where the therapy has survival benefit and it can be curative). Also, it can be given alone or combined with other treatments such as surgery or chemotherapy. The precise treatment intent and procedure depend on the tumor type, location and stage, as well as on the general health of the patient.

In radiation therapy the dose is defined as the energy deposited per unit mass of the irradiated tissue (measured in Gray (Gy) in SI units). Generally, an attempt is made to maximize the dose administered to the malignant tissue while minimizing the dose to other regions. A distinction is made between external radiotherapy, where the irradiation source is situated outside the patient (usually either gamma-rays, x-rays, electrons, neutrons or charged particle beams are used) and brachytherapy, where the radioactive source is situated inside the patient in order to enable a higher localized dose. Brachytherapy treatment is usually conducted by placing sealed radioactive sources inside the tumor. Also, it can be performed by using unsealed sources - radioactive compounds that are injected into the blood stream and reach the tumor through it.

An important difference between radiation treatment types relates to the radiation type used. The linear energy transfer (LET) of a given radiation type is defined as the spatial rate of energy deposition along the path of the radiation inside the tissue. Radiation treatments utilizing photons and electrons are classified as low-LET treatment. This is because the radioactive particles damaging the tissue in both cases - electrons (released in ionization events following irradiation by gamma or x-rays) - are characterized by a typical LET of 0.2-2 $keV/\mu m$. Treatments utilizing alpha particles, having a typical LET of 100-200 $keV/\mu m$ are characterized as high-LET treatments.

High-LET radiation is generally more effective against cancer cells than low-LET radiation, achieving a higher degree of cell kill probability for a given absorbed dose. This results from the differences between the mechanisms creating the cell DNA damage as a result of these radiation types. Low-LET radiation passage through the tissue leads to the ionization of water molecules and to the formation of free radicals in the tissue that damage the DNA. This usually results in a single strand break or a simple strand break in the DNA that can be repaired with a high probability. In contrast, high-LET radiation creates direct damage to the DNA by passing through the nucleus. This results in complex DNA lesions that are very difficult to repair. Another important reason for the higher probability of high-LET radiation to cause a cell death is that its effect does not depend on the cell oxygenation state. Oxygen plays an important role in the formation of free radicals. Therefore hypoxic cell are resistant to low-LET radiation while the effect of alpha particle on these cells almost does not change [6, 7].

Despite of the alpha radiation advantage in causing cell damage, so far very little clinical use was made with these particles against solid tumors. This stems from the fact that the range of these particle is too short, limited to several dozen microns in tissue. In order to

be used alpha sources should be brought into the target area and spaced very close to one another (less then 0.5 mm). This is actually impractical. The only investigated treatment using alpha radiation today is called alpha-radioimmunotheraphy. In this treatment alpha emitters are attached to a molecule or to a monoclonal antibody that targets or seeks out specific tumor cells in specific organs of the body. The emitters should release their energy after reaching to the tumor, in the vicinity of the cancerous cells leading to their death. This treatment is considered to be best against isolated cells, small clusters and small metastases [14].

1.2 DART basic idea

A new method for treating solid tumors with alpha particles, DART - Diffusing Alpha-emitters Radiation Therapy, was developed and tested in our lab in the last few years [14, 15, 24]. The basic idea of DART is to insert into the tumor a radioactive wire impregnated with small activities of a parent alpha-emitting isotope which continually releases its short-lived alpha emitting daughter atoms from the source surface. The atoms are released from the source by recoil during the radioactive decay of the parent atom which is embedded closely below the source surface. When a radioactive atom emits an alpha particle in one direction (with an energy of 6 - 9 Mev), its daughter atom recoils in the opposite direction with a kinetic energy of about 100 - 170 Kev. This energy enables the atom to traverse about 10 - 30 nm in the tumor. After entering the tumor the released atoms can spread by the combined effect of thermal diffusion and convection.

According to information gathered so far, the atoms released from the source lead to the creation of a biologically significant dose over a region measuring a few mm in size in the tumor. Also, considerable cell damage is detected in this region. The DART method therefore overcomes the limitation that prevented the use of alpha radiation for treatment so far - the extremely short range of alpha particles in matter. This becomes possible thanks to the intermediate agents - the short lived daughter atoms released from the source. After entering the tumor, these agents, named the 'diffusing atoms', take the alpha particles away from the source, extending significantly the region exposed to high-LET radiation.

The DART idea is implemented by using the alpha decay chain beginning with thorium-228 (^{228}Th, 1.91 y half life) presented in figure 1.1. The ^{228}Th long-lived isotope is used as a generator to produce radium-224 (^{224}Ra, 3.66 d half-life) bearing sources. The source, a thin conducting wire, is treated by a special procedure (described in chapter 2) in order to enable considerable release of ^{224}Ra daughters and prevent the ^{224}Ra itself from leaving the source. radon-220 (^{220}Rn, 55.6 s half-life), polonium-216 (^{216}Po, 0.15 s half-life) and lead-212 (^{212}Pb, 10.64 h half-life) atoms are released by recoil from the source over a period determined by the ^{224}Ra half-life and diffuse in the tumor. ^{220}Rn, a noble gas, migrates

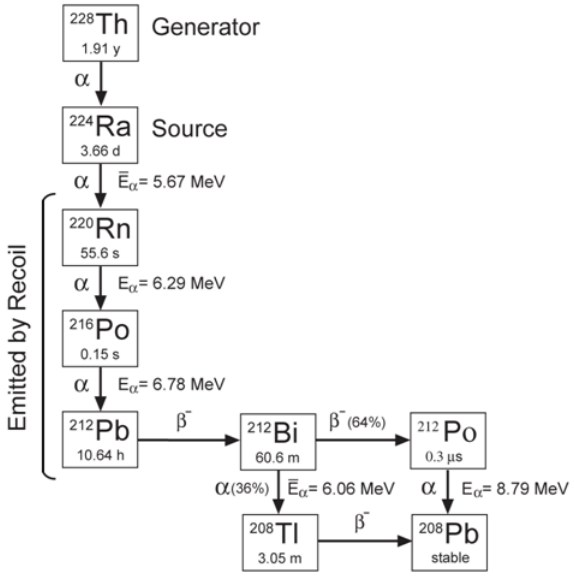

Figure 1.1: ^{224}Ra decay chain.

in the biological environment until it decays by alpha emission. This is followed almost instantaneously by alpha decay of its daughter isotope, ^{216}Po. ^{212}Pb, the result of this last decay, migrates in the tumor, eventually giving rise to yet another alpha particle. As mentioned, ^{212}Pb can also enter the tumor by recoiling directly from source. The complete listing of this alpha decay chain is given in table 1.1.

1.3 Research motivation

Several works were conducted in our lab in order to examine the effect of ^{224}Ra-loaded DART wires on different tumor types development *in vivo* [24, 23, 25]. The examination was carried out by using stainless steel sources (0.3 mm-diameter and 5-8 mm long) loaded with ^{224}Ra activities in the range of 0.5-2 kBq. Experiments were performed on BALB/c and C57BL/6 mice bearing metastatic squamous cell (SCC), pancreatic and lung carcinoma tumors, derived from appropriate cell lines. After reaching 4-10 mm in diameter the tumors of each type were divided into three groups. The first group tumors were implanted with stainless steel ^{224}Ra-loaded wires, the second group tumors were implanted with inert wires and the third group tumors were not treated. For all groups, tumor progression was recorded over a 25-35 days period.

The treatment of the SQ2, PANC02 and LL2 tumors with a single DART source resulted in the inhibition of tumor growth for all tumors types, as presented in figure 1.2. The most pronounced effect was observed in SQ2 tumors (figure 1.2a). While inert wires had no effect on tumors volume, ^{224}Ra wires considerably retarded tumor development. The effect

Isotope	Half-life	Decay mode	Energies and branching ratios (keV)				
			α	β	e	X, γ	Recoil
^{224}Ra	3.66 d	α (100%)	5449 (5.1%), 5685 (94.9%)			241 (4.1%)	^{220}Rn - 103
^{220}Rn	55.6 s	α (100%)	6288 (99.9%)				^{216}Po - 116
^{216}Po	0.145 s	α (100%)	6778 (100%)				^{212}Pb - 128
^{212}Pb	10.64 h	β$^-$ (100%)		155 (5.1%) 331 (83.1%) 570 (11.9%)	15 (22.2%) 25 (3.5%) 58 (1.3%) 148 (32.3%) 210 (1.3%) 235 (1.3%)	11 (14.3%) 75 (10.3%) 77 (17.1%) 87 (6.0%) 90 (1.5%) 239 (43.6%) 300 (3.3%)	^{212}Bi - 1.46?10^{-3}
^{212}Bi	60.55 m	α (35.9%) β$^-$ (64.1%)	6051 (25.1%) 6090 (9.8%)	633 (1.9%) 1527 (4.4%) 2254 (55.5%)	8 (12.7%) 25 (19.8%) 36 (4.6%)	10 (7.3%) 40 (1.1%) 727 (6.7%) 785 (1.1%) 1621 (1.5%)	^{208}Tl – 117 ^{212}Po – 5.87?10^{-3}
^{212}Po	0.299 μs	α (100%)	8785 (100%)				^{208}Pb – 169
^{208}Tl	3.053 m	β$^-$ (100%)		1033 (3.1%) 1286 (24.5%) 1519 (21.8%) 1796 (48.7%)	8 (4.3%) 189 (2.8%) 423 (2.0%) 495 (1.3%)	11 (2.7%) 73 (2.0%) 75 (3.3%) 277 (6.3%) 511 (22.6%) 583 (84.5%) 763 (1.8%) 861 (12.4%) 2615 (99.2%)	^{208}Pb – 6.97?10^{-3}
^{228}Th	1.912 y	α (100%)	5340 (27.2%) 5423 (72.2%)		9 (10.6%) 65 (19.3%) 80 (5.23%) 83 (1.9%)	12.3 (8.8%) 84 (1.2%)	^{224}Ra - 96

Table 1.1: ^{228}Th nuclear chain emissions.

became evident 10 days after treatment start and became more pronounced as time passed. After 20 days, the average tumor volume of the ^{224}Ra group was 12% of the average volume measured in untreated and inert wire control groups ($p < 0.01$ on Day 20). In about 22% of the ^{224}Ra treated mice, the primary tumor completely regressed, (i.e., the observable tumor temporarily disappeared) and there was one case of complete cure with no tumor recurrence.

Significant tumor growth arrest was also detected in LL2 tumors (figure 1.2b). Twenty one days post treatment, the average tumor volume of mice treated with a single DART source was 60% of the non-treated and inert wire control groups tumor volume ($p < 0.05$). Like SQ2 tumors, inert wires had no effect on tumor volume. As for PANC02 tumors, no significant growth retardation of treated tumors compared to inert wire and non-treated tumors was observed ($p > 0.5$). After twenty two days there was no difference between the average tumor volume of the three groups. Slight tumor retardation only started twenty six days after the beginning of treatment.

Similar experiments aimed to assess tumor growth retardation as a result of treatment with a single DART source were performed on additional tumor types. Generally, the effect ranged between a significant effect as observed in SQ2 tumors and a very weak effect as observed in PANC02 tumors. The interesting finding emerging from all these experiments is that the response to the DART treatment strongly depends on tumor type. This is not very surprising when taking into account that different tissue properties that can theoretically affect the treatment results might change significantly between tumors. For example, different cell types might respond differently to alpha radiation. Therefore, more resistant cell lines will probably be less affected by the DART treatment. Also, the tissue density, the blood volume and the interstitial pressure might change between different tumors. This might affect the alpha emitters spread pattern inside each tissue. The interesting question is, therefore, what are the main differences between SQ2, PANC02 and LL2 tumors and how do they relate to the DART treatment response.

An extensive experimental and theoretical program aimed to enable preliminary assessment of the processes occurring during DART treatment was conducted over the last few years by L. Arazi and T. Cooks. The existing tools enabled the presented research whose goal is to explore a few of the possible explanations for the varying effect of the DART treatment on different tumor types - Squamous cell (SQ2), pancreatic (PANC02) and lung (LL2) carcinomas. Specifically, the explored tumors properties are:

- The leakage probability of ^{212}Pb atoms out of the tumor during treatment
- The radiation distribution inside the tumor four days after treatment
- The histological properties of the tumor tissue before and after treatment

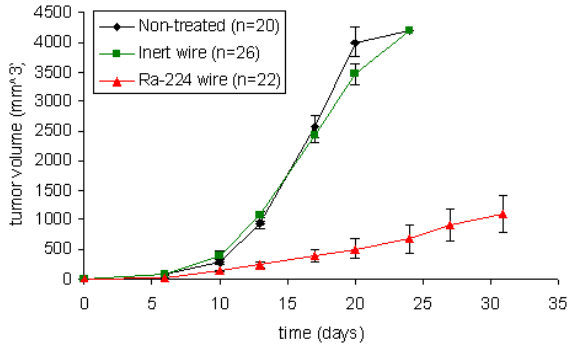

(a)

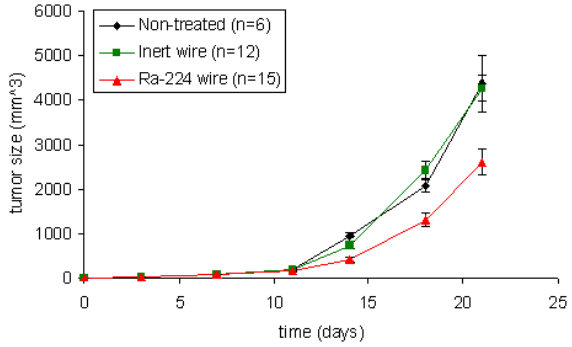

(b)

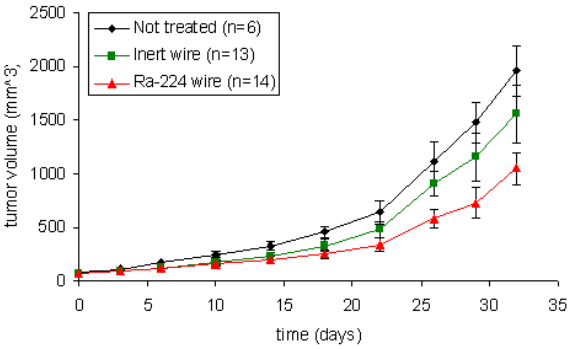

(c)

Figure 1.2: Tumor progression measurements results for BALB/c and C57BL/6 mice bearing SQ2, Panc02 and LL2 tumors accordingly. (a) SQ2 tumors development of BALB/c mice. Non-treated: Non treated tumors (n=20), Inert wire: Tumors treated with inert wire (n=26), Ra-224 wire: Tumors treated with single DART wire (n=22) [25]. (b) LL2 tumors development of C57BL/6 mice [25]. (c) Panc02 tumors development of C57BL/6 mice [8].

1.4 Chapter organization

This work is organized as follows. Chapter 2 summarizes the basic experimental procedures used during this research. Chapter 3 describes the theoretical aspects of ^{212}Pb leakage out of a tumor and presents the experimental results for different tumor types. Chapter 4 presents a histological analysis for sections of treated and untreated SQ2, PANC02 and LL2 tumors. Chapter 5 describes and presents the theoretical and experimental aspects of radiation distribution measurements inside the tumors. Finally, Chapter 6 describes the results of radiation measurements in mice organs.

Chapter 2

Experimental methods & materials

A significant part of the research described in this report was composed of experimental work *in vivo* aimed to compare different biological features of the SCC, lung and pancreatic carcinomas after treatment with DART sources. Also, theoretical work was conducted in order to extend and validate the existing model (extensively discussed in chapters 3 and 5). Most of the experimental methods used were developed by the DART research group over the last few years. The physical and technical aspects of DART source preparation were mainly developed by M. Schmidt and I. Kelson as part of the former's M.Sc. and Ph.D. work. Combined histological and auto-radiography experiments designed to detect the tumor damage and radiation spread, were mainly developed by L. Arazi and T. Cooks as part of their Ph.D. work. The main part of each of the experimental procedures was already developed before this research started. However, because of the exploratory nature of the work, some methods were reexamined and changed during the research.

The following chapter describes the main basic experimental methods that were used during this research. Application of these methods toward the study of tumor properties is described in later chapters.

A thorough description of the many intricacies involved in DART source preparation procedures is given in M. Schmidt's M.Sc. thesis and Ph.D. research proposal [16, 17]. Also, extensive explanations regarding the high resolution auto-radiography method development and calibration appear in L. Arazi's Ph.D. thesis [14].

2.1 Animals

Three types of mice were used during the research, each one for a different experimental tumor cell line. All mice were 8-12 weeks old and were obtained from the breeding colony of Tel-Aviv University, Israel. The types are Male BALB/c mice (injected with SQ2 cells), Male B57BL/6 mice (injected with LL2 cells) and Female B57BL/6 mice (injected

with PANC02 cells). Animal care and experimentation was carried out in accordance with Tel-Aviv University guidelines. All surgical and invasive procedures were held under anesthesia by intraperitoneal inoculation of imalgen (100 mg/kg) and xylazine hydrochloride (10 mg/kg) solution in 0.25 ml of PBS.

2.2 Tumor cell inoculation

BALB/c and B57BL/6 male mice were inoculated subcutaneously with $5 \cdot 10^5$ SQ2 cells or $5 \cdot 10^5$ LL2 cells (respectively) in 0.2-ml HBSS buffer (Biological industries, Israel) into the low lateral side of the back. Female B57BL/6 mice were inoculated subcutaneously with 10^5 PANC02 cells in 0.1-ml HBSS buffer also to the low lateral side of the back. The volume of the created tumor was calculated using the formula: $(\pi/6) \cdot D1 \cdot D2 \cdot D3$, where D1, D2, D3 stand for the measured diameters.

2.3 Wire preparation

DART source preparation was comprised of the following stages:

- **Electrostatic collection of ^{224}Ra from a ^{228}Th generator -** The ^{228}Th generator is a surface covered with a thin layer containing ^{228}Th. In the generator-source setup, 0.3 diameter 304 stainless steel wire with a rounded tip [1] was held vertically at a typical negative potential of 1-3 Kev relative to the generator surface (represented schematically in figure 2.1). The distance between the ^{228}Th generator and the wire tip was 5 - 15 mm. Positive ^{224}Ra ions were emitted by recoil from the surface and electrostatically collected near the tip of the wire which subsequently became the implanted source. Electrostatic collection was performed in air at atmospheric pressure. Prior to the electrostatic collection phase the wire was cleaned in an ultrasonic bath, immersed first in ethanol and then in methanol. The duration of the electrostatic collection stage was of the order of a few days. Collection setups comprising a single ^{228}Th generator were used to prepare DART sources with typical activities in the range 0.1 - 1 μCi (4 - 40 kBq) ^{224}Ra. DART sources carrying higher ^{224}Ra activities (up to 3 μCi) were prepared using collection setups comprising several ^{228}Th generators.

- **Heat treatment of the ^{224}Ra-loaded wire** - placing the ^{224}Ra source in water after the electrostatic collection leads to a rapid shedding of about 95% of the ^{224}Ra atoms. In order to reduce ^{224}Ra loss while keeping a high probability that for each decay of ^{224}Ra, its daughter ^{220}Rn will leave the source by recoil ($P_{des}(Rn)$ - Rn desorption

[1] Gooden Needle, China

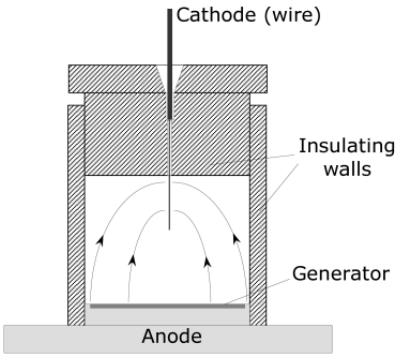

Figure 2.1: schematic representation of the generator-source setup in DART wire preparation.

probability), the source was heated to 400-470°C in vacuum after the completion of the collection phase. It was found experimentally that this procedure induced radium diffusion away from the surface to a typical depth of 10-20 nanometers leading to the desired effect. $P_{des}(Rn)$ average value after heating was 0.36 and ^{224}Ra loss to water at body temperature ranged in 1-5%. When better sealing of the ^{224}Ra atoms on the source was required an additional procedure was conducted. Before heating and after the completion of the ^{224}Ra collection phase, the source was placed in pressurized water at 130-150°C for 1 hour. This procedure lowered the long-term ^{224}Ra loss in water at body temperature to less than 0.5%.

- **Source characterization -** the source measurement setup was based on an ion-implanted silicon charged particle detector (model ULTRA, EG&G ORTEC, Oak Ridge, TN, USA) and auxiliary electronics (power supply model 4001A, detector bias supply model 428, preamplifier model 142, amplifier model 571 - all by EG&G ORTEC). After completion of the first two procedures the ^{224}Ra activity and ^{220}Rn desorption probability were recorded for each source. They were determined based on the 5685 keV line (95%) of ^{224}Ra and the 6288 keV line (100%) of ^{220}Rn. Using the detector efficiency the measurements was translated to ^{224}Ra and ^{220}Rn activity.^{220}Rn desorption probability was calculated by the formula: $P_{des}(Rn) = 1 - \frac{\Gamma_{Rn}}{\Gamma_{Ra}}$.

2.4 Source insertion

Wires, cut to a length of 5–10 mm, were placed near the tip of a 23G needle attached to a 2.5-ml syringe (Picindolor, Italy) and inserted into the tumor by a plunger placed internally along the syringe axis (figure 2.2). A 0.5 mm diameter hole was drilled in the syringe tip's

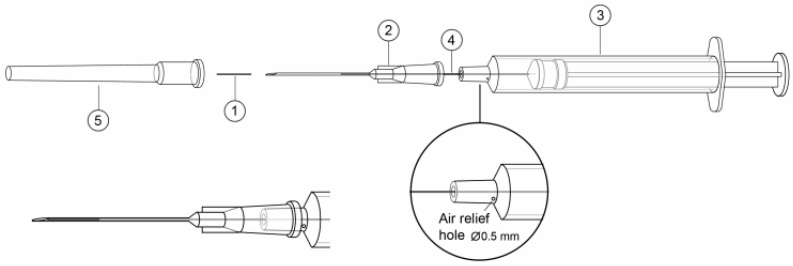

ITEM NO.	Part Description	Material	Qty.
1	DART wire	304 Stainless Steel	1
2	Hypodermic needle BD Medical No. 305120	304 Stainless Steel	1
3	3 mL syringe BD Medical No. 309586	Polypropylene	1
4	Push wire	304 Stainless Steel	1
5	Needle tip cap	Polypropylene	1

DART Applicator Mark I
Components Description

Figure 2.2: DART applicator used in the *in vivo* experiments.

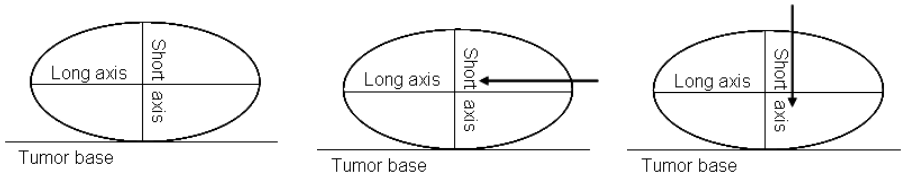

(a) (b) (c)

Figure 2.3: Schematic representation of DART source insertion directions into the tumor. (a) ellipsoid shaped tumor. The two dimensional ellipsoid represents tumors side - along the long axis of the oblate. (b) parallel source insertion into the tumor. The arrow represents DART wire insertion direction (c) perpendicular source insertion into the tumor. The arrow represents DART wire insertion direction.

base to allow for air relief during source insertion.

Sources were inserted into the tumor center, parallel or perpendicular to the long semi-axis of the oblate ellipsoid- shaped tumor. The tumor labels - 'parallel' or 'perpendicular' that appear in the following chapters are the wire insertion directions into the tumor.

2.5 Activity measurements

The ^{224}Ra decay chain contains a few gamma emitter isotopes (table 1.1). As discussed extensively in the following chapters, one of them - ^{212}Pb - is a key factor in the DART treatment. Measurements of ^{212}Pb activity in different samples, such as the tumor itself, the mouse organs and the DART source was required in order to develop a partial understanding of the processes occurring during the DART treatment.

Another important gamma emitter isotope is ^{224}Ra. Theoretically all ^{224}Ra atoms

should have been embedded below the source surface having a zero probability of leaving it. However, small amount of ^{224}Ra atoms were found experimentally in the tumor and in other tissues. Measurements of ^{224}Ra activity in the source, in the tumor and in different mouse organs helped estimate DART sources quality contributing to improvements in their production procedures.

^{212}Pb and ^{224}Ra activity in different sample types was measured by a high-efficiency, low-background, well-type NaI gamma counter (LKB Wallac 1282 CompuGamma, Wallac, Finland) focusing on the ^{212}Pb 239 keV line. Detector efficiency at 239 keV was found to be 0.76 and constant for the relevant samples volume range in a series of calibration experiments.

Typically, each sample was measured several times over a typical period of 24-72 hours. Since ^{224}Ra has a gamma line at 241 keV (branching ratio 4.1%), which cannot be separated from the 239 keV line of ^{212}Pb (branching ratio 43.6%) with the Wallac detector, the time-dependent data was analyzed in a procedure that accommodated for the possible presence of ^{224}Ra as well as ^{212}Pb in the measured sample.

2.5.1 ^{212}Pb and ^{224}Ra activity analysis procedure

The ^{212}Pb and ^{224}Ra activity of each sample should have always been calculated for a specific time which we mark as t_0. $N_i(t)$ labels the total number of atoms of either isotope in the sample at time t and $\Gamma_i \equiv \lambda_i N_i$ (λ_i is the decay constant) is the corresponding activity. We now show the procedure used in order to derive Γ_i out of the count rate measured at the gamma detector.

Placing a sample containing ^{212}Pb and ^{224}Ra atoms in the gamma counter leads to a measurement of a count rate determined by the branching ratio of each isotope (43.6% for ^{212}Pb and 4.1% for ^{224}Ra) and the detector efficiency ε(0.76 at 240 keV). The total count rate at time t is given by:

$$CR(t) = \varepsilon(0.041\Gamma_{Ra}(t) + 0.436\Gamma_{Pb}(t)) \tag{2.1}$$

The isotopes activity at time t is calculated by solving the time dependent equations for the number of atoms. Assuming that the decay of ^{224}Ra inside the sample immediately gives rise to a ^{212}Pb atom (the two intermediate decays between them occur within a half life of less than a minute) leads to an approximate description of $N_i(t)$ change with time:

$$\frac{dN_{Ra}}{dt} = -\lambda_{Ra}N_{Ra} \tag{2.2}$$

$$\frac{dN_{Pb}}{dt} = \lambda_{Ra}N_{Ra} - \lambda_{Pb}N_{Pb} \tag{2.3}$$

solving these equations and multiplying $N_i(t)$ by λ_i gives the isotopes activities at time t:

$$\Gamma_{Ra}(t) = \Gamma_{Ra}(t_0)e^{-\lambda_{Ra}(t-t_0)} \tag{2.4}$$

$$\Gamma_{Pb}(t) = \Gamma_{Pb}(t_0)e^{-\lambda_{Pb}(t-t_0)} + \frac{\lambda_{Pb}}{\lambda_{Pb}-\lambda_{Ra}}\Gamma_{Ra}(t_0)(e^{-\lambda_{Ra}(t-t_0)} - e^{-\lambda_{Pb}(t-t_0)}) \tag{2.5}$$

Finally, replacement of the isotopes activities in equation 2.1 with its exact representation (equations 2.4 and 2.5) yields a dual exponent function:

$$CR(t) = \varepsilon(Ae^{-\lambda_{Ra}(t-t_0)} + Be^{-\lambda_{Pb}(t-t_0)}) \tag{2.6}$$

$$A = 0.041\Gamma_{Ra}(t_0) + 0.436\frac{\lambda_{Pb}}{\lambda_{Pb}-\lambda_{Ra}}\Gamma_{Ra}(t_0) \tag{2.7}$$

$$B = 0.436(\Gamma_{Pb}(t_0) - \frac{\lambda_{Pb}}{\lambda_{Pb}-\lambda_{Ra}}\Gamma_{Ra}(t_0)) \tag{2.8}$$

For most samples, ^{212}Pb and ^{224}Ra activities were calculated by fitting the count rate measured in the gamma counter to a two-exponent function of the form $Ae^{-\lambda_{Ra}t} + Be^{-\lambda_{Pb}t}$ using MATLAB's curve fitting tool. The fit result - A and B values - leads immediately to the requested activities by solving equations 2.7 and 2.8.

The activities of samples with low count rate (less than several times the standard deviation of the background) was calculated by using a different procedure. The count rate in such cases was fitted with one exponent only (^{212}Pb) assuming there was no ^{224}Ra in order to avoid unrealistic estimates for the ^{224}Ra content of the sample. Also, in some cases it was reasonable to assume that a sample contains a negligible amount of ^{224}Ra. Such samples were measured only once and their activity was calculated using one exponent fit representing^{212}Pb activity.

Because of the high efficiency and low background of the Wallac detector, it was possible to detect ^{212}Pb activities down to a few Bq, where the uncertainties were of the order of 20% (the typical uncertainty for the samples used for the major part of the analysis was below 3%).

2.6 Histology

Histological analysis was performed on SQ2, Panc02 and LL2 tumors, treated with a radioactive and with an inert wire. Immediately after tumor removal, the source was removed and the tumor was fixed by a 4% formaldehyde solution for at least 24 hours. The preserved

specimen was embedded in paraffin. Histological sections (5– 10 μm) were cut using Shandon finesse microtome (Thermo scientific, Breda, The Netherlands) and placed on glass slides. The samples were then stained using hematoxylin-eosin (H&E) (Surgipath, ichmond, IL, USA). Photographs of the stained sections were obtained by an optical flatbed scanner (EPSON V750).

2.7 High Resolution Autoradiography (HRA)

High Resolution Autoradiography (HRA) is an experimental technique aimed to provide high resolution data regarding the spread of alpha diffusing atoms inside treated tumors by utilizing Fujfilm's phosphor-imaging technology. The erasable phosphor imaging plate developed by Fujfilm is comprised of a flexible plastic plate coated with a thin layer of photostimulable phosphor crystal ($BaFBr:Eu^{2+}$ or $BaFBr_xI_{1-x}:Eu^{2+}$) mixed with an organic binder. When ionizing radiation passes through the phosphor layer, some of the incoming energy is stored in long-lived excited electron states. When the crystal is stimulated by visible or infrared light, it emits photostimulated luminescence (PSL). The PSL intensity is proportional to the density of the stored energy and hence reflects the spatial pattern of the absorbed radiation.

The imaging plate used in the present work, Fujfilm's BAS-TR2040S is suitable for the detection of alpha particles since it does not have a protective coat on top of the phosphor layer (unlike other imaging plates developed for measurement of gamma radiation). A calculation of the range of alpha particles emitted during ^{224}Ra daughters decay inside the active layer showed that all of the alpha particle energy released is deposited within the layer [14]. Therefore it is possible to assume that the energy stored in the layer is proportional to the energy of the incident alpha particle. This conclusion leaded to the use of BAS-TR2040S imaging plate as measurement tool that enabled the exploration of ^{212}Pb atoms spread inside treated tumors.

The HRA experiments (frequently referred to as 'HistoFuji' experiments) are composed of many different steps. Because of the wide theoretical background required to understand the procedure motivation and results, both theoretical and experimental aspects are detailed in chapter 5. The experimental procedure is described generally after introducing the histology procedure. In HRA experiments, tumors treated with a DART source were fixated and handled using the standard procedures that enabled excision of histological sections. A short time after section preparation they were placed on top of the fujifilm imaging plate in order to record the decay of ^{212}Pb atoms that were fixated inside the section. The data regarding the spatial ^{212}Pb activity inside the tumor section was processed and analyzed by using several assumptions regarding the isotopes transport inside the tissue.

Chapter 3

^{212}Pb leakage from treated tumors

A radioactive isotope in the ^{224}Ra decay chain can either enter the tumor by direct recoil from the DART source or be created in the tumor itself by the decay of its parent atom. More specifically, assuming no ^{224}Ra is leaving the source, ^{220}Rn enters the tumor by direct recoil. ^{216}Po, ^{212}Pb and ^{208}Tl can enter the tumor in both ways.^{212}Bi and ^{212}Po atoms are only created in the tumor itself since their recoil energy is of the order of a few eV, not enough for recoiling into the tumor.

After entering the tumor the atoms begin to travel in the tissue, affected by different biological parameters such as blood vessel density, blood flow velocity, tissue density, tissue protein composition etc. The various possibilities for these parameter values together with the high number of different parameters make it almost impossible to reach a complete understanding of the processes occurring in the tumor during the DART treatment. Still, simple model development and its validation by measurements, can teach us about the most important ones.

This chapter deals with the temporal and integral behavior of the various isotopes entering the tumor. Investigation of those properties leads to interesting findings even before exploring the spatial behavior of the isotopes during the treatment.

The chapter is structured as follows. We begin with a description of the temporal behavior of the various isotopes in the ^{224}Ra decay chain as derived from the solution of 0D equations. Then the integral properties of each isotope behavior inside the tumor are described. A detailed discussion is dedicated to the three most important isotopes - ^{220}Rn, ^{212}Pb and ^{212}Bi. In order to explore the ^{212}Pb behavior, two important entities are defined in section 3.3 - *^{212}Pb leakage probability* and the *instantaneous ^{212}Pb leaking fraction.* After a short explanation regarding these parameters and their experimental measurement procedure, we present the results of several experiments aimed to explore their values in SQ2 tumors treated with a single DART source. Generally, the results show that the simple assumption according to which ^{212}Pb atoms leave the tumor through

the blood vessels at a constant rate is good enough to describe their average temporal behavior. Finally, ^{212}Pb behavior is examined for different tumor types - SQ2, PANC02 and LL2. Differences found between tumors are shown and discussed.

The theoretical model described in the first sections of this chapter was developed by L. Arazi as part of his PhD work [14]. The important parts of this model are presented here in order to enable an understanding of the additional research that was conducted.

3.1 ^{224}Ra decay chain temporal properties

The number of atoms of each isotope in a general decay chain changes with time due to its own decay and due to the decay of its parent atoms (if applicable). Both processes have their own typical half-life time. The equations describing the temporal behavior of the isotopes of our ^{224}Ra decay chain are:

$$\frac{dN_{Ra}}{dt} = -\lambda_{Ra}N_{Ra} \tag{3.1}$$

$$\frac{dN_{Rn}}{dt} = \lambda_{Ra}N_{Ra} - \lambda_{Rn}N_{Rn} \tag{3.2}$$

$$\frac{dN_{Po216}}{dt} = \lambda_{Rn}N_{Rn} - \lambda_{Po216}N_{Po216} \tag{3.3}$$

$$\frac{dN_{Pb}}{dt} = \lambda_{Po216}N_{Po216} - \lambda_{Pb}N_{Pb} \tag{3.4}$$

$$\frac{dN_{Bi}}{dt} = \lambda_{Pb}N_{Pb} - \lambda_{Bi}N_{Bi} \tag{3.5}$$

$$\frac{dN_{Po212}}{dt} = 0.641\lambda_{Bi}N_{Bi} - \lambda_{Po212}N_{Po212} \tag{3.6}$$

$$\frac{dN_{Tl}}{dt} = 0.359\lambda_{Bi}N_{Bi} - \lambda_{Tl}N_{Tl} \tag{3.7}$$

Where N_i is the number of atoms, λ_i is the decay constant of each isotope ($\lambda = ln2/T_{1/2}$) and 0.641, 0.359 are the ^{212}Bi branching ratios as listed in table 1.1. The activity for each isotope is calculated using $\Gamma_i \equiv \lambda_i N_i$ and approximate solutions for equations 3.1-3.7.

The whole decay chain is dominated by the ^{224}Ra 3.66 d half-life which is much longer than all other isotopes half-lives. The **^{224}Ra activity** is given by:

$$\Gamma_{Ra}(t) = \Gamma_{Ra}(0)e^{-\lambda_{Ra}t} \tag{3.8}$$

The first daughter of ^{224}Ra is $^{\mathbf{220}}\mathbf{Rn}$. A complete description of its activity is given by:

$$\Gamma_{Rn}(t) = \Gamma_{Rn}(0)e^{-\lambda_{Rn}t} + \frac{\lambda_{Rn}}{\lambda_{Rn} - \lambda_{Ra}}\Gamma_{Ra}(0)(e^{-\lambda_{Ra}t} - e^{-\lambda_{Rn}t}) \tag{3.9}$$

The ^{220}Rn half-life is very short (55.6 sec). Therefore, within a few minutes $e^{-\lambda_{Rn}t} \backsimeq 0$ and its activity becomes:

$$\Gamma_{Rn}(t) \backsimeq \frac{\lambda_{Rn}}{\lambda_{Rn} - \lambda_{Ra}}\Gamma_{Ra}(0)e^{-\lambda_{Ra}t} = 1.0002\Gamma_{Ra}(t) \tag{3.10}$$

The practical meaning is that within a few minutes ^{220}Rn and ^{224}Ra attain secular equilibrium. The same behavior holds for $^{216}\mathbf{Po.}$ Its half -life is even shorter than that of ^{220}Rn (0.145 sec). After several minutes its activity is almost equal to the ^{224}Ra activity:

$$\Gamma_{Po216}(t) \backsimeq \frac{\lambda_{Po216}}{\lambda_{Po216} - \lambda_{Rn}}\Gamma_{Rn}(t) = 1.0002\Gamma_{Ra}(t) \tag{3.11}$$

The $^{212}\mathbf{Pb}$ half life is much longer than that of ^{220}Rn and ^{216}Po. The solution of equation 3.4 gives:

$$\Gamma_{Pb}(\mathrm{t}) = \Gamma_{Pb}(0)e^{-\lambda_{Pb}t} + \frac{\lambda_{Pb}}{\lambda_{Pb} - \lambda_{Po216}}\Gamma_{Po216}(0)(e^{-\lambda_{Po216}t} - e^{-\lambda_{Pb}t}) \tag{3.12}$$

Insertion of ^{216}Po activity for times greater than several minutes from t=0 into equation 3.12 yields an approximation of the ^{212}Pb activity vs. time:

$$\Gamma_{Pb}(t) \simeq \Gamma_{Pb}(0)e^{-\lambda_{Pb}t} + 1.0002\frac{\lambda_{Pb}}{\lambda_{Pb} - \lambda_{Ra}}\Gamma_{Ra}(0)(e^{-\lambda_{Ra}t} - e^{-\lambda_{Pb}t}) \tag{3.13}$$

The temporal behavior of the ^{212}Pb activity in comparison to ^{224}Ra activity is shown in figure 3.1. During the first hours after t=0, ^{212}Pb activity, which starts from zero, continually becomes higher while ^{224}Ra activity becomes smaller (decays with ^{224}Ra half-life). The^{212}Pb activity reaches its maximum which is temporarily equal to the ^{224}Ra activity value at a time $t_{max} = 36.9$h. For $t > t_{max}$ the ^{212}Pb activity gradually decreases, asymptotically decaying with the ^{224}Ra half-life and with ratio of the two activities reaching a codeep thinking aboutnstant value:

$$\Gamma_{Pb}(t) \simeq 1.138\Gamma_{Ra}(t) \tag{3.14}$$

In a similar way, the $^{\mathbf{212}}\mathbf{Bi}$ activity as a function of time is calculated by solving equation 3.5 and using the approximation for ^{212}Pb in 3.13:

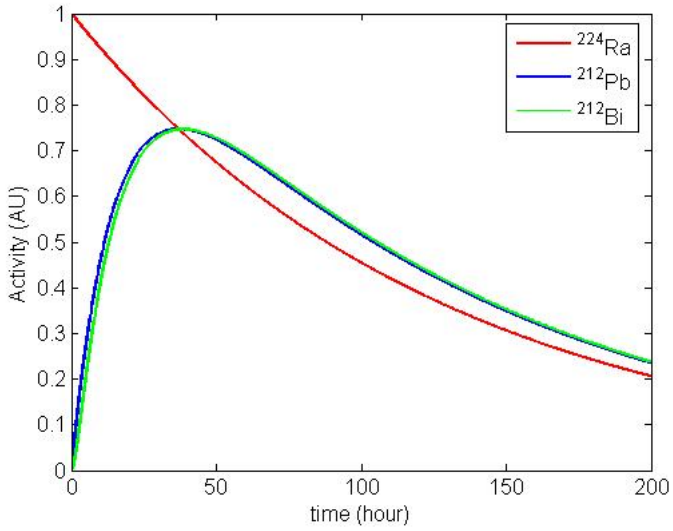

Figure 3.1: Activity of ^{224}Ra decay chain isotopes - ^{224}Ra, ^{212}Pb and ^{212}Bi as a function of time. Activity is normalized such that the activity at t=0 is 1 (arbitrary units)

$$\begin{aligned}\Gamma_{Bi}(t) \simeq\ & \Gamma_{Bi}(0)e^{-\lambda_{Bi}t} + \frac{\lambda_{Bi}}{\lambda_{Bi}-\lambda_{Pb}}\left(\Gamma_{Pb}(0) - 1.0002\frac{\lambda_{Pb}}{\lambda_{Pb}-\lambda_{Ra}}\Gamma_{Ra}(0)\right)(e^{-\lambda_{Pb}t} - e^{-\lambda_{Bi}t}) + \\ & 1.0002\frac{\lambda_{Bi}}{\lambda_{Bi}-\lambda_{Ra}}\frac{\lambda_{Pb}}{\lambda_{Pb}-\lambda_{Ra}}\Gamma_{Ra}(0)(e^{-\lambda_{Ra}t} - e^{-\lambda_{Bi}t})\end{aligned}$$

For $t \gg \tau_{Pb}$ the activity becomes:

$$\Gamma_{Bi}(t) \backsimeq 1.0002\frac{\lambda_{Bi}}{\lambda_{Bi}-\lambda_{Ra}}\frac{\lambda_{Pb}}{\lambda_{Pb}-\lambda_{Ra}}\Gamma_{Ra}(0)e^{-\lambda_{Ra}t} = 1.012\Gamma_{Pb}(t) = 1.151\Gamma_{Ra}(t) \quad (3.15)$$

^{212}Pb and ^{212}Bi temporal behavior is very similar. ^{212}Bi activity reaches its maximum value about 1.1 hours after ^{212}Pb. The short-lived daughters of ^{212}Bi - ^{212}Po and ^{212}Tl - follow their parent's temporal behavior. Within about $1\mu s$ we get

$$\Gamma_{Po212}(t) = 0.64\Gamma_{Bi}(t)$$

and within several hours:

$$\Gamma_{Tl}(t) \simeq 0.36\Gamma_{Bi}(t)$$

3.2 ^{224}Ra decay chain atoms in tumor

Experimental data gathered so far indicates that during DART treatment, a region inside the tumor measuring a few mm in size is exposed to an high-LET radiation. Theoretically, this becomes possible due to the six diffusing radionuclides released from DART source - ^{220}Rn, ^{216}Po,^{212}Pb,^{208}Tl,^{212}Bi and ^{212}Po. Examination of the temporal behavior of each of the isotopes leads to the conclusion that in practice only three of them contribute directly to the impressive dose spread observed - ^{220}Rn, ^{212}Pb and ^{212}Bi. ^{216}Po and ^{212}Po have a very short half life (0.15 sec and $0.3\mu sec$ respectively). Therefore, it is very reasonable to assume that they decay at the same point as their parents (^{220}Rn and ^{212}Bi respectively) and do not contribute to the radiation spread. ^{208}Tl does not lead to the emission of an alpha particle. Therefore, it has little importance in terms of the source dosimetry and its contribution to the spatial spread is negligible.

A detailed discussion of the spatial distribution of each of the three isotopes is given in the next chapter. In the following sections we start with a presentation of the assumed integral and temporal properties of ^{220}Rn ^{212}Pb and ^{212}Bi inside a treated tumor.

3.2.1 ^{220}Rn

^{220}Rn is emitted from the source by recoil following ^{224}Ra decay with a typical desorption probability ($P_{des}(Rn)$) of 30-40%. ^{220}Rn is a noble gas, and therefore its atoms are free to diffuse in the tissue with no chemical interactions. We assume that ^{220}Rn atoms do not leave the tumor since the main route out - through the blood vessels - is not available for them. ^{220}Rn atoms cannot bind to molecules inside the blood that trap the atoms and remove them from the tumor.

The equation describing the ^{220}Rn integral behavior inside the tumor is:

$$\frac{dN_{Rn}^{tum}}{dt} = S - \lambda_{Rn} N_{Rn}^{tum} \tag{3.16}$$

where S is the source term and N_{Rn}^{tum} is the total number of ^{220}Rn atoms. Since ^{220}Rn atoms are emitted directly from the source, S is given by:

$$S = P_{des}(Rn)\Gamma_{Ra}^{src} = P_{des}(Rn)\Gamma_{Ra}^{src}(0)e^{-\lambda_{Ra}t} \tag{3.17}$$

Using the initial condition $\Gamma_{Rn}(0) = 0$ and solving equation 3.16 after insertion of 3.17 yields the following expression for the integral ^{220}Rn activity:

$$\Gamma_{Rn}^{tum}(t) = \lambda_{Rn} N_{Rn}^{tum}(t) = \frac{\lambda_{Rn}}{\lambda_{Rn} - \lambda_{Ra}} P_{des}(Rn)\Gamma_{Ra}^{src}(0)(e^{-\lambda_{Ra}t} - e^{-\lambda_{Rn}t}) \tag{3.18}$$

Within several minutes this activity becomes:

$$\Gamma_{Rn}^{tum}(t) \approx \frac{\lambda_{Rn}}{\lambda_{Rn}-\lambda_{Ra}} P_{des}(Rn)\Gamma_{Ra}^{src}(0)e^{-\lambda_{Ra}t} \approx P_{des}(Rn)\Gamma_{Ra}^{src}(0)e^{-\lambda_{Ra}t}$$

Not surprisingly, the expression describing the temporal behavior of ^{220}Rn inside the tumor is very similar to the general 0D solution (equation 3.10). As in the general case, the ^{224}Ra activity on the source and the total ^{220}Rn activity (on the source and inside the tumor) are equal. Inside the tumor, however, only a fraction of the total ^{220}Rn activity is found- the fraction that has been released from the source by recoil. Therefore the only difference between the two solutions is the product of ^{220}Rn activity inside the tumor times the ^{220}Rn desorption probability. The ratio between ^{220}Rn activity in the tumor and the total ^{224}Ra activity is $\frac{\Gamma_{Rn}^{tum}}{\Gamma_{Ra}^{tot}} = P_{des}(Rn)$.

3.2.2 ^{212}Pb

^{212}Pb enters the tumor in 3 possible ways:

1. Direct recoil from the source, following ^{216}Po alpha decay events
2. Alpha decays of ^{216}Po atoms which have recoiled out of the source
3. Alpha decays of ^{216}Po following ^{220}Rn decays away from the source

The sum of these three possible routes is defined as the effective desorption probability of ^{212}Pb ($P_{des}^{eff}(Pb)$) and is given by the expression:

$$P_{des}^{eff}(Pb) = P_{des}(Rn) + (1-P_{des}(Rn))P_{des}(Po) + (1-P_{des}(Rn))(1-P_{des}(Po))P_{des}(Pb) \tag{3.19}$$

where $P_{des}(Po)$ is ^{216}Po desorption probability from the source.

^{212}Pb enters the tumor as an ion but it is well known that the percentage of the bio-available lead in tissue is very low [10]. Therefore, we assume that after entering into the tumor ^{212}Pb atoms rapidly binds to the surrounding proteins [2]. Also, it is known that inside the blood vessels most of the lead atoms are attached to red blood cells (RBCs) [21]. Our second assumption is that RBCs act as a trap for ^{212}Pb atoms entering the blood vessels inside the tumor. ^{212}Pb atoms that reach the blood stream are cleared from the tumor with different times depending on the vasculature properties (morphology, rheology etc.).

Using the last assumption we write an approximate description of the ^{212}Pb atoms temporal behavior inside the tumor:

$$\frac{dN_{Pb}^{tum}}{dt} = S - (\alpha_{Pb} + \lambda_{Pb})N_{Pb}^{tum} \tag{3.20}$$

Where S is the source term and N_{Pb}^{tum} is the total number of ^{212}Pb atoms. α_{Pb} is a sink term that represents ^{212}Pb atoms clearance rate ($\tau_{Pbleak} = \frac{1}{\alpha_{Pb}}$ is the average clearance time). The approximation which underlies this term is that the clearance rate has no time dependence. The real clearance process of ^{212}Pb atoms in tumor is probably much more complicated. However, as detailed below, our experimental results agree with this simple assumption. Also, this simple model is only aimed to provide a first order quantitative estimates and to get a qualitative understanding of the ^{212}Pb atoms temporal behavior.

The source term, S, is given by:

$$S = \lambda_{Rn} N_{Rn}^{tum}(t) + (P_{des}^{eff}(Pb) - P_{des}(Rn))\Gamma_{Ra}^{src}(0)e^{-\lambda_{Ra}t} \tag{3.21}$$

which becomes within a few minutes:

$$S \approx P_{des}^{eff}(Pb)\Gamma_{Ra}^{src}(0)e^{-\lambda_{Ra}t} \tag{3.22}$$

Solving equation 3.20 by using the initial condition $N_{Pb}^{tum}(0) = 0$ and equation 3.22 gives the ^{212}Pb approximate activity inside the tumor as a function of time:

$$\Gamma_{Pb}^{tum}(t) \approx \frac{\lambda_{Pb}}{\lambda_{Pb} + \alpha_{Pb} - \lambda_{Ra}} P_{des}^{eff}(Pb)\Gamma_{Ra}^{src}(0)(e^{-\lambda_{Ra}t} - e^{-(\lambda_{Pb}+\alpha_{Pb})t}) \tag{3.23}$$

As before, the result is very similar to the ^{212}Pb activity in 0D (3.13) with two main differences . The first difference is the $P_{des}^{eff}(Pb)$ factor in the solution. This results from the partial entrance of ^{212}Pb atoms into the tumor with a probability of $P_{des}^{eff}(Pb)$. The second difference, and the more important one, is the addition of the sink term. A careful look at 3.23 reveals that the ^{212}Pb decay constant λ_{Pb} can be replaced by an effective decay constant :

$$\lambda_{Pb}^{eff} = \lambda_{Pb} + \alpha_{Pb}$$

Writing the new decay constant shows that the^{212}Pb activity in the tumor has the same qualitative behavior as in 0D but with a few quantitative differences. The effective mean lifetime of ^{212}Pb inside the tumor is shorter than its natural life time: $\tau_{Pb}^{eff} = \frac{1}{\lambda_{Pb}+\alpha_{Pb}}$. Also, the maximal value of ^{212}Pb activity inside the tumor is reached after 20.3 h compared to 36.9 h when no ^{212}Pb is removed from the tumor.

3.2.3 ^{212}Bi

^{212}Bi is created inside the tumor by ^{212}Pb beta decays and is not released from the DART source. As ^{212}Pb atoms, ^{212}Bi atoms can be removed from the tumor by interaction with molecules inside the blood vessels. We consider this process even though experimental data shows that it is a second order effect [14].

^{212}Bi behavior inside the tumor is described by:

$$\frac{dN_{Bi}^{tum}}{dt} = \lambda_{Pb}N_{Pb} - (\lambda_{Bi} + \alpha_{Bi})N_{Bi} \tag{3.24}$$

With the initial condition $N_{Bi}^{tum}(0) = 0$ and neglecting ^{220}Rn buildup, ^{212}Bi activity is calculated to be within a few minutes:

$$\Gamma_{Bi}^{tum}(t) = A(e^{-\lambda_{Ra}t} - e^{-(\lambda_{Bi}+\alpha_{Bi})t}) + B(e^{-(\lambda_{Pb}+\alpha_{Pb})t} - e^{-(\lambda_{Bi}+\alpha_{Bi})t})$$

$$A = \frac{\lambda_{Bi}}{\lambda_{Bi} + \alpha_{Bi} - \lambda_{Ra}} \frac{\lambda_{Pb}}{\lambda_{Pb} + \alpha_{Pb} - \lambda_{Ra}} P_{des}^{eff}(Pb)\Gamma_{Ra}^{src}(0)$$

$$B = -\frac{\lambda_{Bi}}{\lambda_{Bi} + \alpha_{Bi} - \lambda_{Pb} - \alpha_{Pb}} \frac{\lambda_{Pb}}{\lambda_{Pb} + \alpha_{Pb} - \lambda_{Ra}} P_{des}^{eff}(Pb)\Gamma_{Ra}^{src}(0)$$

and for asymptotic times:

$$\Gamma_{Biasy}^{tum} = \frac{\lambda_{Bi}}{\lambda_{Bi} + \alpha_{Bi} - \lambda_{Ra}} \frac{\lambda_{Pb}}{\lambda_{Pb} + \alpha_{Pb} - \lambda_{Ra}} P_{des}^{eff}(Pb)\Gamma_{Ra}^{src}(0)e^{-\lambda_{Ra}t}$$

Hence, using equation 3.23 the asymptotic ^{212}Bi/^{212}Pb activity ratio is:

$$\frac{\Gamma_{Biasy}^{tum}}{\Gamma_{Pbasy}^{tum}} = \frac{\lambda_{Bi}}{\lambda_{Bi} + \alpha_{Bi} - \lambda_{Ra}} \tag{3.25}$$

.

3.3 ^{212}Pb leakage out of the tumor

Identification of ^{212}Pb as a key element in DART treatment and the relative simplicity of its measurement, lead to the performance of extensive experimental work aimed to study the ^{212}Pb atoms temporal behavior inside the tumor. As noted above, a very important characteristic of this behavior is the clearance rate of the atoms by the blood. Several experiments were performed in order to explore this property. These experiments and their results are described in this section.

3.3.1 ^{212}Pb leakage probability

The ^{212}Pb leakage probability is defined as the probability that ^{212}Pb atoms released from the source decay outside the tumor:

$$P_{leak}(Pb) = \frac{\text{total number of Pb decays outside the tumor}}{\text{total number of Pb atoms released by the source}}$$

It is also equal to 1 minus the probability that a ^{212}Pb atom, released from the source, decays inside the tumor . Mathematically it is given by:

$$P_{leak}(Pb) = 1 - \frac{A_{Pb}^{tum}}{A_{Pb}^{rel}} \tag{3.26}$$

where A_{Pb}^{tum} is the total number of ^{212}Pb decays inside the tumor from the time of source insertion on. A_{Pb}^{tum} is calculated by:

$$A_{Pb}^{tum} = \int_0^\infty \Gamma_{Pb}^{tum}(t)dt = \frac{\lambda_{Pb}}{\lambda_{Pb} + \alpha_{Pb}} P_{des}^{eff}(Pb) N_{Ra}^{src}(0) \tag{3.27}$$

A_{Pb}^{rel} is the total number of ^{212}Pb atoms released from the source and is given by:

$$A_{Pb}^{rel} = P_{des}^{eff}(Pb) N_{Ra}^{src}(0) \tag{3.28}$$

Insertion of equation 3.27 and equation 3.28 into 3.26 gives:

$$P_{leak}(Pb) = \frac{\alpha_{Pb}}{\lambda_{Pb} + \alpha_{Pb}} \tag{3.29}$$

According to this expression the ^{212}Pb leakage probability variess in the range 0-1 and is closely related to the ^{212}Pb atoms clearance rate - α_{Pb}.

Assuming ^{212}Pb removal rate is linear, $P_{leak}(Pb)$ was estimated experimentally for tumors treated with one DART source. For that, measurement of five properties was required:

- $\Gamma_{Ra}^{src}(t_{TR})$,$\Gamma_{Pb}^{src}(t_{TR})$- ^{224}Ra and ^{212}Pb activities on the source at tumor removal time
- $\Gamma_{Ra}^{tum}(t_{TR})$,$\Gamma_{Pb}^{tum}(t_{TR})$- ^{224}Ra and ^{212}Pb activities in tumor at tumor removal time
- $\frac{\Gamma_{Pb}^{src}(0)}{\Gamma_{Ra}^{src}(0)}$- the ratio of ^{224}Ra and ^{212}Pb activities on the source at t=0

The experimental procedure that was used for the measurement of those quantities is described in section 3.3.3. Assuming that these quantities are given, we will explain the $P_{leak}(Pb)$ calculation based on the assumption that ^{212}Pb clearance rate is linear (linearity assumption) and on the assumption that no ^{224}Ra is leaving the source during treatment.

The ^{224}Ra and ^{212}Pb activities on the source and inside the tumor are given by:

$$\Gamma_{Ra}^{src}(t) = \Gamma_{Ra}^{src}(0)e^{-\lambda_{Ra}t} \tag{3.30}$$

$$\Gamma_{Ra}^{tum}(t) = 0 \tag{3.31}$$

$$\Gamma_{Pb}^{src}(t) = \Gamma_{Pb}^{src}(0)e^{-\lambda_{Pb}t} + (1 - P_{des}^{eff}(Pb))\frac{\lambda_{Pb}}{\lambda_{Pb} - \lambda_{Ra}}\Gamma_{Ra}^{src}(0)(e^{-\lambda_{Ra}t} - e^{-\lambda_{Pb}t}) \tag{3.32}$$

$$\Gamma_{Pb}^{tum}(t) = \frac{\lambda_{Pb}}{\lambda_{Pb} + \alpha_{Pb} - \lambda_{Ra}}P_{des}^{eff}(Pb)\Gamma_{Ra}^{src}(0)(e^{-\lambda_{Ra}t} - e^{-(\lambda_{Pb}+\alpha_{Pb})t}) \tag{3.33}$$

The first step for estimating the ^{212}Pb leakage probability includes the calculation of the effective ^{212}Pb probability by solving equations 3.32 and 3.33 at tumor removal time (t_{TR}):

$$P_{des}^{eff}(Pb) = 1 - \frac{[\Gamma_{Pb}^{src}(t_{TR})/\Gamma_{Ra}^{src}(t_{TR})] - [\Gamma_{Pb}^{src}(0)/\Gamma_{Ra}^{src}(0)]\, e^{-(\lambda_{Pb}-\lambda_{Ra})t_{TR}}}{\frac{\lambda_{Pb}}{\lambda_{Pb}-\lambda_{Ra}}(1 - e^{-(\lambda_{Pb}-\lambda_{Ra})t_{TR}})} \tag{3.34}$$

where t=0 is the time of source insertion. Once $P_{des}^{eff}(Pb)$ is found, equation 3.33 is solved numerically in order to calculate α_{Pb}. $P_{leak}(Pb)$ is then calculated by inserting the acquired sink term into equation 3.29.

Using the above procedure in order to calculate ^{212}Pb leakage probability requires careful consideration of the measurement time of the five quantities used for the calculation. These quantities, and specifically the quantity which we use in order to calculate α_{Pb} - $\Gamma_{Pb}^{tum}(t)$, are time dependent. The sensitivity and accuracy of the α_{Pb} calculation changes for different measurement times of them. Figure 3.2 shows the ^{212}Pb activity in the tumor as a function of time for different alpha values in the range 0.69-0.003 (characteristic ^{212}Pb removal time from 1 hour to 200 hours) calculated using equation 3.33. As can be seen, the ^{212}Pb activity in the tumor rises from zero at source insertion time to its maximal value (as described in section 3.2.2) reached after a period depending on the alpha value. However, the initial rise in activity is very similar for all alpha values. Only after reaching the maximum ^{212}Pb activity, a significant difference can be identified between the activity graphs. This behavior implies that it is better to estimate the alpha value of a given tumor by using activity measurements taken after at least 1-1.5 days of treatment. After this time, the numerical calculation of alpha gives a much more significant result based on the indicative activity value.

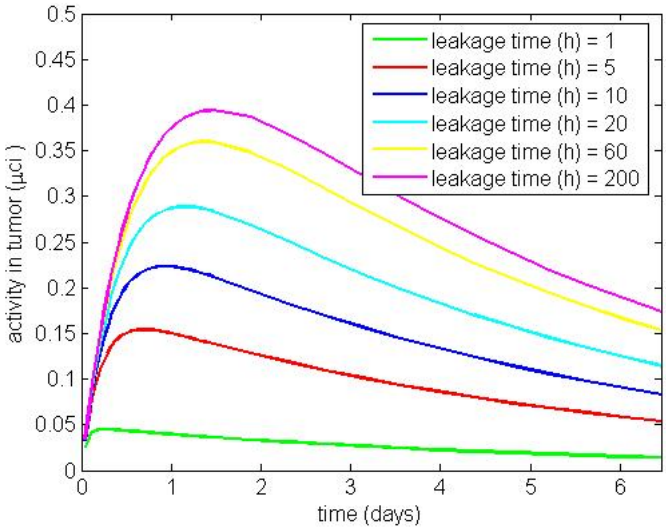

Figure 3.2: ^{212}Pb activity in tumor as the function of time for changing alpha values. The initial ^{224}Ra activity on source was set to be $1\mu Ci$ and $P_{des}^{eff}(Pb)$=0.55 (this is the average result that was observed experimentally for many DART sources).

3.3.2 The instantaneous ^{212}Pb leaking fraction

The total ^{212}Pb activity inside a tumor removed from a treated mice and the total ^{212}Pb activity released from the inserted source can be easily determined for any specific time by several measurements of the tumor and the source in a gamma counter. Usually, these activities are calculated at the time of tumor removal by the analysis procedure described in chapter 2.

We define a second useful quantity for the examination of ^{212}Pb temporal behavior - *the instantaneous ^{212}Pb leaking fraction* ($f_{Pbleak}(t)$). This entity represents the missing ^{212}Pb activity fraction in the tumor at a specific time and is equal to 1 minus the instantaneous ratio of the ^{212}Pb activity in the tumor and ^{212}Pb activity released from the source:

$$f_{Pbleak}(t) = 1 - \frac{\Gamma_{Pb}^{tum}(t_{TR})}{\Gamma_{Pb}^{rel}(t_{TR})} \tag{3.35}$$

f_{Pbleak} can be calculated directly from the measurements of ^{224}Ra and ^{212}Pb activities on the source and inside the tumor at tumor removal time, without using the linearity assumption. As noted above, the activity of ^{212}Pb in the tumor ($\Gamma_{Pb}^{tum}(t_{TR})$) is calculated directly from the tumor measurements. The ^{212}Pb activity released from source into the tumor at tumor removal time ($\Gamma_{Pb}^{rel}(t_{TR})$) is found by the subtraction of the ^{212}Pb activity measured on the source at tumor removal time from the total ^{212}Pb activity in the system at that time $\Gamma_{Pb}^{rel}(t_{TR}) = \Gamma_{Pb}^{tot}(t_{TR}) - \Gamma_{Pb}^{src}(t_{TR})$.

The total ^{212}Pb activity in the system (source and tumor) is given by:

$$\Gamma^{tot}_{Pb}(t_{TR}) = \Gamma^{src}_{Pb}(0)e^{-\lambda_{Pb}t_{TR}} + \frac{\lambda_{Pb}}{\lambda_{Pb}-\lambda_{Ra}}\Gamma^{src}_{Ra}(0)(e^{-\lambda_{Ra}t_{TR}} - e^{-\lambda_{Pb}t_{TR}}) \tag{3.36}$$

The ^{212}Pb activity in the source is given by equation 3.32. Insertion of this expression together with 3.36 gives:

$$\Gamma^{rel}_{Pb}(t_{TR}) = \Gamma^{tot}_{Pb}(t_{TR}) - \Gamma^{src}_{Pb}(t_{TR}) = \frac{\lambda_{Pb}}{\lambda_{Pb}-\lambda_{Ra}}P^{eff}_{des}(Pb)\Gamma^{src}_{Ra}(0)(e^{-\lambda_{Ra}t_{TR}} - e^{-\lambda_{Pb}t_{TR}}) \tag{3.37}$$

Now the only missing entity is the ^{224}Ra activity in the source. This value is measured before source insertion. Usually, however, the source is cut before insertion and the exact amount of ^{224}Ra activity in the source at the time of insertion is unknown. Calculation of ^{224}Ra activity is therefore done by using the activity measurement at tumor removal and back extrapolation to source insertion time: $\Gamma^{src}_{Ra}(0) = \Gamma^{src}_{Ra}(t_{TR})e^{\lambda_{Ra}t_{TR}}$.

If the tumor removal time is of the order of a few days, the entire system is close to secular equilibrium. We can then calculate the released ^{212}Pb activity more easily by the approximation:

$$\Gamma^{rel}_{Pb}(t_{TR}) = \Gamma^{tot}_{Pb}(t_{TR}) - \Gamma^{src}_{Pb}(t_{TR}) \approx 1.14\Gamma^{src}_{Ra}(t_{TR}) - \Gamma^{src}_{Pb}(t_{TR})$$

A second way of calculating f_{Pbleak} is by using the linearity assumption. After a few minutes from source insertion the ^{212}Pb activity in tumor is given by equation 3.33. The ^{212}Pb activity released from the source is given by equation 3.37. Inserting this expression into 3.35 gives:

$$f_{Pbleak}(t) = 1 - \frac{\frac{\lambda_{Pb}}{\lambda_{Pb}+\alpha_{Pb}-\lambda_{Ra}}P^{eff}_{des}(Pb)\Gamma^{src}_{Ra}(0)(e^{-\lambda_{Ra}t} - e^{-(\lambda_{Pb}+\alpha_{Pb})t})}{\frac{\lambda_{Pb}}{\lambda_{Pb}-\lambda_{Ra}}P^{eff}_{des}(Pb)\Gamma^{src}_{Ra}(0)(e^{-\lambda_{Ra}t} - e^{-\lambda_{Pb}t})} \tag{3.38}$$

which asymptotically becomes:

$$f^{asy}_{Pbleak} = \frac{\alpha_{Pb}-\lambda_{Ra}}{\lambda_{Pb}+\alpha_{Pb}-\lambda_{Ra}}$$

The asymptotic or instantaneous value of f_{Pbleak} can be calculated in a similar way to the calculation of the ^{212}Pb leakage probability. First we find $P^{eff}_{des}(Pb)$ and α_{Pb} using the procedure described in 3.3.1. α_{Pb} is used in order to calculate f_{Pbleak} value.

As for the ^{212}Pb leakage probability, the study of the f_{Pbleak} temporal behavior is important in order to understand the experimental limitations of its measurement. The

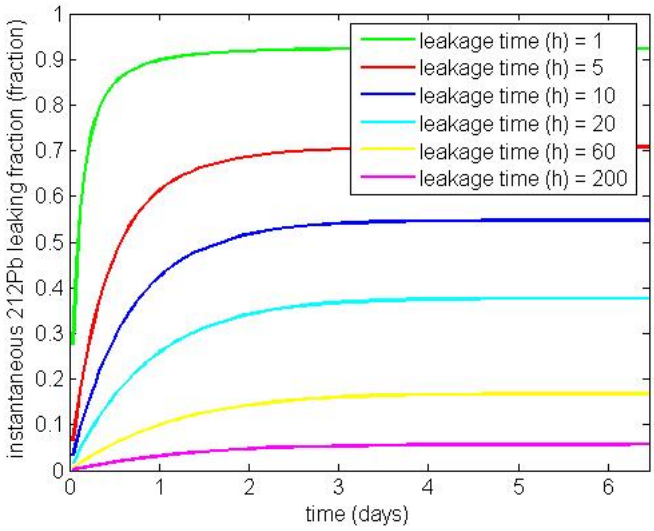

Figure 3.3: f_{Pbleak} value as function of time for changing alpha values.

value of f_{Pbleak} as a function of time, for different alpha parameters in the range 0.693-0.003 (characteristic ^{212}Pb removal time between 1 hour and 200 hours) was calculated using equation 3.38. The result is presented in figure 3.3. As expected, f_{Pbleak} stabilizes after a relatively quick increase of its value. For most alpha values, after one day of treatment the instantaneous ^{212}Pb leaking fraction is constant as a function of time. Thus, we can expect that experimental measurement of tumors with a similar leakage rate at times greater than one day after treatment will give similar f_{Pbleak} values.

It is important to remember that by definition, f_{Pbleak} does not depend on the assumption that the ^{212}Pb leakage rate from the tumor is linear. Finding similar f_{Pbleak} values in similar tumors treated for different time periods can therefore support our linear model.

3.3.3 Experimental procedures for clearance rate exploration - SCC

The measurement of ^{212}Pb leakage from a tumor treated with a DART source is not a simple task. The reason is the high variability of different characteristics of the experimental system containing the tumor and the source. For example, the orientation of the DART source inside the tumor is a very important parameter affecting the leakage probability. It is reasonable to assume that if the source is located near the tumor surface, the ^{212}Pb leakage is higher than when the source is located in the tumor center. Still, even when one follows the experimental procedure described in section 2.4 it is impossible to ensure that the orientation is the same for every treated tumor.

Another example is tumor size. The effect of tumor size on ^{212}Pb leakage is quite intuitive. In the center of big tumors we usually find several necrotic areas with little

amount of normal blood vessels that can enable a removal of ^{212}Pb atoms out of the tumor. In small tumors the distance which the atoms should pass inside the tumor to reach its perimeter is small and usually the necrotic area is very limited. Therefore we expect that large tumors will have a lower leakage of ^{212}Pb out of the tumor in comparison to small tumors.

A few different experiments were conducted in order to assess the effect of different parameters on tumor leakage probability values and to confirm the validity of the linearity assumption. In what follows we first describe the procedures used in order to measure the five quantities required for the calculation of the leakage probability (see 3.3.1) and then describe these experiments and their results.

The instantaneous ^{212}Pb leaking fraction and the ^{212}Pb leakage probability which were defined in the previous section and which were calculated for each experiment, are relative amounts that do not depend on the initial DART source activity. The experiments that will now be described were conducted by using different DART sources with an initial ^{224}Ra activity in the range 0.3-1.5 μCi. Due to the irrelevance of the specific activity used for each experiment it is not specified.

Integral activities measurement

As was described in sections 3.3.1 and 3.3.2 measurement of five quantities are required in order to calculate the ^{212}Pb leakage probability or the instantaneous ^{212}Pb leaking fraction of a treated tumor:

- $\frac{\Gamma^{src}_{Pb}(0)}{\Gamma^{src}_{Ra}(0)}$- the ratio of ^{224}Ra and ^{212}Pb activities on the source at t=0
- $\Gamma^{src}_{Ra}(t_{TR})$,$\Gamma^{src}_{Pb}(t_{TR})$- ^{224}Ra and ^{212}Pb activities on the source at tumor removal time
- $\Gamma^{tum}_{Ra}(t_{TR})$,$\Gamma^{tum}_{Pb}(t_{TR})$- ^{224}Ra and ^{212}Pb activities in the tumor at tumor removal time

The ratio of ^{224}Ra and ^{212}Pb activities on the source at source insertion (t=0) was calculated from alpha spectroscopy measurements of the source prior to its insertion into the tumor. Since ^{212}Pb does not decay by alpha emission and ^{212}Po and ^{212}Pb are in secular equilibrium, the ^{212}Pb activity was determined by the ^{212}Po activity. The required ratio was found by the division of ^{212}Po peak value (on the 8785 KeV line) by ^{224}Ra 95% peak value (on the 5685 KeV line) multiplied by 0.64/0.95.

Calculation of ^{212}Pb and ^{224}Ra activities on the source was done by analyzing the gamma counter measurements of the source after its removal from the tumor using the procedure described in 2.5.1. Sources removed from the tumor were inserted into a capped scintillation vial containing 0.5 ml of deionized water in order to stay confined to the vial bottom, for which the detection efficiency was known. The sources were measured several

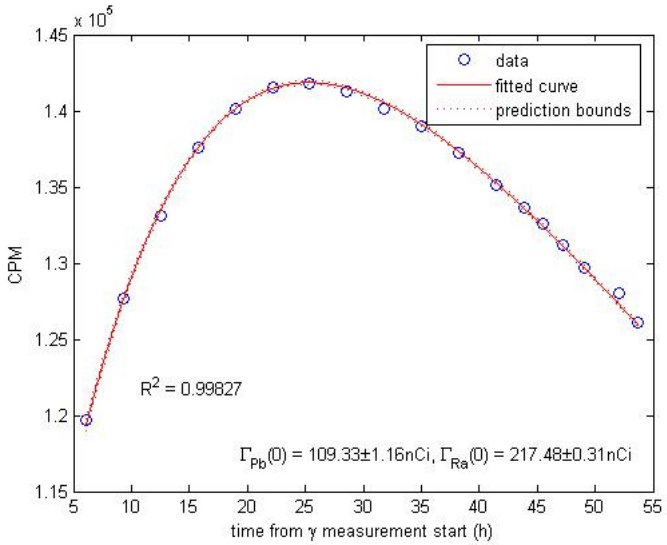

Figure 3.4: Dual-exponent fit of the count rate of DART source removed from tumor

times over a typical period of 48-72 hours. The time for which the activities were calculated (t0) was the tumor removal time. An example of the analysis results is given in figure 3.4.

Two methods were used in order to calculate ^{212}Pb and ^{224}Ra activities inside the tumor at tumor removal time. In the first one, the tumor extracted from the animal was placed on dry ice. After a few minutes, the tumor was removed from the ice and the source was extracted by carefully cutting pieces from the tumor end exposing the source and enabling its extraction. The dissected tumor was inserted into a vial containing 4% formaldehyde solution. A few hours later the tumor was taken for a single measurement in the gamma counter under the assumption that ^{224}Ra activity in the tumor is negligible. The tumor ^{212}Pb activity at tumor removal was calculated by back extrapolation of the activity value at measurement time. When the radium absence assumption could not be made[1] the tumor activity was measured several times over a period of at least 24 hours and the results were analyzed by the dual-exponent procedure. In most cases, a negligible amount of ^{224}Ra was found in the tumor (the activity was less than 1% of the whole tumor activity).

In some experiments insufficient freezing of the tumor led to partial pouring of the tissue content. In other experiments, the source was located so deep inside the tissue that several cuts in the tumor were required in order to find and extract the source. In such experiments, a non-negligble amount of ^{212}Pb could have been lost during the procedure itself. Therefore, the accuracy of the ^{212}Pb tumor calculated activity was compromised. It was difficult to estimate the exact inaccuracy of the evaluated ^{212}Pb tumor activity with regard to the "real" activity at tumor removal time and as a result the accuracy of the

[1]In the first experiments, when a problem with the source was detected or when it was possible

^{212}Pb leakage probability calculated for the problematic experiments was unknown. It is important to note that an effort was made in order to decrease activity loss. First, all tumor cuts were taken to measurement in the gamma counter when more than one existed. Also, three samples of 1 ml were taken from the formaldehyde solution during the first three hours after tumor removal from the mouse. These samples were measured in order to add the ^{212}Pb lost by leaking out of the tumor into the formaldehyde to the measured tumor activity. The lost activity was calculated by back extrapolation of the samples' measured activity multiplied by a proper factor in order to obtain the ^{212}Pb activity in the entire formaldehyde solution at tumor removal time.

Still, due to the inaccuracy problems described above, a second method to measure a more accurate value of ^{212}Pb tumor activity was developed. This procedure included a measurement of the tumor activity before source extraction. Immediately after tumor removal from the animal it was inserted into a vial with 2 ml of 4% formaldehyde solution, with the source still inside. The whole vial was taken into the gamma counter and the total activity was measured. After a single measurement the source was removed and its activity was measured several times over a period of 48-72 hours. The calculation of ^{212}Pb tumor activity at tumor removal time was done as follows. The source ^{212}Pb and ^{224}Ra activities at tumor measurement time were calculated using the dual-exponent procedure for t0 = tumor measurement time ($\Gamma^{src}_{Ra}(t_m)$,$\Gamma^{src}_{Pb}(t_m)$). If there is no ^{224}Ra in the tumor, then the first whole tumor measurement value is composed of ^{224}Ra activity of the source ($\Gamma^{src}_{Ra}(t_m)$),^{212}Pb activity in the tumor ($\Gamma^{tum}_{Pb}(t_m)$)[2] and ^{212}Pb activity on the source ($\Gamma^{src}_{Pb}(t_m)$). Insertion of $\Gamma^{src}_{Ra}(t_m)$,$\Gamma^{src}_{Pb}(t_m)$ into the expression for the total count rate in the gamma counter (equation 2.1) gave the^{212}Pb activity in the tumor at the measurement time:

$$\Gamma^{tum}_{Pb}(t_m) = \frac{CR(t_m) - 0.041\varepsilon\Gamma^{src}_{Ra}(t_m)}{0.436\varepsilon} - \Gamma^{src}_{Pb}(t_m)$$

The required value of ^{212}Pb activity at tumor removal was calculated taking account of the time difference between tumor removal and tumor measurement. During this period, ^{212}Pb was released into the tumor from the source. This released activity was found by first calculating the effective ^{212}Pb desorption probability ($P^{eff}_{des}(Pb)$) by using equation 3.34 and then inserting the calculated value into the following expression:

$$\Gamma^{add}_{Pb}(t_m - t_{TR}) = \frac{\lambda_{Pb}}{\lambda_{Pb} - \lambda_{Ra}} P^{eff}_{des}(Pb)\Gamma^{src}_{Ra}(t_{TR})(e^{-\lambda_{Ra}(t_m - t_{TR})} - e^{-\lambda_{Pb}(t_m - t_{TR})})$$

[2]since we used a close system, the vial, the sum of the activity in tumor and in formalin was considered as the activity inside the tumor

where $\Gamma_{Pb}^{add}(t_m - t_{TR})$ is the ^{212}Pb activity added into the tumor between its removal and its measurement. Finally, this value was subtracted from the tumor activity at tumor measurement time ($\Gamma_{Pb}^{tum}(t_m)$). Simple back extrapolation of the result yielded the requested tumor ^{212}Pb activity at tumor removal time.

A few experiments were made in order to estimate the difference between using the first and the second procedure for measuring the tumor activity at tumor removal time. Each tumor examined was measured with the source inside in order to find a more accurate ^{212}Pb activity value in the tumor as described above. After source removal, the tumor was measured again and the second ^{212}Pb activity value at tumor removal time was calculated. It was done by subtraction of the added ^{212}Pb activity from tumor removal to first tumor measurement and back extrapolation of the result to tumor removal time. This procedure was similar to the first tumor activity measurement procedure described above and enabled an estimation of its inaccuracy in comparison to the second procedure.

The experiments conducted included 47 tumors, 24 treated for a four day period (group A) and 23 treated for a two day period (group B). Group A was divided into 4 equal subgroups - small tumors (200-1000 mg) treated with a wire inserted in parallel to the tumor base, large tumors (1000 - 2000 mg) treated with a wire inserted in parallel to the tumor base, small tumors treated with a wire inserted perpendicular to the tumor base and large tumors treated with a wire inserted perpendicular to the tumor base. Group B was divided into the same 4 groups with 6,7,4 and 6 tumors respectively.

Figure 3.5 shows the summary of the experiments results. The X axis represents the absolute difference between the leakage probability values calculated from the first and the second measurements. For each value, the percentage of tumors (out of 47) with less or equal difference is represented by the Y value. As shown in the graph, for 85% of the tumors the absolute difference of leakage probability calculated was less than 10% and for 99% (all except one) it was less then 20% . Considering the fact that for the tumor with the calculated difference of 45%, finding the wire was difficult and required a lot of tumor cuts we can ignore this result. The addition of our knowledge (detailed in the following sections) regarding the high natural diversity of leakage probability, makes it safe to assume that the difference between the two measurement methods is not significant.

Leakage probability determination for changing parameters

In addition to the two experiments described in the previous section a third experiment with 23 tumors treated for a one day period was conducted (group C). This group contained 2 subgroups of 5 small tumors treated with sources that were inserted parallel and perpendicular to the tumor base, one subgroup of 8 large tumors treated with sources that were inserted perpendicular to the tumor base and one subgroup of 5 large tumors treated

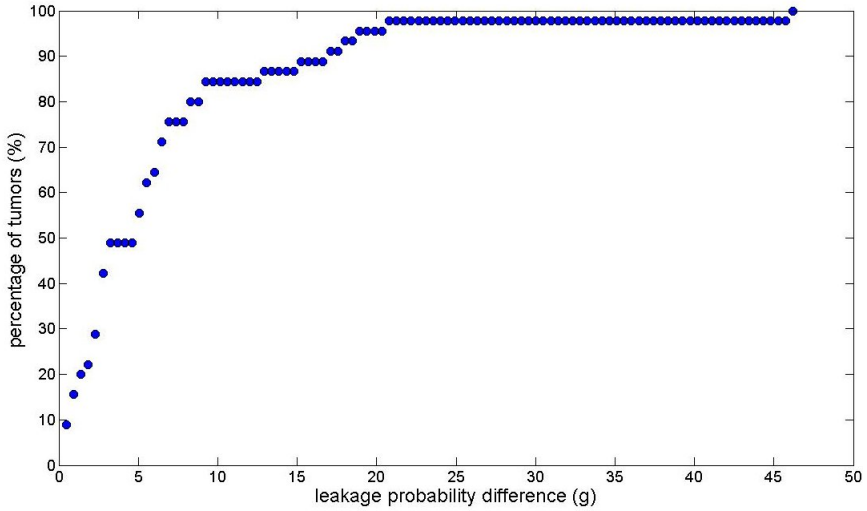

Figure 3.5: Cumulative percentage of tumors vs. absolute leakage probability difference

with sources that were inserted parallel to the tumor base. All tumors in this group were measured once before source removal and therefore their ^{212}Pb activity at the time they were removed from the animal was calculated by using the more accurate procedure.

The data gathered from the three experiments enables the comparison of leakage probability values (f_{Pbleak} and $P_{leak}(Pb)$) for tumors of different sizes, for tumors treated with sources inserted in different directions and for tumors treated for different times. ^{212}Pb leakage probability ($P_{leak}(Pb)$) as a function of the tumor mass and source insertion direction (parallel or perpendicular) for tumors treated with different treatment times is shown in figure 3.6. The leakage probability was calculated by using the procedure detailed above. The error range for each leakage value was calculated by running the numeric calculation for alpha estimation 1000 times. Each time, the numeric values used to calculate alpha (^{212}Pb activity inside the tumor, ^{212}Pb activity on the source etc.) was chosen at random to be in its possible error range with a normal probability distribution. The required leakage probability possible range was then calculated by the insertion of the possible alpha values range into equation 3.29.

According to the results shown in the plot the ^{212}Pb leakage probability for tumors with the same mass, same treatment time and same source insertion direction might be very different (up to 50% difference). In other words, the ^{212}Pb leakage probability values show large variability. Still, as was expected, a slight decrease of leakage probability as a function of tumor mass is detected for tumors treated for four and two days with the exception of two relatively high leakage values calculated for two tumors treated for two days both with a source parallel to the tumor base (figure 3.6 - b). As mentioned before, the orientation and position of the source inside the tumor cannot be exactly known . Therefore

we cannot exclude the possibility that the source was placed near the tumor periphery in these tumors, leading to a higher leakage of ^{212}Pb. With regard to the source insertion direction, a comparison between the leakage probability values for tumors treated for the same period but with different source insertion direction was made by performance of the Mann-Whitney U test. This is a statistical non-parametric test aimed at assessing whether two independent samples of observations come from the same distribution. According to this test no significant difference was found between leakage probability values for tumors treated with sources parallel to the tumor base or perpendicular.

Figure 3.7 shows a second view of the experiments results. The instantaneous ^{212}Pb leaking fraction (f_{Pbleak}) as a function of tumor mass for different tumor treatment times is presented in subplot (a) and ^{212}Pb leakage probability as a function of the same parameters is presented in subplot (b). The f_{Pbleak} value was calculated directly from tumor and source activity measurements without using any assumption regarding the ^{212}Pb removal rate. As can be seen in subplot (b), tumors with a similar mass (within the range of a few hundreds grams) are characterized by similar $P_{leak}(Pb)$ values regardless of treatment time. This hypothesis was checked by using the Mann-Whitney U test for comparison of the average leakage for tumors with similar masses. According to this test there is no significant difference between the leakage probability from similar mass tumors. This result can be explained by the assumption that the tumor mass correlates with the characteristic ^{212}Pb removal rate from the tumor (α_{Pb})[3]. Having the same removal rate from tumor immediately implies that tumors with similar mass will have the same $P_{leak}(Pb)$ value, since this entity is determined directly by α_{Pb} (equation 3.29).

As discussed in section 3.3.2 the assumption that the leakage rate is constant predicts that f_{Pbleak} will reach a stable constant value after about two days of treatment of a tumor with a given leakage rate (α_{Pb}). Moreover, the asymptotic f_{Pbleak} expected within a few days of treatment is very close to the leakage probability $P_{leak}(Pb)$ determined by α_{Pb} . This prediction is confirmed by the results shown in the subplot (a). The f_{Pbleak} values for tumors treated for four and two days are similar to one another and to the corresponding leakage probability value. f_{Pbleak} values for tumors treated for one day are smaller than the calculated leakage probability but are more similar to the values of tumors treated for four and two days when the tumor mass is smaller than 2000 mg. The agreement between the experimental results and the predicted behavior suggests that the linear model is reasonable when describing the average leakage behavior. Although it is clearly not an accurate description of the actual ^{212}Pb removal from tumor, it provides a good description of the general temporal behavior.

[3]There are many indications imp ling that tumor vasculature changes between tumors with different sizes. Also, we assume that blood vessels properties (morphology rehology etc.) have a great effect on ^{212}Pb leakage probability. It is therefore expected that similar size tumor will show a similar leakage.

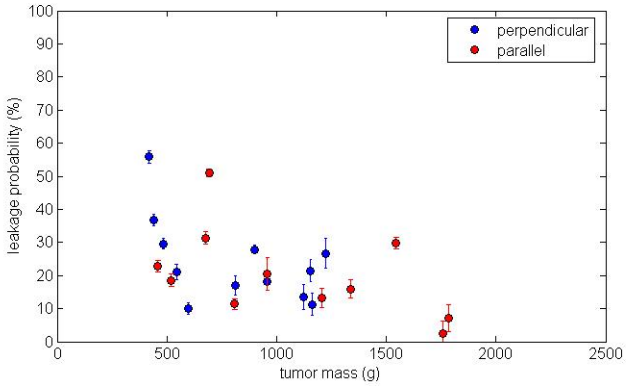

(a)

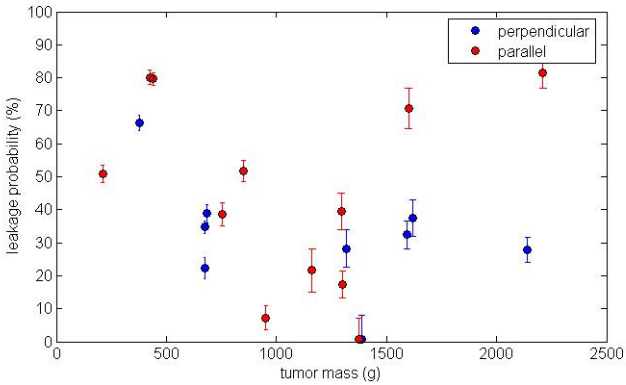

(b)

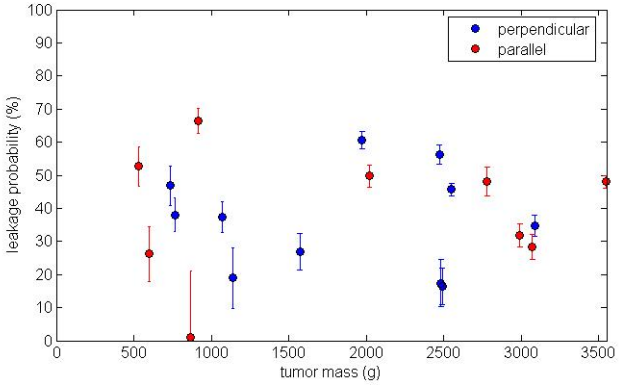

(c)

Figure 3.6: ^{212}Pb leakage probability for tumors treated with single DART source (a) ^{212}Pb leakage probability vs. tumor mass vs. source insertion direction (parallel or perpendicular) for tumors treated for 4 days (b) tumors treated for 2 days (c) tumors treated for 1 day

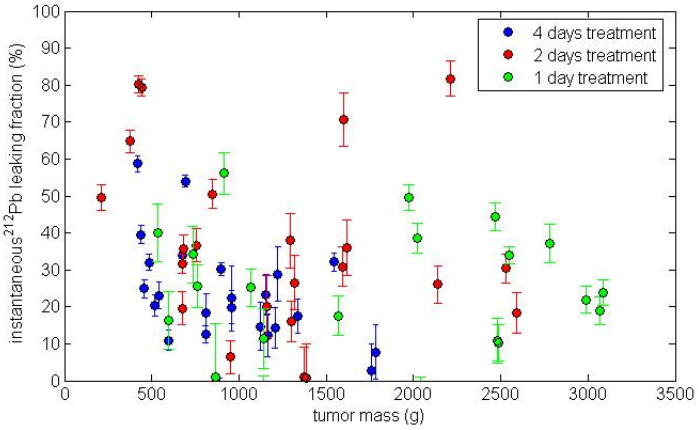

(a)

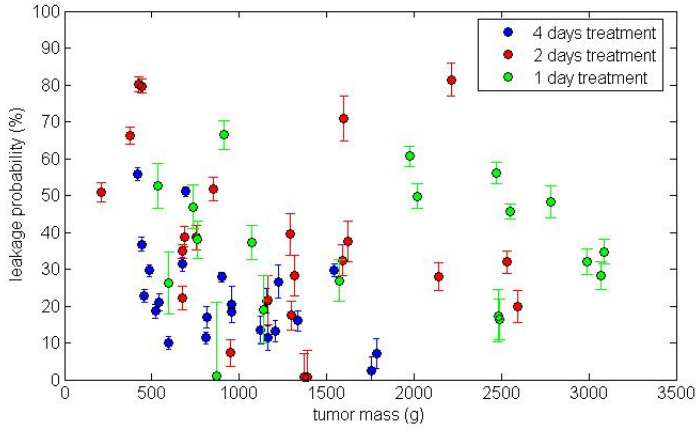

(b)

Figure 3.7: ^{212}Pb Leakage as function of tumor mass and treatment time (a) The instantaneous ^{212}Pb leaking fraction vs. tumor mass for different treatment times - 4 days treatment, 2 days treatment and 1 day treatment. f_{Pbleak} was calculated directly from measurements without using the linearity assumption (b)^{212}Pb leakage probability vs. tumor mass for different treatment times (4,2 and 1 day)

Tumors with mass higher than 2000 mg that were treated for one day show relatively high values of leakage probability in comparison with tumors of similar mass treated for a longer period. We would like to regard three aspects of this result. First, as explained above, variability in alpha values, and as a result in leakage probability, is theoretically expected since after one day of treatment the system does not reach equilibrium. This is shown explicitly by the error bars in both plots. The error range for leakage values of tumors treated for one day is much higher than that for tumors treated for two and four days due to possible error in alpha estimation. Second, as described in the introduction, the tumor mass is a time dependent variable. Though the change in tumor mass that might result from a few days of treatment is very small, a comparison of tumor mass after one day of treatment to the mass after four days of treatment might be problematic. We cannot exclude the possibility that ^{212}Pb removal rate from tumor treated for one day is similar to that of a tumor treated for four days for tumors that weigh 500 mg less. It is therefore important to regard the graph presentation as limited in its meaning and to remember that the use of tumor mass is made from practical reasons - the tumor mass is a variable which is very easy to measure and to present in a graph. Finally, tumors weighing more than 2000 mg at removal had a mass of the same order of magnitude at treatment beginning. This initial weight is higher than the initial weight of the tumors that were treated for two and four days. This difference might also explain the different results obtained for tumors treated for one day and for tumors treated for two and four days.

To conclude, SQ2 tumors show relatively high and variable leakage probability values. Also, it seems that the linearity assumption is justified when describing the general temporal processes occurring during the DART treatment. It is better to determine the tumor leakage probability after at least four days of treatment.

3.4 Comparison of ^{212}Pb leakage probability for different tumors

Remembering the motivation of this research stated in the introduction lead us to examine the ^{212}Pb leakage behavior for different tumor types. The data regarding this property was gathered from many different experiments in which SQ2, PANC02 and LL2 tumors were treated for four days with a single DART source. In most cases tumor activity was measured once after source removal and the tumors were taken for further experimental procedures (histology, Fuji or both). For some of the SQ2 tumors, the tumor activity was measured before source removal. The ensemble of all these experiments was analyzed in order to check for interesting patterns detectable despite the inherent noise in the measurements. Also, an assumption was made about the equivalence of the two methods used for measuring the

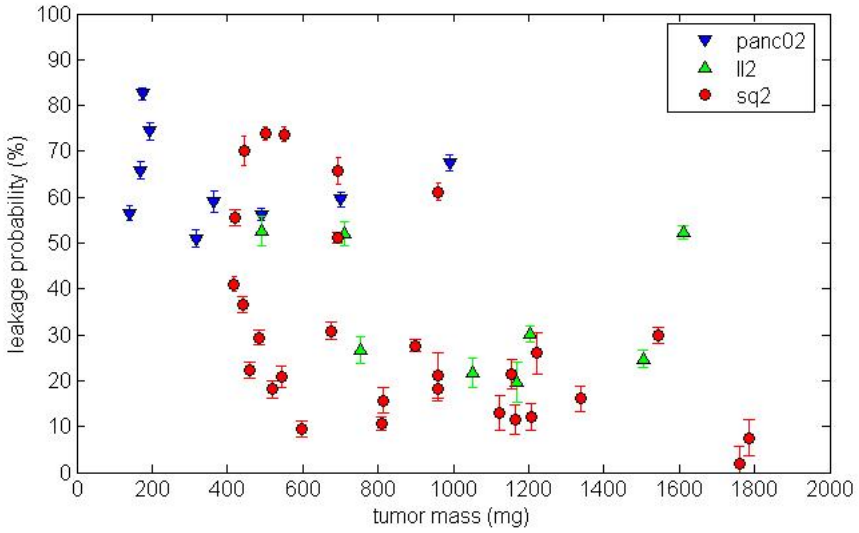

Figure 3.8: ^{212}Pb leakage probability as a function of tumor mass in different tumor types

^{212}Pb leakage probability (section 3.3.3).

The ^{212}Pb leakage probability as a function of tumor mass for SQ2, PANC02 and LL2 tumors is shown in figure 3.8. As can be seen, leakage values for PANC02 tumors with tumor mass higher than 1000 mg was not measured. This is because PANC02 tumors grow very slowly and usually do not reach large sizes. The tumors shown therefore represent characteristic PANC02 tumors for all comparison needs.

The first interesting result shown in the plot is the relatively high variability of leakage probability values for SQ2 in comparison to PANC02 tumors. The leakage probability value is relatively high and constant as a function of mass in PANC02 tumors (range between 55-85%) . SQ2 tumors with similar masses have a variable leakage value ranging from 80% to 10%. The second interesting result is that LL2 tumors are similar to each of the other tumor types, when regarding a different property. On the one hand, the wide range of LL2 tumors masses is similar to SQ2 tumors. Also, leakage probability values are smaller than those of PANC02 and range between 18-55%, similar to leakage probability values of SQ2 tumors. On the other hand, examination of the leakage values range shows that the absolute difference between the maximum and minimum value is similar to that for PANC02 tumors.

The results presented here provide an initial lead to an explanation of the different effect of DART treatment in different tumor types. When ^{212}Pb atoms leave the tumor at a faster rate, less damage is caused to the tumor tissue due to a decrease in the potential number of alpha decays inside the tumor and a corresponding decrease in effective dose. PANC02 tumors, which show relatively high values of leakage also showed the least significant re-

sponse to the DART treatment. In comparison, SQ2 tumors showed the most pronounced response to the DART treatment, a significant inhibition of tumor growth for most tumors treated with a single DART wire. Correspondingly, many SQ2 tumors had a small leakage value (smaller than that of PANC02), specifically tumors having large mass. LL2 tumors, with a more significant response to DART treatment than PANC02 tumor but less than SQ2 tumors, are located in the middle with regard to leakage probability values.

Chapter 4

Necrotic damage in tumors before and after treatment

Tumor tissue can be characterized by many biological features. Cell density, elastic fibers composition, blood vessel morphology, blood density and macromolecular constituent types are some of them. Theoretically, each feature can influence the movement of DART diffusing atoms inside the tumor and therefore can change the treatment results.

In this chapter we present a simple histological analysis of tissue sections taken from Squamous cell carcinoma, pancreatic and lung tumors treated with a single DART source and with an inert wire. The analysis goal is to obtain a qualitative understanding of the necrotic damage in tumors of different types before DART treatmentand and as the result of it. Necrosis is assumed to be one of the important factors affecting atom diffusion inside the tumor. Therefore, the understanding acquired in this chapter will later help us to analyze the differences between radiation distribution patterns inside tumors of different types.

4.1 The histology procedure

The histological sections used for the necrotic damage analysis were cut from SQ2, panc02 and LL2 tumors treated for 3-4 days with a single DART source or with an inert wire. All sections taken from tumors treated with a DART source were cut in the framework of 'HistoFuji experiments' (HRA experiments). In these experiments, representative sections were cut from successive 0.5 mm slabs of the tumor, starting from its edge. After measuring the spatial radiation distribution of these sections (see chapters 2 and 5 for details) they were subjected to H&E staining and histological analysis, along with additional pre-cut sections. Tumors treated with an inert wire were not, of course, used for 'HistoFuji' experiments. Histological sections were cut from these tumors by a standard procedure described in

chapter 2.

In order to compare necrosis damage of different tumors two rules were defined, aimed to enable the choosing of 'equivalent' representative sections from different tumors. For necrosis damage detection of DART treated tumor, the 'hottest' section that was measured on the Fujifilm plate was chosen. It was found using the radiation measurement analysis results - a map representing the spatial distribution of the dose inside a tissue section. The 'hottest' section was the section with the largest area exposed to an asymptotic dose higher or equal to 10Gy inside the tumor. It was assumed that the 'hot' section lies in perpendicular to the most active part of the source. For tumors that were treated with an inert wire the representative section was taken from the middle of the tumor. It was assumed that this location is equivalent to the location of the 'hottest' section in treated tumors.

4.2 Necrosis damage detection

Quantification and assessment of necrotic domains in each tumor section were done by delineating the damaged areas obtained by the staining and calculating the areas of the resulting polygons using imageJ free software (http://rsbweb.nih.gov/ij/). The total tumor area was calculated the same way. The necrosis fraction was estimated by division of both values for each section.

The real, 3-dimensional necrosis volume for the entire tumor can only be approximately estimated from the ensemble of individual 2-dimensional sections. Furthermore, the delineation of the necrotic domains is not exact due to the image resolution, the fuzzy biological borders and the subjectivity involved in this procedure. Still, by using the calculated necrotic domain area and the necrotic fraction we can learn about the differences between the tumor types as shown below.

4.3 Results

The following figures show a comparison of the necrotic area size in histological sections taken from SQ2, PANC02 and LL2 tumors treated for 4 days with inert wires, and with wires with initial ^{220}Rn release rate of $\sim$0.15, 0.28, 0.57 μCi. The necrotic domain is marked in each section with a white line. For each group of tumors treated with a similar activity the tissue properties are also presented in a plot. The plot shows the value of the non-necrotic area and the necrotic area for each tumor. A summarizing plot showing the value of the non-necrotic and the necrotic areas as a function of the source activity in SQ2 and PANC02 tumors is also presented.

As can be noticed, fewer histological sections were taken from lung tumors. This is

because the sections taken from LL2 treated tumors tend to get ripped during the staining procedure. The presented sections are the ones that 'survived' the whole procedure.

4.4 Discussion

The data gathered from the histological stainings show that the characteristic necrotic area changes between the different tumors and as a function of the source activity. Generally, we can say that the size of the necrotic area in treated and untreated SQ2 tumors is much higher than in similar PANC02 tumors. The size of the necrotic area in LL2 tumors is smaller than that of SQ2 tumors and higher than that of PANC02 tumors. Also, not surprisingly, increasing the source activity results in an increased necrotic area for all tumors types.

Comparison of the necrotic and non necrotic area of similar sized tumors treated with an inert wire (figure 4.1) shows that the necrotic volume fraction varies between a few percent in PANC02 tumors, about ten percent for LL2 tumor and about twenty percent for SQ2 tumors. Also, the treatment of SQ2, PANC02 and LL2 tumors with a DART source results in a larger necrotic area than observed in tumors treated with an inert wire while the relations between the necrotic area in different tumors stay unchanged. Figures 4.2-4.4 show that for each source activity the necrotic area is the largest in SQ2 tumors and the smallest in PANC02 tumors. Notice that the comparison in figure 4.2 is problematic due to differences between the whole tumor area of SQ2 tumors and PANC02 tumors. Still, this difference between the tumors is clearly shown in the two other images where the tumors compared had a similar area. With regard to the necrotic area change as a result of an increased activity it is shown that the necrotic area in SQ2 tumors increases from 10 mm^2 to 20 mm^2 when the source activity increases from 0.15 μCi to 0.55 μCi. The change in PANC02, by comparison is from 0.5 mm^2 to about 10 mm^2.

These results are very important when considering the radioisotopes transport inside the tumor. It is very likely that the movement of atoms entering a necrotic region is easier and faster than that of atoms entering a non necrotic region. It is therefore expected that the spread of ^{224}Ra daughters inside a necrotic tumor (SQ2 and LL2) will be larger than in a non necrotic tumor (PANC02). Also, releasing an increased amount of radioactive isotopes into the tumor (by increasing the source activity) is likely to lead to the formation of a larger necrotic domain as a result of an increased area with a therapeutically higher dose.

As shown in the following chapter, the suggested explanation is consistent with the results obtained from HRA experiment, showing that the spread of DART diffusing atoms in SQ2 tumors is much higher than in PANC02 tumors.

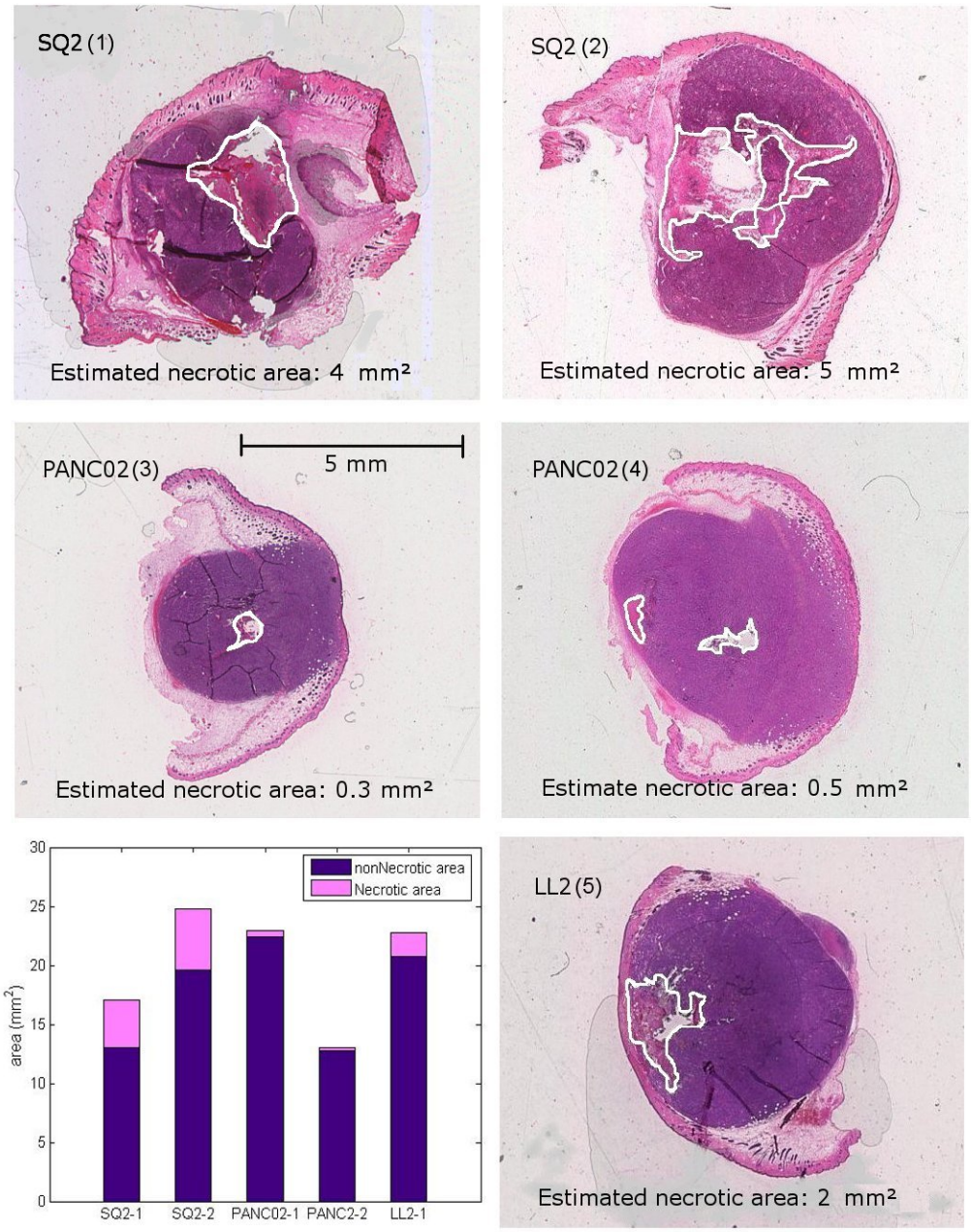

Figure 4.1: Histological sections of SQ2, PANC02 and LL2 tumors treated with inert wire. The estimated necrotic area is marked with a white line. The measured areas are as follows: (1) total section area: 17 mm^2, estimated necrotic area: 4 mm^2, necrotic fraction: 24% (2) total section area: 25 mm^2, estimated necrotic area: 5 mm^2, necrotic fraction: 21% (3) total section area: 13 mm^2, estimated necrotic area: 0.3 mm^2, necrotic fraction: 2% (4) total section area: 23 mm^2, estimated necrotic area: 0.5 mm^2, necrotic fraction: 2% (5) total section area: 23 mm^2, estimated necrotic area: 2 mm^2 , necrotic fraction: 9%

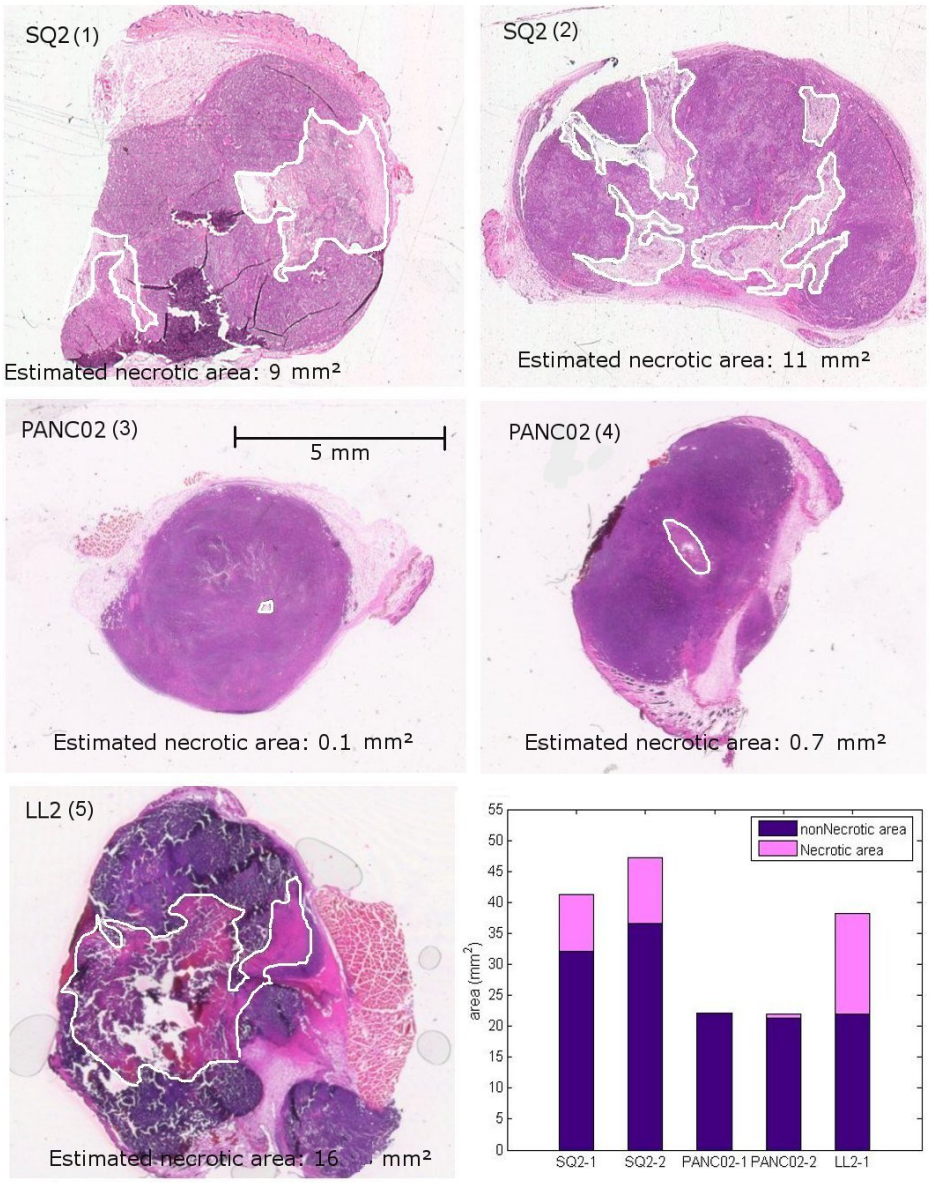

Figure 4.2: Histological sections of SQ2, PANC02 and LL2 tumors treated with DART wire with initial ^{220}Rn release rate of ˜0.15μCi. Necrotic area is marked with a white line. (1) total section area: 41 mm^2, estimated necrotic area: 9 mm^2, necrotic fraction: 22%, initial ^{220}Rn release rate: 0.16 μCi (2) total section area: 47 mm^2, estimated necrotic area: 11 mm^2, necrotic fraction: 23%, initial ^{220}Rn release rate: 0.14 μCi (3) total section area: 22 mm^2, estimated necrotic area: 0.1 mm^2, necrotic fraction: 0.2% , initial ^{220}Rn release rate: 0.16 μCi (4) total section area: 22 mm^2, estimated necrotic area: 0.7 mm^2, necrotic fraction: 3% , initial ^{220}Rn release rate: 0.2 μCi (5) total section area: 38 mm^2, estimated necrotic area: 16 mm^2, necrotic fraction: 43% , initial ^{220}Rn release rate: 0.11 μCi

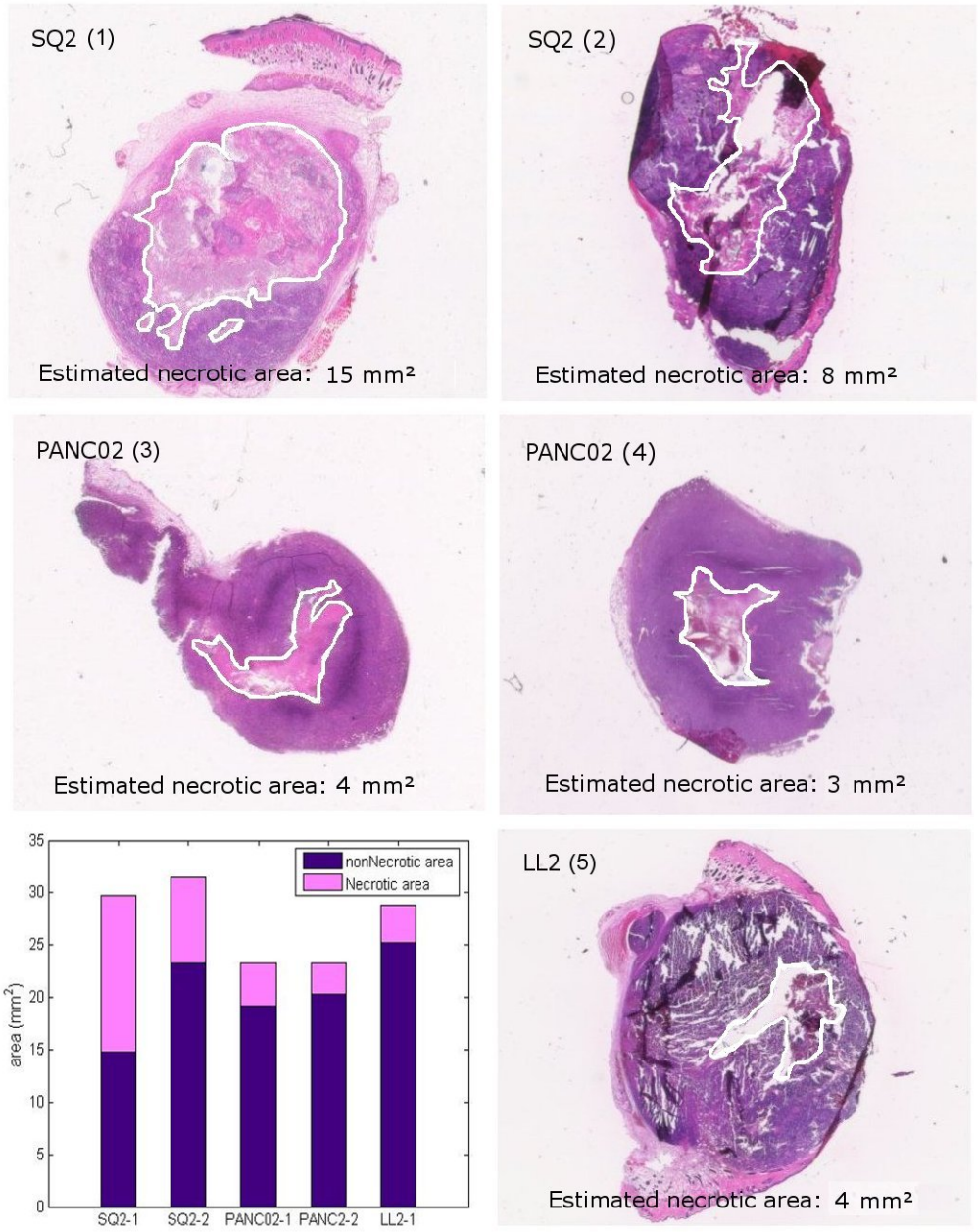

Figure 4.3: Histological sections of SQ2, PANC02 and LL2 tumors treated with DART wire with initial ^{220}Rn release rate of ˜0.25μCi. Necrotic area is marked with a white line. (1) total section area: 30 mm^2, estimated necrotic area: 15 mm^2, necrotic fraction: 50% , initial ^{220}Rn release rate: 0.31 μCi (2) total section area: 32 mm^2, estimated necrotic area: 8 mm^2, necrotic fraction: 26%, initial ^{220}Rn release rate: 0.21 μCi (3) total section area: 23 mm^2, estimated necrotic area: 4 mm^2, necrotic fraction: 18% , initial ^{220}Rn release rate: 0.25 μCi (4) total section area: 23 mm^2, estimated necrotic area: 3 mm^2, necrotic fraction: 13% , initial ^{220}Rn release rate: 0.29 μCi (4) total section area: 29 mm^2, estimated necrotic area: 4 mm^2, necrotic fraction: 13% , initial ^{220}Rn release rate: 0.22 μCi

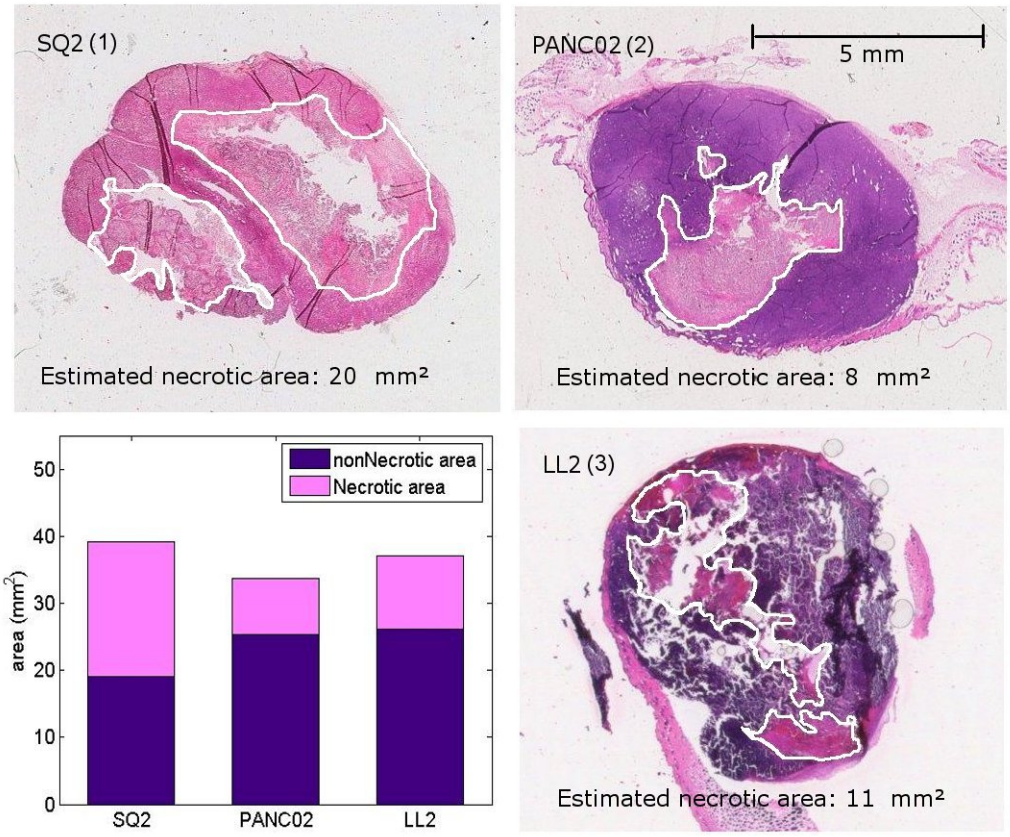

Figure 4.4: Histological sections of SQ2, PANC02 and LL2 tumors treated with a DART wire with initial ^{220}Rn release rate of ˜0.55μCi. The necrotic area is marked with a white line. (1) total section area: 39 mm^2, estimated necrotic area: 20 mm^2, necrotic fraction: 51% , initial Rn release rate: 0.57 μCi (2) total section area: 34 mm^2, estimated necrotic area: 8 mm^2, necrotic fraction: 25%, initial Rn release rate: 0.58 μCi (3) total section area: 37 mm^2, estimated necrotic area: 11 mm^2, necrotic fraction: 30% , initial Rn release rate: 0.57 μCi

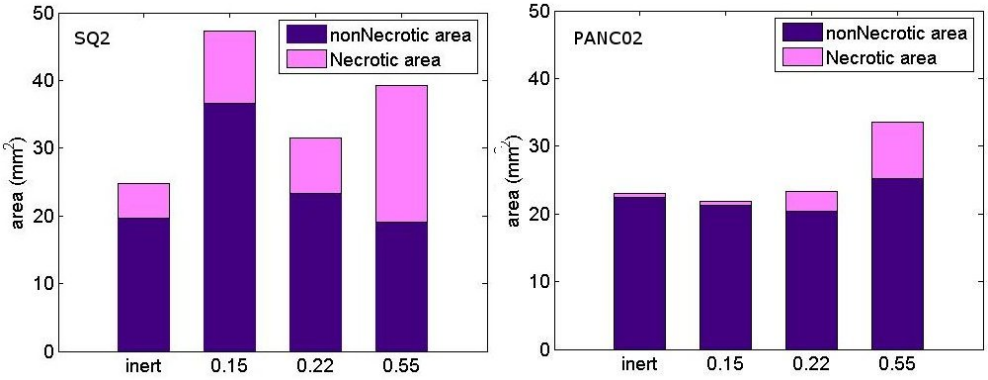

Figure 4.5: The necrotic and non-necrotic area in SQ2 and PANC02 tumors treated with various source acitivities for 4 days.

Chapter 5

Dose distribution measurements and analysis

So far we have developed an extensive discussion regarding the temporal and integral behavior of the alpha emitters diffusing atoms and about the tumor tissue histological properties. In order to consider the practical use of DART sources for treating cancer, additional work regarding the spatial distribution of these atoms inside the tumor is required. The theoretical and experimental aspects that enabled preliminary dosimetry calculations for treated tumors were developed by L. Arazi and T. Cooks as part of their Ph.D. work. A thorough description of the theoretical diffusion-leakage model and of the experimental setup that was developed can be found in Arazi's work [14]. In this chapter, the most important results of the theoretical model are described and their meaning in the context of different tumor types is discussed. Also, an extension to the diffusion-leakage model taking into account the possible drift of the diffusing atoms in the tumor due to the blood and the interstitial fluid flow is presented. Finally, the results of the experimental work conducted to measure the dose distribution in SQ2, PANC02 and LL2 tumors following the DART treatment are shown and discussed.

5.1 Diffusing atoms transport in the tissue - theoretical aspects

After recoiling into the tumor, some of the ^{224}Ra daughters may interact with the tissue constituents to form various molecules and some may start moving in the tumor as single atoms. In any case, the movement of the atoms\created molecule[1] inside the tumor is controlled by two major mechanisms - diffusion and convection. Both processes change in

[1]For clarity, we will regard a molecule from now on

space and time and depend on the chemical properties of the diffusing molecule and on the medium itself. The transport of each molecule might differ between tumors and normal tissue as well as between different tumor types.

The tumor interstitium is a complex network structure composed of elastic fibers and collagen interspersed with macromolecular constituents and the interstitial fluid to form a gel-like medium. It is sometimes convenient to divide the interstitial space into two compartments: the colloid rich gel space and the colloid poor free fluid space. The movement of molecules inside the fluid phase of the medium depends on its size, charge and shape as well as its interaction with the tissue constituents. In comparison to normal tissues, tumors are usually characterized by a large interstitial space, which can comprise up to 60% of the tumor volume (the interstitial volume in normal brain tissue, for comparison is 7%). Although the implications of a large interstitial space are not completely understood, it seems reasonable to assume that a large "free-fluid" space would offer less resistance to interstitial transport than a small space. In any case, the diversity in space volume values might be one of the causes of the differences in diffusion rates between different tumors [11].

As discussed in the previous section, the necrotic domains volume inside the tissue differ between different tumor types. Their total volume ranges between 50% of the total tumor volume to a negligible fraction. Changes in the necrotic volume might influence the mobility of the diffusing atoms inside the tumor. The movement of a diffusing atom inside a necrotic domain is assumed to be easier than in a non necrotic domain.

The tumor vasculature is another tissue constituent that changes between tumor types and is very different in comparison to normal tissue. It is highly chaotic in nature and the clear structural order which characterizes normal tissue does not exist. It is hard to distinguish between different blood vessel types such as arteries, arterioles and capillaries. Also, there are many shunts and dead ends. The blood vessels themselves are highly porous and the typical blood flow velocity is an order of magnitude lower than in normal capillaries (0.1-0.3 mm/sec). The vessels morphology, blood velocity, viscosity and other parameters that characterize the tumor vasculature contribute and affect the distribution of the molecules in the tumor. In addition, tumor vasculature has an important role in the evacuation of the tumor constituents out of the tissue. The removal rate of ^{224}Ra recoiling daughters from the tumor has a large influence on the atoms distribution, and it also varies between different tumors [18].

This short description should be sufficient to clarify the difficulties involved in trying to create an accurate model describing the spatial and temporal behavior of the diffusing atoms inside the tumor. A too general model for tumors will not reflect the possible differences between tumor types. Moreover, it is impossible to measure the exact properties of each tumor. There is no imaging method today, that provides the data of the quality required for

a quantitative analysis regarding the DART transport processes. Also, one cannot expect complete knowledge of the effective diffusion coefficients of the migrating atoms which depend on the tissue ingredients. Finally, tumor tissue changes with time, and probably in an accelerated rate due to the DART treatment effect. It is unrealistic to follow the exact temporal changes in tissue properties. [18]

Still, in order to enable practical use of DART as a cancer treatment, a general model that provides simple quantitative estimates is required. In order to start we initially write a very general transport equation similar for all isotopes, attempting to describe the major processes that affect the number density of the atoms inside the tumor as time progresses:

$$\frac{\partial n_i(\mathbf{r},t)}{\partial t} + \nabla \cdot \mathbf{J}_i = s_i - \lambda_i n_i - \alpha_i n_i \tag{5.1}$$

$\lambda_i n_i$ - represents the isotope decay with a characteristic half life, $\nabla \cdot \mathbf{J}_i$ - indicates the spatial distribution change in atoms flux ($\mathbf{J}_i$) due to diffusion and convection, s_i - the source term, represents the entry of additional atoms into the tumor following its parent decay, and $\alpha_i n_i$ - reflects the assumption that the removal rate of the atoms from the tumor is constant.

Several assumptions, based on the knowledge gathered from the literature and on our experimental data can be made with regard to each isotope in ^{224}Ra decay chain. By using these assumptions we get approximate solutions for the transport equation 5.1 that enables the performance of first order dosimetry calculations. These assumptions are described below.

5.2 The Diffusion-Leakage model

As mentioned in section 3.2, the spatial distribution of only three isotopes in the ^{224}Ra decay chain - ^{220}Rn, ^{212}Pb and ^{212}Bi - need be considered. The spatial distribution of each of the shorter lived members of the decay chain is essentially identical to that of its respective parent. Consider, for example, ^{216}Po whose half-life is 0.15 sec and whose diffusion coefficient in tissue is approximately $D_{Po216} = 1 \cdot 10^{-6} cm^2/sec$. Using these values, the diffusion length of ^{216}Po is $dx_{po} \sim \sqrt{D_{Po216}\tau_{Po216}} \sim 4\mu m$. Thus, ^{216}Po is effectively in local secular equilibrium with ^{220}Rn. The same holds for the $0.3\mu sec$ half-life ^{212}Po, which is in local secular equilibrium with ^{212}Bi. Finally, ^{208}Tl, with a 3 min half-life may show some redistribution relative to ^{212}Bi, but its effect is of little dosimetric importance since it does not emit alpha particles.

The Diffusion-Leakage model developed for describing the spatial and temporal behavior of ^{220}Rn, ^{212}Pb and ^{212}Bi in the tumor is very simplistic and is based on the following assumptions:

- The migration of the atoms inside the tumor is predominantly diffusive in nature.

Convective processes are characterized by a short correlation length (relative to therapeutically significant distances) and can thus be incorporated into an effective diffusion coefficient.

- The tissue is homogeneous and isotropic. The effective diffusion coefficients are constant in space.
- The diffusion coefficients are constant in time. Temporal changes in the properties of the tissue are not considered.
- ^{212}Pb likely binds to many different kinds of proteins in the tumor. Its migration can be described by using a single effective diffusion coefficient representing the average over all ^{212}Pb molecular species.
- ^{212}Pb atoms reaching major blood vessels may be trapped in red blood cells and immediately cleared from the tumor. This process is described by a uniform sink term which is independent of space and time - α_{Pb}. This assumption was already discussed extensively in chapter 3.
- Since the short lived ^{220}Rn atoms are free to diffuse with no chemical interaction through blood vessels and RBCs, the equation for ^{220}Rn does not include a sink term (i.e., blood vessels do not act as traps for ^{220}Rn).
- The diffusion equation for ^{212}Bi does include a sink term - α_{Bi}. However, the experimental data that was presented in [14] showed that it is a second order effect.

Under these assumptions, the number densities of ^{220}Rn, ^{212}Pb and ^{212}Bi are governed by the following diffusion equations:

$$\frac{\partial n_{Rn}}{\partial t} = D_{Rn}\nabla^2 n_{Rn} + s_{Rn} - \lambda_{Rn} n_{Rn} \tag{5.2}$$

$$\frac{\partial n_{Pb}}{\partial t} = D_{Pb}\nabla^2 n_{Pb} + s_{Pb} - \lambda_{Pb} n_{Pb} - \alpha_{Pb} n_{Pb} \tag{5.3}$$

$$\frac{\partial n_{Bi}}{\partial t} = D_{Bi}\nabla^2 n_{Bi} + s_{Bi} - \lambda_{Bi} n_{Bi} - \alpha_{Bi} n_{Bi} \tag{5.4}$$

where D_{Rn}, D_{Pb}, D_{Bi} are the constant effective diffusion coefficients of ^{220}Rn, ^{212}Pb and ^{212}Bi respectively, and α_{Pb}, α_{Bi} are the constant leakage rate coefficients of ^{212}Pb and ^{212}Bi respectively.

5.2.1 Model solutions and the alpha particle dose - theoretical analysis

In this section we present the final solutions of diffusion-leakage equations for an ideal point source. For ^{220}Rn, the complete time dependent solution and the asymptotic solution is shown . For ^{212}Pb and ^{212}Bi we discuss the numerical solutions for the time dependent equations together with important approximations that are later used for the evaluation of these isotopes distribution in real tumors.

The solutions of the diffusion-leakage equations are used in order to estimate the alpha particle dose contributed by DART diffusing atoms. The observed dose is approximated by the assumption that the energy of each alpha decay is deposited locally. We divide the alpha particle dose into two components which are discussed separately. The dose contributed by ^{220}Rn and its daughter ^{216}Po (both in local secular equilibrium) with a spatial distribution governed by the ^{220}Rn diffusion length is shown first. Then, the contribution of alpha particles emitted by ^{212}Bi and ^{212}Po at distances determined by the ^{212}Pb diffusion length is presented.

The prediction of the diffusion-leakage model depends on the choice of numerical values for its parameters - the effective diffusion coefficients and the leakage rate constants. These parameter ranges differ for each isotope and from tumor to tumor. In order to estimate the relevant ranges for our model we rely on experimental data and on the literature. As noted above, the diffusion-leakage model was developed by L. Arazi. The experimental data which he used for the theoretical analysis was obtained from mice bearing metastatic SCC tumors derived from the SQ2 cell line. In this research, additional data regarding the isotopes spatial distribution in SQ2 tumors and in other tumor types - pancreas (derived from PANC02) and lung (LL2) was collected. We use all the experimental data in order to estimate the relevant parameters for each tumor type. The range of those parameters and the reasons for choosing them as well as their effect on the model predictions are shown in this section.

The theoretical model is solved for a point source. In order to use it to analyze the results of experiments conducted with real DART sources (wires of a few mm length), the sources are later approximated as a superposition of point increment along a line. This approximation is valid as long as non linear effects can be neglected.

5.2.2 ^{220}Rn distribution in the tumor

Time dependent and asymptotic solutions

The solution for ^{220}Rn is based on the assumption that it enters the tumor directly from the source following ^{224}Ra decay and not by the decay of ^{224}Ra inside the tumor. This assumption is valid when a negligible amount of ^{224}Ra leaves the source and enters the tumor during the treatment. This is usually the case. ^{224}Ra release to the tumor can be

limited to less than 0.5% of its initial load and only a fraction of the ^{224}Ra released stays inside the tumor.

The time-dependent ^{220}Rn diffusion equation for a point source in an infinite homogeneous and isotropic medium is given by:

$$\frac{\partial n_{Rn}}{\partial t} = \frac{D_{Rn}}{r^2}\frac{\partial}{\partial r}(r^2\frac{\partial n_{Rn}}{\partial r}) - \lambda_{Rn} n_{Rn} \tag{5.5}$$

with the boundary condition:

$$\lim_{r\to 0} 4\pi r^2 j^{asy}_{Rn}(r,t) = P_{des}(Rn)\Gamma^{src}_{Ra}(0)e^{-\lambda_{Ra}t}$$

and the initial condition $n_{Rn}(0) = 0$.

The general solution achieved by using the Laplace transform, for time t and distance r from the source is:

$$n_{Rn}(r,t) = \frac{P_{des}(Rn)\Gamma^{src}_{Ra}(0)e^{-\lambda_{Ra}t}}{8(\pi D_{Rn})^{3/2}} \int_0^t \frac{1}{\tau^{3/2}} e^{-\frac{r^2}{4D_{Rn}\tau}} e^{-(\lambda_{Rn}-\lambda_{Ra})\tau} d\tau \tag{5.6}$$

A few minutes after source insertion, the solution for ^{220}Rn converges to its asymptotic form at every point inside the tumor, having a temporal part controlled by the ^{224}Ra half life. The asymptotic solution is calculated by changing the integral limit to $t \to \infty$. The result is:

$$n^{asy}_{Rn}(r,t) = \frac{P_{des}(Rn)\Gamma^{src}_{Ra}(0)e^{-\lambda_{Ra}t}}{4\pi D_{Rn}} \frac{e^{-r/L_{Rn}}}{r} \tag{5.7}$$

where L_{Rn} is the *effective diffusion length* defined by:

$$L_{Rn} = \sqrt{\frac{D_{Rn}}{\lambda_{Rn} - \lambda_{Ra}}} \tag{5.8}$$

^{220}Rn effective diffusion coefficient - numerical range

Direct measurement of the ^{220}Rn distribution inside the tumor *in vivo* is very difficult to perform, primarily because of its short half-life (55.6 sec). ^{220}Rn has no gamma emissions and its presence can only be detected by an immediate measurement of the alpha particle it emits. Such measurements are very complicated in practice. Therefore, the numerical value for the ^{220}Rn diffusion coefficient range is mainly estimated by using information from the literature. The relevant considerations are as follows:

- The diffusion coefficient of radon in water at 37^oC is $1.9 \cdot 10^{-5} cm^2/sec$ [1].
- In the NRC report on radon in drinking water the effective diffusion coefficient of

^{220}Rn through the stomach wall was assumed to be $0.5{\cdot}10^{-5}$ cm^2/sec [19].

- The histological data presented in chapter 4 show that the average necrosis percentage in SQ2 tumors is much higher than in PANC02 tumors. The necrosis percentage in LL2 tumors is higher than in PANC02 tumors and smaller than in SQ2 tumors. Elevated necrosis is expected to increase the effective diffusion coefficient since the atom movement inside the tissue is easier.

- Doseimetry measurements in SQ2, PANC02 and LL2 tumors suggest that the effective ^{220}Rn diffusion coefficient is in the range $(0.5{-}1.8){\cdot}10^{-5}cm^2/sec$, $(2{-}5){\cdot}10^{-6}cm^2/sec$ and $(0.5-1.8)\cdot 10^{-5}cm^2/sec$ respectively.

The effective diffusion coefficient of ^{220}Rn is assumed to be in the range $(0.2$ - $2)\cdot 10^{-5}$ cm^2/sec . We assume that the ^{220}Rn diffusion coefficient in PANC02 tumors is closer to the lower limit and to the value suggested by the NRC report due to these tumors histological properties. As presented in chapter 4 the necrotic domains in PANC02 tumors are very small. We assume that the PANC02 tissue is more similar to normal tissue than to necrotic tissue and therefore we expect that the diffusion coefficient value will also be closer to the value suggested for normal tissues (stomach wall). The upper limit value, which is the diffusion coefficient of ^{220}Rn in water, is probably closer to the diffusion value in SQ2 and LL2 tumors since they are relatively necrotic. According to the results of the dosimetry measurements we assume that a reasonable reference value for the ^{220}Rn diffusion coefficient in these tumors will be in the range $(1-1.5)\cdot 10^{-5}$ cm^2/sec.

The effective diffusion length that corresponds to the suggested diffusion coefficients (defined by equation 5.8) is between 0.13-0.4 mm for all tumor types.

The alpha particle dose

The alpha particle dose contributed by ^{220}Rn and ^{216}Po from source insertion to time t can be calculated to an accuracy of $\sim 10^{-4}$ by neglecting the initial buildup of ^{220}Rn inside the tumor and assuming that from t=0 the ^{220}Rn activity attain its asymptotic form. Insertion of the asymptotic solution for the ^{220}Rn number density into the expression that defines the dose gives (5.6):

$$Dose_\alpha(RnPo;\mathbf{r},t)=\frac{E_\alpha(RnPo)}{\rho}\int_0^t \lambda_{Rn}n_{Rn}(r,t^{'})dt^{'}=$$
$$\frac{\lambda_{Rn}P_{des}(Rn)\Gamma_{Ra}^{src}(0)E_\alpha(RnPo)}{4\pi\rho D_{Rn}}\frac{e^{-r/L_{Rn}}}{r}(1-e^{t/\tau_{Rn}})$$

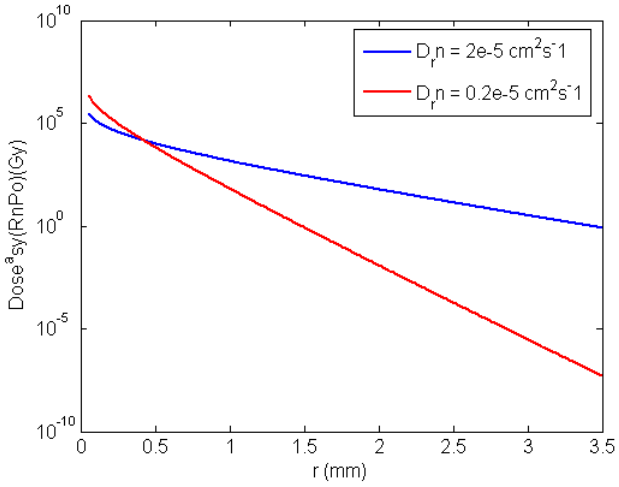

Figure 5.1: The asymptotic dose contributed by ^{220}Rn\$^{216}$Po alpha decays vs. distance from source. The dose was calculated for the lower and upper bound values of ^{220}Rn effective diffusion coefficient - $0.5 \cdot 10^{-5} - 2 \cdot 10^{-5} cm^2/sec$. The initial ^{220}Rn release rate was set to be $1\mu Ci$.

$E_\alpha(RnPo)$ is the total alpha particle energy of ^{220}Rn and ^{216}Po, $E_\alpha(RnPo) = 13.07MeV = 2.09 \cdot 10^{-12}J$ and ρ is the tissue density.

The asymptotic dose is defined as the dose delivered from source insertion to infinity. It is calculated by changing the integral limit to $t \to \infty$:

$$Dose_\alpha^{asy}(RnPo; \mathbf{r}, t) = \frac{E_\alpha(RnPo)}{\rho} \int_0^\infty \lambda_{Rn} n_{Rn}(r, t')dt' = \frac{\lambda_{Rn} P_{des}(Rn) \Gamma_{Ra}^{src}(0) E_\alpha(RnPo)}{4\pi\rho D_{Rn}} \frac{e^{-r/L_{Rn}}}{r} \tau_{Ra}$$

Figure 5.1 shows the asymptotic dose governed by ^{220}Rn/^{216}Po alpha decays as a function of the distance from a point source with an initial ^{220}Rn release rate $P_{des}(Rn)\Gamma_{Ra}^{src}(0) = 1\mu ci$. The dose is plotted for the two extreme values of the ^{220}Rn effective diffusion coefficient.

Figure 5.2 shows the diameters of spherical regions around a point source receiving an asymptotic dose higher than 10 and 30 Gy, respectively, as a result of ^{220}Rn and ^{216}Po alpha decays. This variable - defined as *effective diameter* is plotted as a function of the initial ^{220}Rn release rate from a point source. Due to the reasons detailed above, L_{Rn} was assumed to be in the range 0.1-0.4 mm.

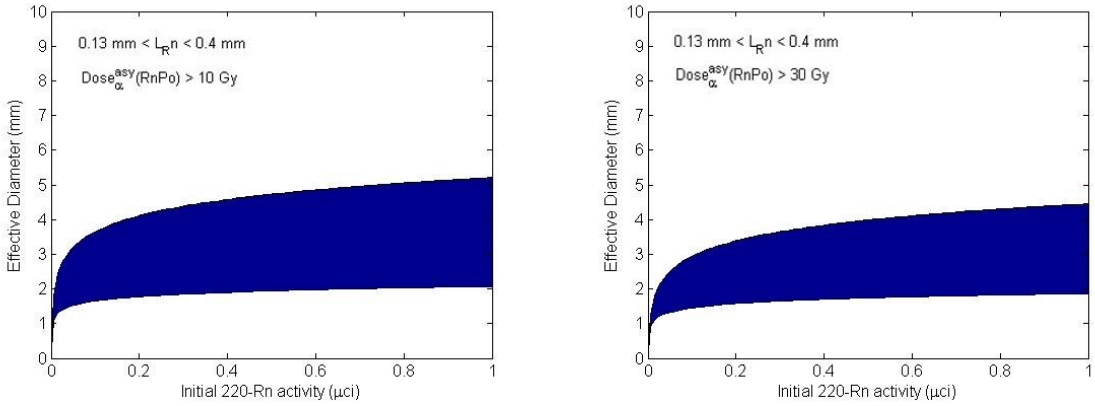

(a) (b)

Figure 5.2: Effective diameter of the spherical region receiving an asymptotic ^{220}Rn/^{216}Po alpha particle dose as function of initial source release. (a) The diameter of a region receiving more than 10 Gy (a) The diameter of a region receiving more than 30 Gy

5.2.3 ^{212}Pb distribution in the tumor

Time dependent and asymptotic solutions

The time-dependent diffusion-leakage equation for ^{212}Pb in uniform homogeneous tissue is:

$$\frac{\partial n_{Pb}}{\partial t} = \frac{D_{Pb}}{r^2}\frac{\partial}{\partial r}(r^2\frac{\partial n_{Pb}}{\partial r}) + s_{Pb} - (\lambda_{Pb} + \alpha_{Pb})n_{Pb} \tag{5.9}$$

The source term can be written as (see section 3.2):

$$s_{Pb} = \lambda_{Rn}n_{Rn} + (P_{des}^{eff}(Pb) - P_{des}(Rn))\Gamma_{Ra}^{src}(0)e^{-\lambda_{Ra}t}\delta(r) \tag{5.10}$$

the boundary condition is:

$$\lim_{r\to 0} 4\pi r^2 j_{Pb}^{asy}(r,t) = (P_{des}^{eff}(Pb) - P_{des}(Rn))\Gamma_{Ra}^{src}(0)e^{-\lambda_{Ra}t} \tag{5.11}$$

and the initial condition is: $n_{Pb}(0) = 0$.

The exact solution of this equation can be calculated numerically. The exact solution will be used below, after introducing the effective diffusion coefficients range and in comparison to the approximate solutions.

The asymptotic solution is calculated by assuming that within several ^{212}Pb half-lives from source insertion, the ^{212}Pb number density takes the following form:

$$n_{Pb}(\mathbf{r},t) = n_{Rn}(\mathbf{r})\hat{e}^{-\lambda_{Ra}t} \tag{5.12}$$

Substituting equation 5.12 and the ^{220}Rn asymptotic solution (equation 5.7) into the diffusion-leakage equation yields the following solution:

$$n_{Pb}^{asy}(r,t) = (A_{Pb}\frac{e^{-r/L_{Rn}}}{r} + B_{Pb}\frac{e^{-r/L_{Pb}}}{r})e^{-\lambda_{Ra}t} \tag{5.13}$$

$$A_{Pb} = \left(\frac{L_{Rn}^2 L_{Pb}^2}{L_{Rn}^2 - L_{Pb}^2}\right)\frac{\lambda_{Rn}}{D_{Pb}}\frac{P_{des}(Rn)\Gamma_{Ra}^{src}(0)}{4\pi D_{Rn}} \tag{5.14}$$

$$B_{Pb} = \frac{(P_{des}^{eff}(Pb) - P_{des}(Rn))\Gamma_{Ra}^{src}(0)}{4\pi D_{Pb}} - A_{Pb} \tag{5.15}$$

$$L_{pb} = \sqrt{\frac{D_{Pb}}{\lambda_{Pb} + \alpha_{Pb} - \lambda_{Ra}}} \tag{5.16}$$

As for ^{220}Rn, we define L_{pb} - *the effective ^{212}Pb diffusion length.*

An important approximation to this solution is the 'Pb only' approximation. In some cases, we can assume that the ^{220}Rn diffusion length is very short in comparison to the ^{212}Pb diffusion length and moreover, that it is very close to zero. The asymptotic solution then becomes:

$$n_{Pb}^{asy}(r,t) \approx B_{Pb}\frac{e^{-r/L_{Pb}}}{r}e^{-\lambda_{Ra}t} \approx_{L_{Rn}\to 0} \frac{P_{des}^{eff}(Pb)\Gamma_{Ra}^{src}(0)e^{-\lambda_{Ra}t}}{4\pi D_{Pb}}\frac{e^{-r/L_{Pb}}}{r}$$

An alternative approximation that describes the opposite case is the 'Rn only' approximation. If $L_{pb} \ll L_{Rn}$ the spread of ^{212}Pb is determined by L_{Rn} and the asymptotic solution becomes:

$$n_{Pb}^{asy}(r,t) \approx A_{Pb}\frac{e^{-r/L_{Rn}}}{r}e^{-\lambda_{Ra}t} \approx \frac{\lambda_{Rn}}{\lambda_{Pb} + \alpha_{Pb} - \lambda_{Ra}}\frac{P_{des}(Rn)\Gamma_{Ra}^{src}(0)e^{-\lambda_{Ra}t}}{4\pi D_{Pb}}\frac{e^{-r/L_{Rn}}}{r}$$

^{212}Pb effective diffusion coefficient range

The experimental data from mice bearing SQ2, PANC02 and LL2 tumors implies that the ^{212}Pb effective diffusion coefficient varies for different histologies. The data that enables a numerical estimation of the effective coefficient is the following:

- As presented in chapter 3 the ratio $\frac{\alpha_{Pb}}{\lambda_{Pb}}$ ranges between 0.1-2 in SQ2 tumors, 0.3-1.1 in LL2 tumors and 1-3.5 in PANC02 tumors. Taking $\alpha_{Pb} = \lambda_{Pb}$ as a representative case for SQ2 tumors and $\alpha_{Pb} = 2.5\lambda_{Pb}$ for PANC02 tumors and assuming that ^{212}Pb effective diffusion coefficient is the same in both tissues, the expected ratio between the effective lengths can be calculated. Substituting these values into the ^{212}Pb effective

diffusion lengths of the two tumors types (equation 5.16) and dividing gives:

$$\frac{L_{Pb}^{SCC_2}}{L_{Pb}^{PANC}} \approx \sqrt{\frac{\frac{D_{Pb}}{2\lambda_{Pb}-\lambda_{Ra}}}{\frac{D_{Pb}}{3.5\lambda_{Pb}-\lambda_{Ra}}}} = \sqrt{\frac{3.5\lambda_{Pb}}{2\lambda_{Pb}}} \approx 1.32$$

This result implies that the average ^{212}Pb effective diffusion length in SQ2 tumors is longer than in PANC02 tumors by a factor of at least 1.3 (when the effective diffusion coefficient is the same for both tissues). Using the same set of assumptions implies that the effective diffusion length in LL2 tumors will be similar to that of SQ2 tumors and longer than the effective length of PANC02 tumors.

- The considerations regarding the effect of tumor histology on ^{220}Rn diffusion apply to ^{212}Pb diffusion as well. It is expected that the ^{212}Pb diffusion coefficient in SQ2 tumors will be higher than in PANC02 tumors due to the higher necrosis percentage. Moreover, the difference between the diffusion coefficient in the two tumors is assumed to be more significance for ^{212}Pb than for ^{220}Rn since ^{212}Pb atoms interact with tumor components while ^{220}Rn atoms do not. It is reasonable to assume that non necrotic tumor tissues contains more molecular components that can bind to ^{212}Pb and inhibit its motion inside the tumor (leading to a decrease in the effective diffusion length).

- As mentioned in chapter 3, ^{212}Pb is likely bound to proteins inside the tumor. Works aimed to identify lead binding proteins in healthy tissues show that lead can bind to many kinds of proteins. These proteins vary in different tissues and span a large spectrum of masses, ranging between 5 to 280 kDa [14]. The results of a study of the diffusion coefficient range of dextrans (20-150 kDa) in VX2 carcinoma can be used for a rough estimate of the ^{212}Pb diffusion coefficient value and its possible range in different tissues and for different molecular masses [11]. It was found that dextrans diffusion coefficient can be approximated by the formula: $D = aM^{-b}$ for both tumor ($a = 2.51 \cdot 10^{-2}, b = -1.14$) and normal tissues ($a = 10^6, b = -2.96$). The diffusion coefficient value range in the tumor for the relevant mass spectrum of lead binding proteins is therefore: $3.1 \cdot 10^{-7} - 3.2 \cdot 10^{-8}$ cm^2/sec. In normal tissues, the diffusion coefficient values for the same molecules might be at least an order-of-magnitude lower.

- Dosimetry measurements in SQ2, PANC02 and LL2 tumors suggest that the effective ^{212}Pb diffusion coefficient is in the range $(0.3-4)\cdot 10^{-7} cm^2/sec$ (assuming that ^{220}Rn is concentrated closer to the source), $(0.5-3)\cdot 10^{-8} cm^2/sec$ and $(1-2)\cdot 10^{-7} cm^2/sec$ respectively.

To conclude, we assign different expected diffusion coefficient ranges to different tumor types. For SQ2 and LL2 tumors, we assume that the diffusion coefficient is in the range $(1-4)\cdot 10^{-7} cm^2/sec$. For PANC02 tumors we assume that it is in the range $(0.5-5)\cdot 10^{-8} cm^2/sec$. These values agree both with the experimental results and with the information regrading the values of the diffusion coefficients of macromolecules in different histologies.

Taking $\alpha_{Pb} = \lambda_{Pb}$ and $\alpha_{Pb} = 2.5\lambda_{Pb}$ as a representative case for SQ2 and PANC02 tumors respectively we get an effective diffusion length that lies between 0.5-1 mm in SQ2 tumors and 0.1- 0.3 mm in PANC02 tumors. For LL2 tumors we take the lower limit of the effective diffusion coefficient in SQ2 tumors and the upper limit of it in PANC02 tumors. We also choose $\alpha_{Pb} = \lambda_{Pb}$ as a representative value. The obtained effective diffusion length in LL2 tumors lies between 0.3-0.6 mm.

The validity of the ^{212}Pb number density approximations in different tumor types

The validity of the suggested 'Pb-only' and 'Rn-only' approximations for ^{212}Pb number density in different tumor types, can be examined by substituting the proposed values of ^{212}Pb and ^{220}Rn diffusion coefficients into the analytic asymptotic solution and into its approximations and comparing the results. Since ^{212}Pb and ^{220}Rn diffusion coefficient ranges vary between different histologies, each of the approximations should be examined in the proper domain. For comparison needs, we only regard the expected effective lengths in SQ2 and PANC02 tumors since they represent two extreme cases.

Figure 5.3(a) shows the ratio between the 'Pb only' approximation solution and the exact asymptotic solution as a function of the distance from a point source divided by the ^{212}Pb effective diffusion length. This ratio was calculated for a source with initial ^{224}Ra activity of $3\mu Ci$, ^{220}Rn desorption probability of $\frac{1}{3}$ and ^{212}Pb effective desorption probability of 0.55[2]. The ^{220}Rn effective diffusion length (L_{Rn}) was chosen to be 0.3 mm and the ^{212}Pb effective diffusion length was varied between $\frac{L_{Rn}}{0.3} - \frac{L_{Rn}}{0.7}$ (1-0.4 mm). These values represent the expected diffusion lengths in SQ2 tumors. As shown in the figure, the '^{212}Pb only' approximation holds reasonably well for the ratios $L_{Rn}/L_{Pb} < 0.5$, i.e L_{Pb} higher than 0.6 mm. For these values, within a few effective diffusion lengths from the source the difference between the solutions is smaller than 15%.

The ratio between the 'Rn only' approximation and the exact asymptotic solution is shown in figure 5.3(b). The ratio was calculated by using the same source characteristics. The ^{220}Rn effective diffusion length was chosen to be 0.2 mm and the ^{212}Pb effective diffusion length was varied between $L_{Rn}\cdot 0.1 - L_{Rn}\cdot 0.5$ (0.02-0.1 mm). These values are lower than the expected values of the ^{212}Pb effective diffusion length, even in PANC02

[2]This is the average value measured in all experiments

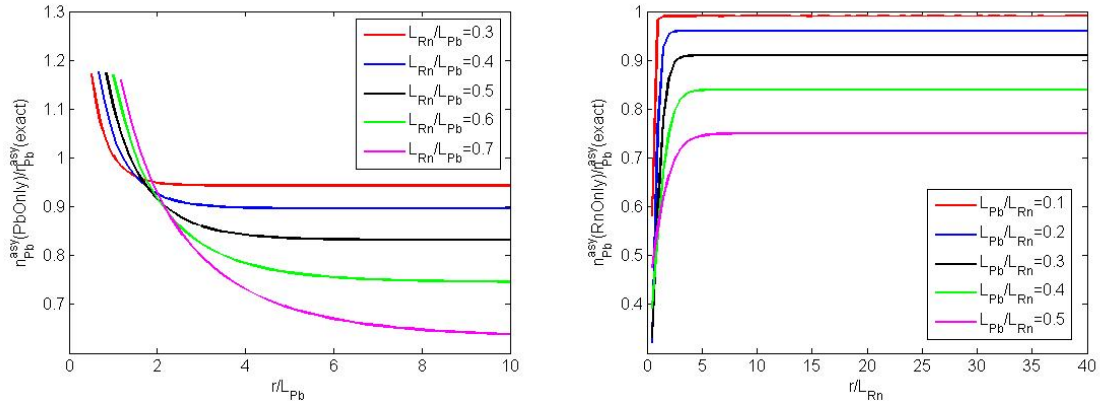

(a) (b)

Figure 5.3: The ratio between approximations of ^{212}Pb asymptotic solution and it's exact form as function of distance from the source divided by the proper diffusion length. (a) ratio between 'Pb only' approximation and the exact solution for $L_{Rn}/L_{Pb} = 0.3 - 0.7$ mm and $L_{Rn} = 0.3$ mm (b) ratio between 'Rn only' approximation and the exact solution for $L_{Pb}/L_{Rn} = 0.1 - 0.5$ mm and $L_{Rn} = 0.2$ mm

tumors (0.1 mm was the lowest ^{212}Pb diffusion length estimated in PANC02 tumors). These values were chosen in order to show that these approximations do not necessarily hold for the expected values of ^{212}Pb and ^{220}Rn diffusion lengths in all tumor types. The error obtained for the lowest ratio possible - $L_{Pb}/L_{Rn} = 0.5$ is already too high (25%) and it becomes even higher for higher diffusion lengths ratios.

5.2.4 ^{212}Bi distribution in the tumor

Time dependent and asymptotic solutions

The time-dependent diffusion-leakage equation for ^{212}Bi in spherical coordinates is:

$$\frac{\partial n_{Bi}}{\partial t} = \frac{D_{Bi}}{r^2}\frac{\partial}{\partial r}(r^2\frac{\partial n_{Bi}}{\partial r}) + s_{Bi} - (\lambda_{Bi} + \alpha_{Bi})n_{Bi} \tag{5.17}$$

^{212}Bi is formed inside the tumor by ^{212}Pb decays:

$$s_{Bi} = \lambda_{Pb} n_{Pb} \tag{5.18}$$

therefore the boundary condition is:

$$\lim_{r\to 0} 4\pi r^2 j_{Bi}^{asy}(r,t) = 0 \tag{5.19}$$

and the initial condition is: $n_{Bi}(0) = 0$.

As for ^{212}Pb**, the exact solution** of this equation is calculated numerically. This

solution is discussed later in the context of dose calculations.

The asymptotic solution is calculated by substituting the asymptotic form of the ^{212}Bi number density

$$n_{Bi}(\mathbf{r},t) = \hat{n_{Bi}(\mathbf{r})}e^{-\lambda_{Ra}t} \tag{5.20}$$

into equation 5.17. The result is :

$$n_{Bi}^{asy}(r,t) = (A_{Bi}\frac{e^{-r/L_{Rn}}}{r} + B_{Bi}\frac{e^{-r/L_{Pb}}}{r} + C_{Bi}\frac{e^{-r/L_{Bi}}}{r})e^{-\lambda_{Ra}t} \tag{5.21}$$

$$A_{Bi} = \left(\frac{L_{Rn}^2 L_{Bi}^2}{L_{Rn}^2 - L_{Bi}^2}\right)\frac{\lambda_{Pb}}{D_{Bi}}A_{Pb} \tag{5.22}$$

$$B_{Pb} = \left(\frac{L_{Pb}^2 L_{Bi}^2}{L_{Pb}^2 - L_{Bi}^2}\right)\frac{\lambda_{Pb}}{D_{Bi}}B_{Pb} \tag{5.23}$$

$$C_{Bi} = -(A_{Bi} + B_{Bi}) \tag{5.24}$$

$$L_{Bi} = \sqrt{\frac{D_{Bi}}{\lambda_{Bi} + \alpha_{Bi} - \lambda_{Ra}}}$$

where L_{Bi} -is *the effective ^{212}Bi diffusion length.*

^{212}Bi effective diffusion coefficient range

A series of experiments that were conducted in our laboratory in the past showed that ^{212}Bi and ^{212}Pb in SQ2 tumors treated with a single DART source are very close to secular equilibrium[14]. In this research, we use this assumption as justification for the determination of ^{212}Bi removal rate and its effective diffusion length. As can be derived from equation 3.25, secular equilibrium between ^{212}Bi and ^{212}Pb implies that $\alpha_{Bi} \ll \lambda_{Bi}$. The meaning is that decay inside the tumor is the main reason for ^{212}Bi atoms disappearance. For simplicity, we assume that $\alpha_{Bi} = 0$ in our following calculations and results analysis.

The secular equilibrium assumption is also related to the possible range of the ratio between the effective diffusion coefficients of the two isotopes. Using the asymptotic solutions for ^{212}Bi and ^{212}Pb activities (equations 5.21 and 5.12) we can calculate the activities ratio as a function of the radial distance from a point source, for varying values of L_{Bi}/L_{Pb} ($\alpha_{Bi} = 0$). Figure 5.4 shows, that in order to reach an activity ratio of 1.01 the diffusion lengths ratio must be smaller than 0.2. Assuming that α_{Pb} is of the order of magnitude of λ_{Pb} ($\alpha_{Pb} \approx \lambda_{Pb}$) leads to the conclusion that D_{Bi} is in the range $0.1D_{Pb} - 0.5D_{Pb}$.

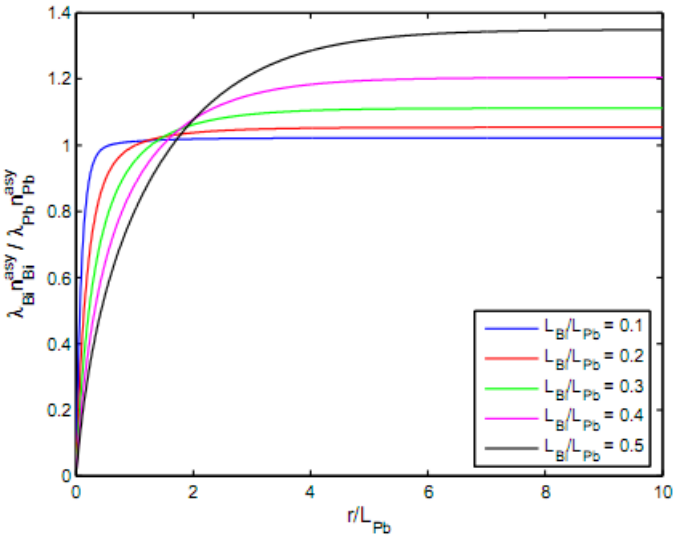

Figure 5.4: The local asymptotic ^{212}Bi\$^{212}$Pb activity ratio as a function of the radial distance from a point source, for varying values of L_{Bi}/L_{Pb}. The calculation assumed that $\alpha_{Bi} = 0$ and $\alpha_{Pb} = \lambda_{Pb}$. This figure was taken with permission from [14]

^{212}Bi\$^{212}$Po Alpha particle dose The alpha particle dose contributed by ^{212}Bi and ^{212}Po from source insertion to time t is given by:

$$Dose_{\alpha}(BiPo;\mathbf{r},t) = \frac{E_{\alpha}(BiPo)}{\rho}\int_{0}^{t}\lambda_{Bi}n_{Bi}(r,t^{'})dt^{'} \tag{5.25}$$

where $E_{\alpha}(BiPo)$ is the average alpha particle energy emitted by ^{212}Bi and ^{212}Po $E_{\alpha}(BiPo) = 7.80MeV = 1.25\cdot 10^{-12}J$. The asymptotic dose contributed by these two isotopes can be calculated by taking the integral limit $t \to \infty$.

The exact solution of the ^{212}Bi\$^{212}$Po alpha particle asymptotic dose has to be calculated numerically because of the delayed buildup of ^{212}Bi and ^{212}Pb at varying distanced from the source. It is presented for different parameter values in figure 5.5. The asymptotic dose as a function of the distance from a point source was calculated for a source with initial ^{224}Ra activity of $1\mu Ci$, ^{220}Rn desorption probability of 0.3 and effective ^{212}Pb desorption probability of 0.55. Also, for the reasons discussed above, we set $\alpha_{Bi} = 0$ and $D_{Bi} = 0.1D_{Pb}$. The two additional parameters, L_{Rn} and L_{Pb} were determined to be in two possible ranges - 0.2, 0.1-0.3 mm (for L_{Rn} and L_{Pb} respectively) representing PANC02 tumors and 0.35,0.55-1 mm representing SQ2 tumors. For the first range we choose $\alpha_{Pb} = 2.3\lambda_{Pb}$ and for the second $\alpha_{Pb} = \lambda_{Pb}$. As shown in the figure, the dose profile is sensitive to both L_{Pb} and L_{Rn} values but the influence of changing L_{Pb} seems to be higher. While for the lower L_{Pb} values the maximum distance for which the asymptotic dose exceeds 10 Gy is between 1.2-1.8 mm,

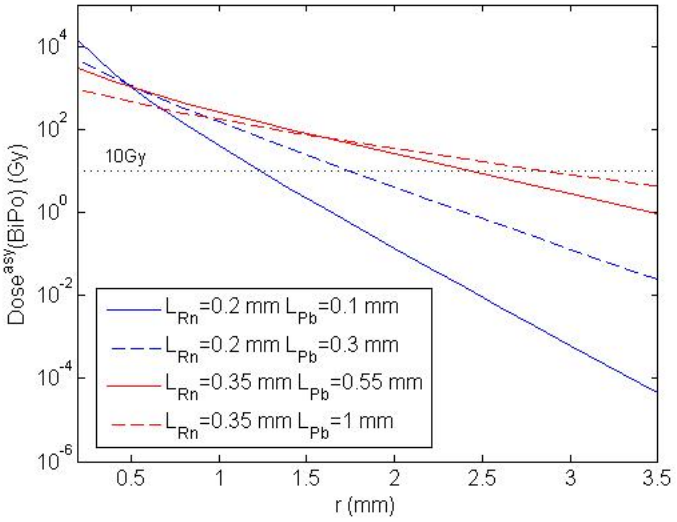

Figure 5.5: The asymptotic ^{212}Bi/^{212}Po alpha particle dose as function of the distance from a point source with initial ^{220}Rn release rate of $1\mu Ci$, and effective ^{212}Pb desorption probability of 0.55. $\alpha_{Bi} = 0$ and $D_{Bi} = 0.1D_{Pb}$. L_{Rn} and L_{Pb} set to four different values combinations representing SCC and pancreatic tumor.

for the higher L_{Pb} values it is between 2.4-2.8 mm.

Figure 5.6 shows the effective diameter corresponding to an asymptotic ^{212}Bi\$^{212}$Po dose exceeding 10 and 30 Gy as a function of the initial ^{220}Rn release rate. These diameters were calculated using the same source parameters described above. L_{Rn} and L_{Pb} were varied between maximum and minimum values in two ranges: $0.1 < L_{Rn} < 0.3$, $0.1 < L_{Pb} < 0.3$ and $0.3 < L_{Rn} < 0.4$, $0.5 < L_{Pb} < 1$. For the first range we choose $\alpha_{Pb} = 2.3\lambda_{Pb}$ and for the second $\alpha_{Pb} = \lambda_{Pb}$. As shown in the figure, the effective diameter values are much higher in the second range, ranging between 5-7 mm in comparison to 2-4 mm in the first. As explained above, the first range represents the expected range of values in SQ2 tumors and the second the expected range in PANC02 tumors.

Approximation to the calculation of the ^{212}Bi\$^{212}$Po Alpha particle dose

We apply different approximations to the asymptotic ^{212}Bi\$^{212}$Po dose by assuming that the local ^{212}Bi activity throughout the tumor can be factorized into a pure space-dependent part and a pure time-dependent part. The time dependent part is represented by the integral temporal behavior of ^{212}Pb atoms inside the tumor (equation 3.13) assuming ^{212}Bi and ^{212}Pb are in local secular equilibrium. The space dependent part is either approximated by using plausible assumptions about the ^{212}Pb effective diffusion length or represented by the complete analytic asymptotic solution for ^{212}Bi. The two possible approximations are therefore:

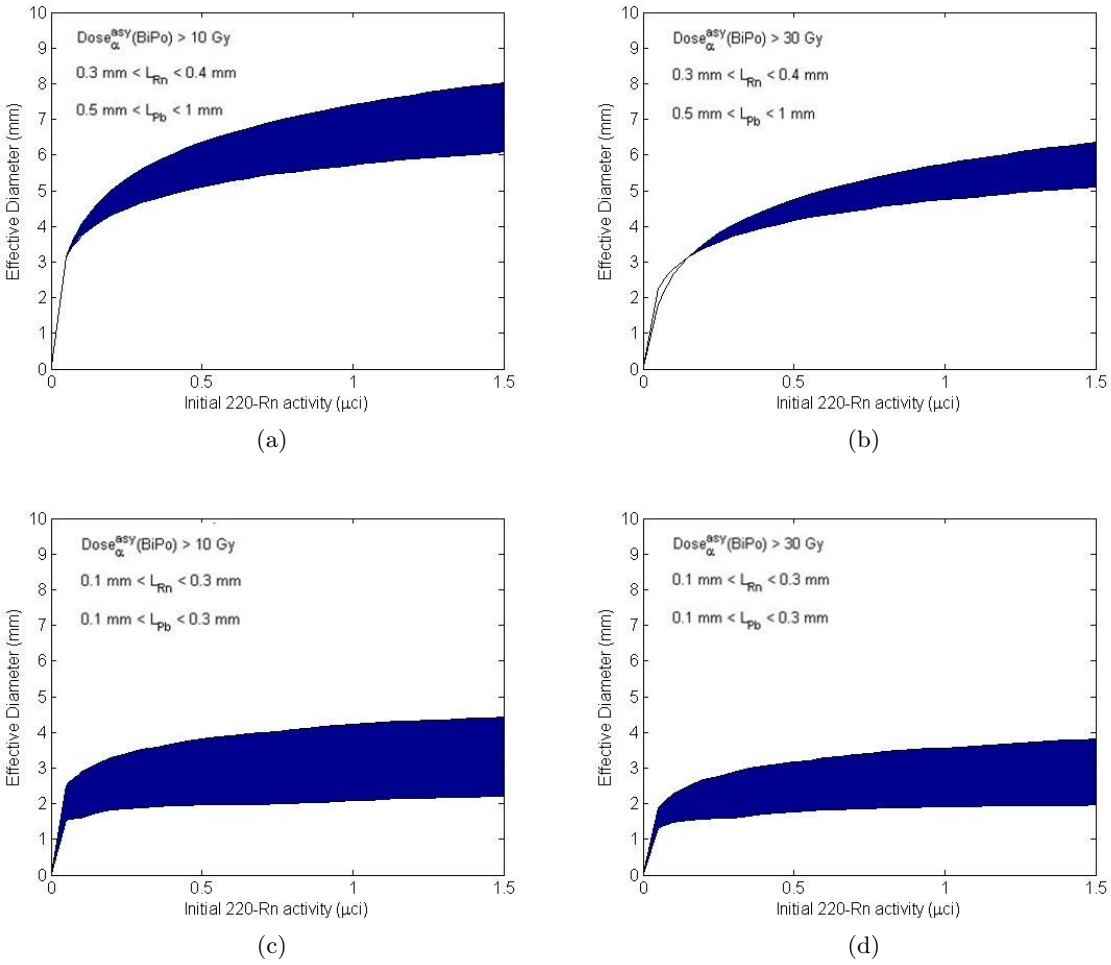

Figure 5.6: Effective Diameter of spherical region receiving an asymptotic ^{212}Bi\$^{212}$Po alpha dose larger than 10,30 Gy. L_{Rn} and L_{Pb} were changed between max and min values in two ranges: first, $0.1 < L_{Rn} < 0.3$ and $0.1 < L_{Pb} < 0.3$ and second $0.3 < L_{Rn} < 0.4$ and $0.5 < L_{Pb} < 1$. For the first range $\alpha_{Pb} = 2.3\lambda_{Pb}$ and for the second $\alpha_{Pb} = \lambda_{Pb}$.

- **'Pb only'** -In this approximation we assume that all ^{212}Pb atoms enter the tumor at $r \to 0$. We also assume that ^{212}Bi is in secular equilibrium with ^{212}Pb. Therefore the number density of ^{212}Pb is given by:

$$n_{Pb}^{PbOA}(r,t) = \frac{P_{des}^{eff}(Pb)\Gamma_{Ra}^{src}(0)e^{-\lambda_{Ra}t}}{4\pi D_{Pb}} \frac{e^{-r/L_{Pb}}}{r}(e^{-\lambda_{Ra}t} - e^{-(\lambda_{Pb}+\alpha_{Pb})t})$$

and the ^{212}Bi activity is given by:

$$\lambda_{Bi} n_{Bi}^{PbOA}(r,t) \approx \lambda_{Pb} n_{Pb}^{PbOA}(r,t)$$

Insertion of ^{212}Bi activity into equation 5.25 and taking $t \to \infty$ gives an analytic approximation for the asymptotic dose:

$$Dose_{\alpha}^{PbOA-asy}(BiPo;r) \approx \frac{E_{\alpha}(BiPo)}{\rho} \frac{\lambda_{Pb} P_{des}^{eff}(Pb)\Gamma_{Ra}^{src}(0)}{4\pi D_{Pb}} \frac{e^{-r/L_{Pb}}}{r}(\tau_{Ra} - \tau_{Pb}^{eff})$$

- **'RnPbBi' -** No approximation regarding the spatial distribution is made. The space dependent part is taken as the asymptotic ^{212}Bi function. Using equation 5.21, the local activity (for a point source) is given by:

$$\lambda_{Bi} n_{Bi}^{RnPbBi}(r,t) = \lambda_{Bi}(A_{Bi}\frac{e^{-r/L_{Rn}}}{r} + B_{Bi}\frac{e^{-r/L_{Pb}}}{r} + C_{Bi}\frac{e^{-r/L_{Bi}}}{r})(e^{-\lambda_{Ra}t} - e^{-(\lambda_{Pb}+\alpha_{Pb})t})$$

and the asymptotic dose becomes:

$$Dose_{\alpha}^{RnPbBi-asy}(BiPo;r) = \frac{E_{\alpha}(BiPo)}{\rho}\lambda_{Bi}(A_{Bi}\frac{e^{-r/L_{Rn}}}{r} + B_{Bi}\frac{e^{-r/L_{Pb}}}{r} + C_{Bi}\frac{e^{-r/L_{Bi}}}{r})(\tau_{Ra} - \tau_{Pb}^{eff})$$

The 'Pb only' approximation for the asymptotic dose underestimates the real dose since it neglects the contribution of ^{212}Pb activity inside the tumor that results from ^{220}Rn diffusion. As explained in paragraph 5.2.3 this approximation is valid when $L_{Rn}/L_{Pb} < 0.5$. The 'RnPbBi' solution overestimates the real dose because it disregards the delayed buildup of ^{212}Pb far from the source. This solution is valid for all possible effective length values. Figure 5.7 shows the exact and the 'RnPbBi' approximations for the ^{212}Bi\$^{212}$Po asymptotic dose calculated for a point source with initial ^{224}Ra activity of $1\mu Ci$, ^{220}Rn desorption probability of 0.3, effective ^{212}Pb desorption probability of 0.55, $\alpha_{Bi} = 0$ and $D_{Bi} = 0.1D_{Pb}$. For the diffusion lengths we set either ($L_{Rn} = 0.2$ mm, $L_{Pb} = 0.3$ mm) or ($L_{Rn} = 0.4$ mm $L_{Pb} = 1$ mm). As shown in the figure the difference between the exact and approximated asymptotic solution is negligible. The same figure shows the 'PbOnly' approximation for $L_{Rn} = 0.4$ and $L_{Pb} = 1$. Again, the difference between the solutions is negligible.

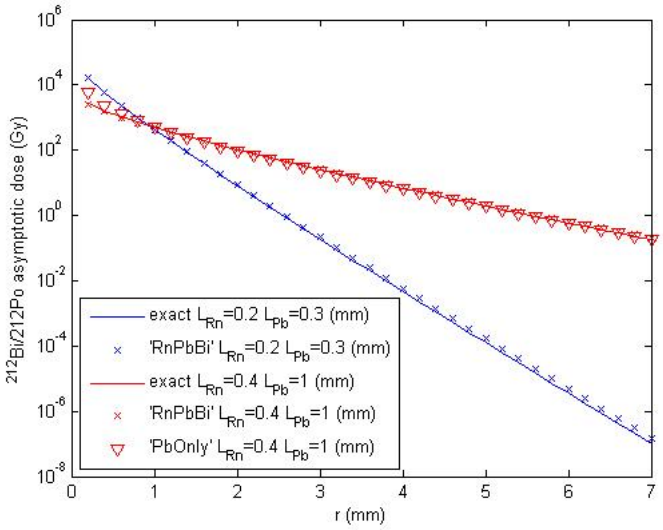

Figure 5.7: Exact and approximated solution of ^{212}Bi\$^{212}$Po asymptotic dose as function of the distance from a point source. The diffusion length are noted in the legend .

In the following sections we use these approximations in order to analyze the asymptotic ^{212}Bi\$^{212}$Po dose measured in SQ2, Panc02 and LL2 tumors. More details regarding the validity of these approximations can be found in [14].

5.3 The Diffusion-Leakage-Convection model

The diffusion-leakage model does not include explicitly convective processes. In this chapter we address this assumption and show its validity for the different radioactive isotopes moving in the tumor tissue. We also discuss the possible change in the asymptotic dose distribution as a result of a large convective effect on the radioactive atoms.

5.3.1 Convection of DART diffusing atoms inside the tumor

The first mechanism that determines the convective component of molecular transport in the tumor is the interstitial fluid flow. In normal tissues, interstitial fluid movement occurs from the capillary to lymphatics driven by interstitial fluid pressure gradients. However, according to different studies, most tumors do not have anatomically well-defined lymphatic vessels and this leads to an increase in the interstitial fluid pressure and a consequent reduction of the driving force for fluid flow [28, 27, 26]. A study aiming to measure the magnitude of the interstitial fluid flow in tissues showed that the average fluid velocity is about 0.6 $\mu m/s$ [22]. The researchers did not find a significant difference between the fluid velocity in tumors and in normal tissue. They explained that it might result from the use of

a tumor in an initial development stage when pressure gradients have not been developed. Still, this value might serve as an upper limit for the interstitial fluid velocity in order to estimate its importance in the radioactive isotope transport inside the tumor.

As mentioned in section 5.1 the volume of the interstitial space in tumors is generally very large in comparison to normal tissues. According to various studies, this volume can comprise up to 60% of the tumor volume [11].

The second important mechanism that affects the convective transport is the blood flow in the tumor. The movement of molecules through the tumor vasculature is governed by the vascular morphology (i.e the number, length, diameter and geometric arrangement of various blood vessels) and the blood flow rate. As explained in section 5.1 the blood system in tumors is very complex and different from the blood system in normal tissues. Still, numerical values for a few characterizing parameters can be found in the literature.

Quantitative morphometric studies in tumors showed that vascular volume fraction out of the whole tumor volume ranges between 1-30% in different tumors. In most of the tumors compared in this study the vascular volume fraction was smaller than 10%. Generally, this value changes as a function of tumor growth rate that depends on the tumor type. Some studies show that the fractional vascular volume of tumors remains fairly constant during growth, while others show that the fractional vascular volume decreases as a tumor grows [12]. Newer research, designed to measure the vascular volume fraction in different tumor types by using magnetic resonance imaging showed that it ranges between 2-7% of the tumor volume and also showed that it varies significantly between different tumor types [4].

A work comparing blood vessels in normal tissues and in human glioma (U87) showed that the blood velocity in tumors does not depend on the vessel diameter in contrast to normal tissues where the velocity decreases with decreasing vessel diameter. Also, the blood velocity in tumor vessels is about an order of magnitude lower than in the host vessels - ranging between 0-0.5 mm/s. Another study showed that blood flow rate varies in different tumor areas. In necrotic and semi-necrotic regions of the tumor the blood flow rates are low. In non-necrotic regions the flow rates are variable and can be substantially higher than in the surrounding normal tissues [13].

We use the values presented above as a reference in order to estimate the importance of the convective processes in the radioactive isotope transport in the tumor. Specifically, the possible drift of ^{220}Rn, ^{212}Pb and ^{212}Bi inside the tumor as a result of the convective processes is discussed in the following sections. As explained above, the half-lives of the other daughters in ^{224}Ra decay chain are very short and therefore we do not treat them explicitly in this context.

5.3.2 ^{220}Rn convection in the tumor

^{220}Rn atoms inside the tumor do not interact with other molecules since ^{220}Rn is a noble gas. This characteristic, together with its short half life, makes it reasonable to assume that ^{220}Rn does not leave the tumor with the blood but moves inside it entering and leaving the blood vessels through their porous walls.

In order to estimate the possible effect of the blood and fluid flow inside the tumor on ^{220}Rn transport, we add to the diffusion-leakage equation (equation 5.2) a third 'drift part' yielding the equation:

$$\frac{\partial n_{Rn}}{\partial t} = D_{Rn}\nabla^2 n_{Rn} + s_{Rn} - \lambda_{Rn} n_{Rn} + f_b \bar{v_b} \cdot \nabla n_{Rn} + f_f \bar{v_f} \cdot \nabla n_{Rn} \tag{5.26}$$

f_b is the fraction of blood volume inside the tumor and $\bar{v_b}$ is a constant average blood flow rate in direction $\hat{r}$. Similarly, f_f is the fraction of the interstitial fluid inside the tumor and $\bar{v_f}$ is an average fluid velocity. Multiplying the average velocity of either the blood or the interstitial fluid by the proper volume fraction represents an effective volume inside the tumor in which the velocity is constant and equal to the proposed value. This simplification is very coarse and will probably result in overestimation of the drift effect. Moreover, we cannot exclude the possibility that the blood and the interstitial fluid flow in opposite directions so that the real effective velocity is smaller. Despite of these possible problems, the asymptotic solution for the presented equation gives an upper limit for the drift of ^{220}Rn atoms inside the tumor. This upper limit can teach us about the order of magnitude of this effect.

In order to estimate this effect we define a new variable - the 'Drift Length' which is the average distance to which ^{220}Rn atom is drifted by the blood flow or by the interstitial fluid flow. The drift length caused by the blood flow is given by $L_{Rn}^{Bdrift} = f_b \bar{v_b} \tau_{Rn}$ and the drift length caused by the fluid flow is given by $L_{Rn}^{Fdrift} = f_f \bar{v_f} \tau_{Rn}$. Insertion of the asymptotic form for ^{220}Rn behavior into equation 5.3 and replacement of the parameters with the given drift lengths and with ^{220}Rn effective diffusion length (equation 5.16) gives:

$$\frac{1}{L_{Rn}^2} n_{Rn} - S_{Rn} \approx \nabla^2 n_{Rn} + \frac{L_{Rn}^{Fdrift}}{L_{Rn}^2} \cdot \nabla n_{Rn} + \frac{L_{Rn}^{Bdrift}}{L_{Rn}^2} \cdot \nabla n_{Rn} \tag{5.27}$$

In order to estimate the drift effect we should examine the reasonable values for L_{Rn}^{Bdrift} and L_{Rn}^{Fdrift} in comparison to the expected ^{220}Rn effective diffusion length proposed in section 5.2. Taking 0.6 $\mu m/s$ as the fluid velocity inside the tumor and 0.4 as the interstitial volume fraction gives the fluid drift length:

$$L_{Rn}^{Fdrift} = 0.0006 \cdot 0.4 \cdot 80.2 = 0.02mm$$

Taking 0.1 mm/s as the blood velocity inside the tumor and 0.05 as the blood volume fraction gives the blood drift length:

$$L_{Rn}^{Bdrift} = 0.1 \cdot 0.05 \cdot 80.2 = 0.4mm$$

These results impliy that the drift of ^{220}Rn atoms inside the tumor as a result of the blood flow might be non negligible in comparison to the diffusion length. On the contrary, the drift as a result of the interstitial fluid flow seems negligible.

The exact effect of each mechanism can be examined separately by solving equation 5.27 numerically for several diffusion length values. Figure 5.8(a) and (b) shows the asymptotic dose contributed by the alpha decays of ^{220}Rn and ^{216}Po atoms emitted from a point source with an initial ^{220}Rn release rate of $1\mu Ci$. The dose was calculated by solving the convection-diffusion equation with drift length values $L_{Rn}^{Fdrift} = 0.02$ mm and $L_{Rn}^{Bdrift} = 0$. In (a) the ^{220}Rn diffusion length was 0.2 mm and in (b) it was 0.3 mm. For each parameter set the left figure presents the asymptotic dose in the z-r plan (cylindrical coordinates) where the velocity direction was along the z axis. The right figure presents statistical properties of the asymptotic dose as a function of the distance from the source location. The graphs 'Z>0' and 'Z<0' represent the exact dose on the z axis to the right and to the left of the source (with, and opposite to the flow direction). The graphs 'mean' and 'median' represent the mean and the median values of the dose calculated for varyious distances from the source (r) and '68% c.i.' represents the corresponding 68% confidence interval of the dose. All four graphs demonstrate that the drift of ^{220}Rn atoms as a result of the interstitial fluid flow inside the tumor is negligible. It is very well demonstrated by the similarity observed between the graphs 'Z>0' ,'Z<0' , 'mean' and 'median' implying that the dose distribution around the source is isotropic.

Figure 5.9 presents the results of a similar calculation that was conducted in order to examine the blood flow effect. The drift lengths were set to be $L_{Rn}^{Bdrift} = 0.4$ and $L_{Rn}^{Fdrift} = 0$. The ^{220}Rn diffusion length was varied between 0.2 and 0.3. The resultant four graphs shows an anisotropic dose distribution, implying that the blood flow inside the tumor might have a non negligible effect on ^{220}Rn transport inside the tissue.

Despite this result it is important to remember that the suggested drift length value representing the blood flow might be much higher than the real value. It is very reasonable to assume that the real effective velocity is much lower since it is composed of many small currents that flow in different directions. Therefore, we cannot exclude the possibility that in reality, the convection of ^{220}Rn atoms is neglegible in comparison to its diffusion inside the tumor.

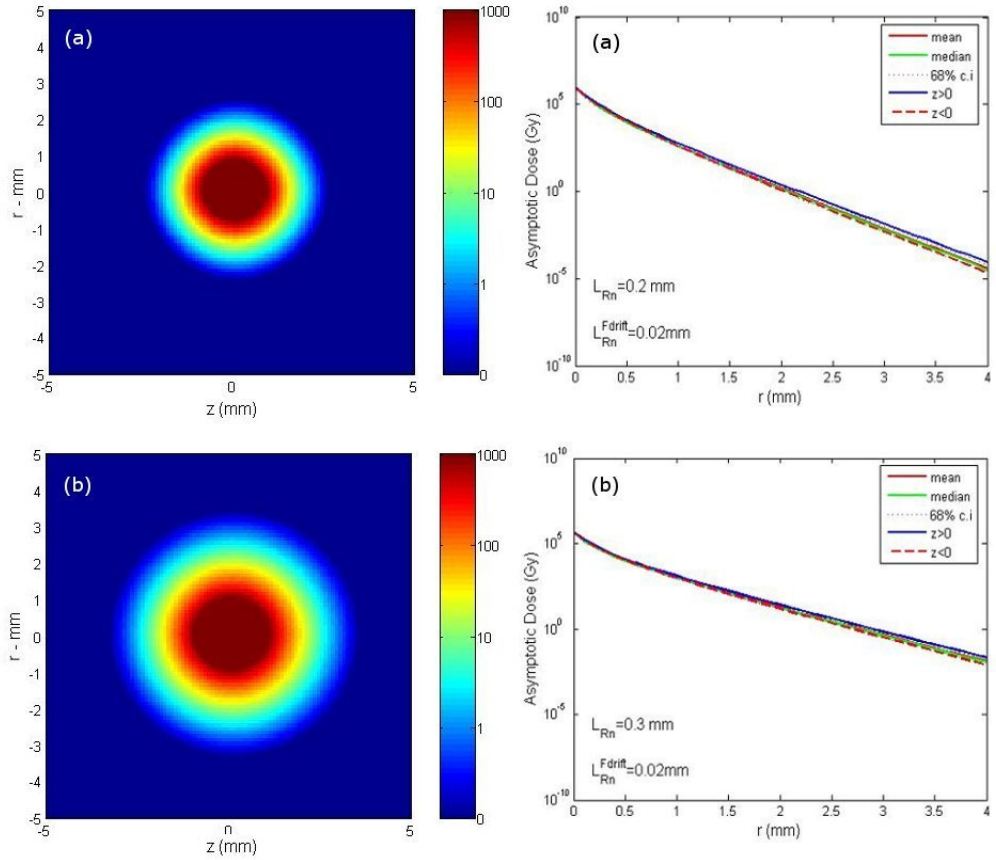

Figure 5.8: The asymptotic dose contributed by ^{220}Rn\$^{216}$Po alpha decays in R-Z plan and as a function of the distance from the source. The initial ^{220}Rn release rate was set to be $1\mu Ci$. ^{220}Rn diffusion length and the drift length as a result of the interstitial fluid flow are noted in each plot.

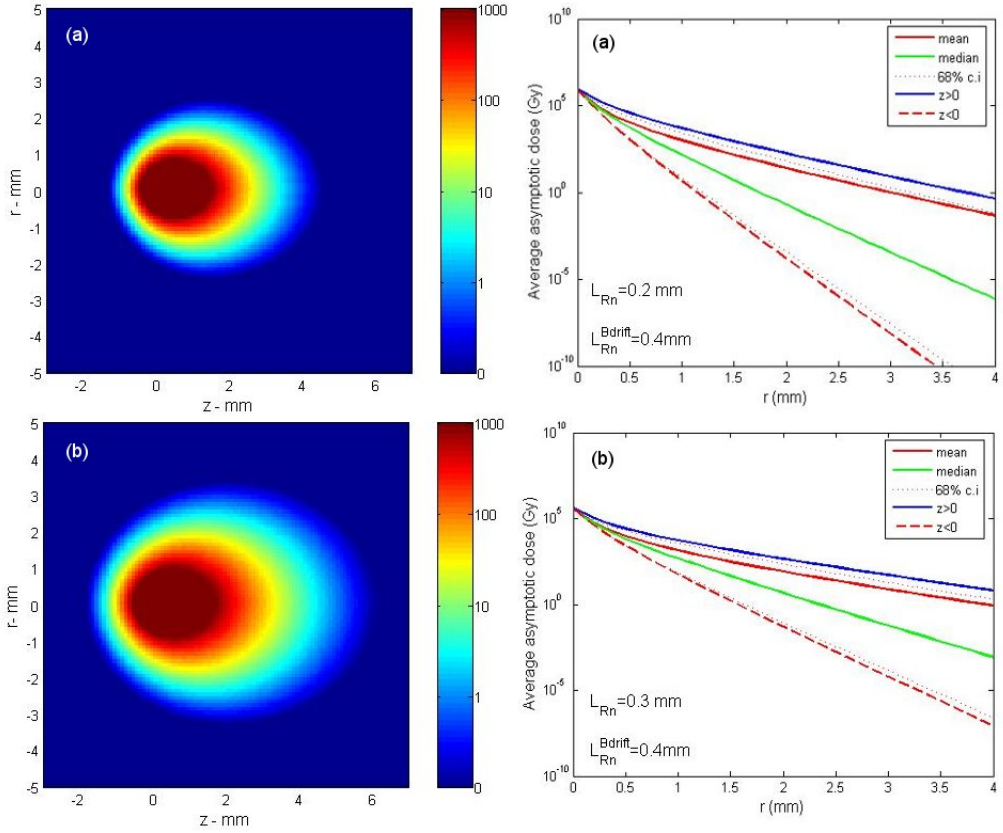

Figure 5.9: The asymptotic dose contributed by ^{220}Rn\$^{216}$Po alpha decays in R-Z plan and as a function of the distance from the source. The initial ^{220}Rn release rate was set to be $1\mu Ci$. ^{220}Rn diffusion length and the drift length as a result of the interstitial fluid flow are noted in each plot.

5.3.3 ^{212}Pb convection in tumor

In contrast to ^{220}Rn, we assume that a ^{212}Pb atom that enters a blood vessel inside the tumor is trapped in the red blood cells and is removed from the tumor with a characteristic constant rate. This rate is included in the ^{212}Pb effective half life that represents the duration of ^{212}Pb stay inside the tumor. Theoretically, it can be assumed that during their stay in the tumor ^{212}Pb atoms drift as a result of the interstitial fluid flow or as a result of the blood flow in small vessels that do not connect to a main vessel leaving the tumor. However, it is very difficult to assess the exact influence of each of these mechanisms on ^{212}Pb atom movement inside the tumor.

With regard to the blood flow, it is hard to tell what percentage of the blood vessels are involved in the ^{212}Pb drift inside the tumor and what is the blood velocity inside them. Therefore, even if a similar expression to that suggested for ^{220}Rn is used to describe ^{212}Pb drift length as a result of the blood flow inside the tumor, it is hard to estimate the expected numbers required for the calculation.

In order to estimate the ^{212}Pb drift as a result of the interstitial fluid flow, the expression given above for the drift length of ^{220}Rn can be used. However, insertion of the same values used for ^{220}Rn drift length calculation (0.6 $\mu m/s$ as the fluid velocity inside the tumor and 0.4 as the interstitial volume fraction) and ^{212}Pb effective half-life, gives a very long drift length of 8.8mm. This drift length equals 8 times the highest ^{212}Pb effective diffusion length ever measured in tumors, and is probably unrealistic since it results in a very anisotropic dose distribution that was never observed in real measurements.

Due to these reasons, we use a different approach in order to estimate the drift of ^{220}Pb in the treated tumors. Writing the diffusion-leakage-convection equation for ^{212}Pb atoms in the tumor gives:

$$0 \approx \nabla^2 n_{Pb} + \frac{L_{Pb}^{Fdrift}}{L_{Pb}^2} \cdot \nabla n_{Rn} + \frac{L_{Pb}^{Bdrift}}{L_{Pb}^2} \cdot \nabla n_{Rn} - \frac{1}{L_{Pb}^2} n_{Pb} + S_{Pb} \tag{5.28}$$

This equation implies that an estimate of the real possible values for the ratio between the drift length and the diffusion length would yield the ^{220}Pb drift length. Therefore, for simplicity, we define a new effective ^{212}Pb drift length to be the sum of both drift lengths: $L_{Pb}^{Effdrift} = L_{Pb}^{Fdrift} + L_{Pb}^{Bdrift}$. Using this effective length we can examine the dose distribution for different values of the ratio $r_L = \frac{L_{Pb}^{Effdrift}}{L_{Pb}}$.

The change in the dose distribution as a function of r_L is examined as follows. First, for simplicity, we solve equation 5.28 numerically by assuming the 'Pb only' approximation and an effective ^{212}Pb diffusion length ranging between 0.55-1 mm. The values for r_L are set to range between 0-5, consistent with the results that follow. The dose contributed by the alpha decays of ^{212}Bi and ^{212}Po is calculated by using the numerical equation solution.

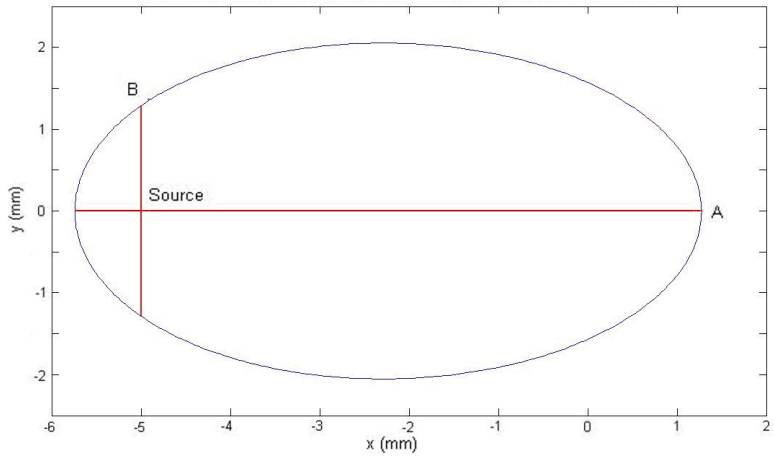

Figure 5.10: An ellipsoid representing an isodose curve of a calculated dose distribution. The long axis is labeled as A and the short axis as B. The ratio r=A/B is an estimator for the dose anisotropy

In order to describe the anisotropy of the calculated dose we define r as the ratio between the long and the short axis of the ellipsoid representing an isodose curve for a specific Gy level (see figure 5.10). r values can now be examined in relation to r_L and to the effective diffusion length.

Figure 5.11 presents the results of the described procedure. The right column shows three 3-dimensional graphs representing the relation between the effective diffusion length, r and r_L for a selected dose levels of 10,100 and 300 Gy. The left column graphs show the projection of the right column graphs on the r-r_L axis.

There are a few interesting phenomena observed in these graphs. First, the relation between r and r_L is well defined for small values of r_L (ranging between 0-2.5) and does not depend on the diffusion length. For higher values of r_L, r depends on the effective diffusion length value. Second, r and r_L are of the same order of magnitude. These results are obtained for all dose levels.

As will be shown below, the estimate of r values from the dose distribution maps measured in SQ2 tumors (characterized by a high ^{212}Pb diffusion length in comparison to the ^{220}Rn diffusion length) yields values ranging between 1-1.5. This implies that the effective diffusion length and the drift length in these tumors are of the same order of magnitude.

The dose distribution measured in PANC02 tumors, characterized a ^{212}Pb diffusion length and a ^{220}Rn diffusion length of the same order of magnitude, is relatively isotropic, and the estimated r values range between 1-1.5. This implies that the convection effect on ^{212}Pb atoms in PANC02 tumors is of the same order of magnitude as in SQ2 tumors, where the 'Pb only' approximation is valid.

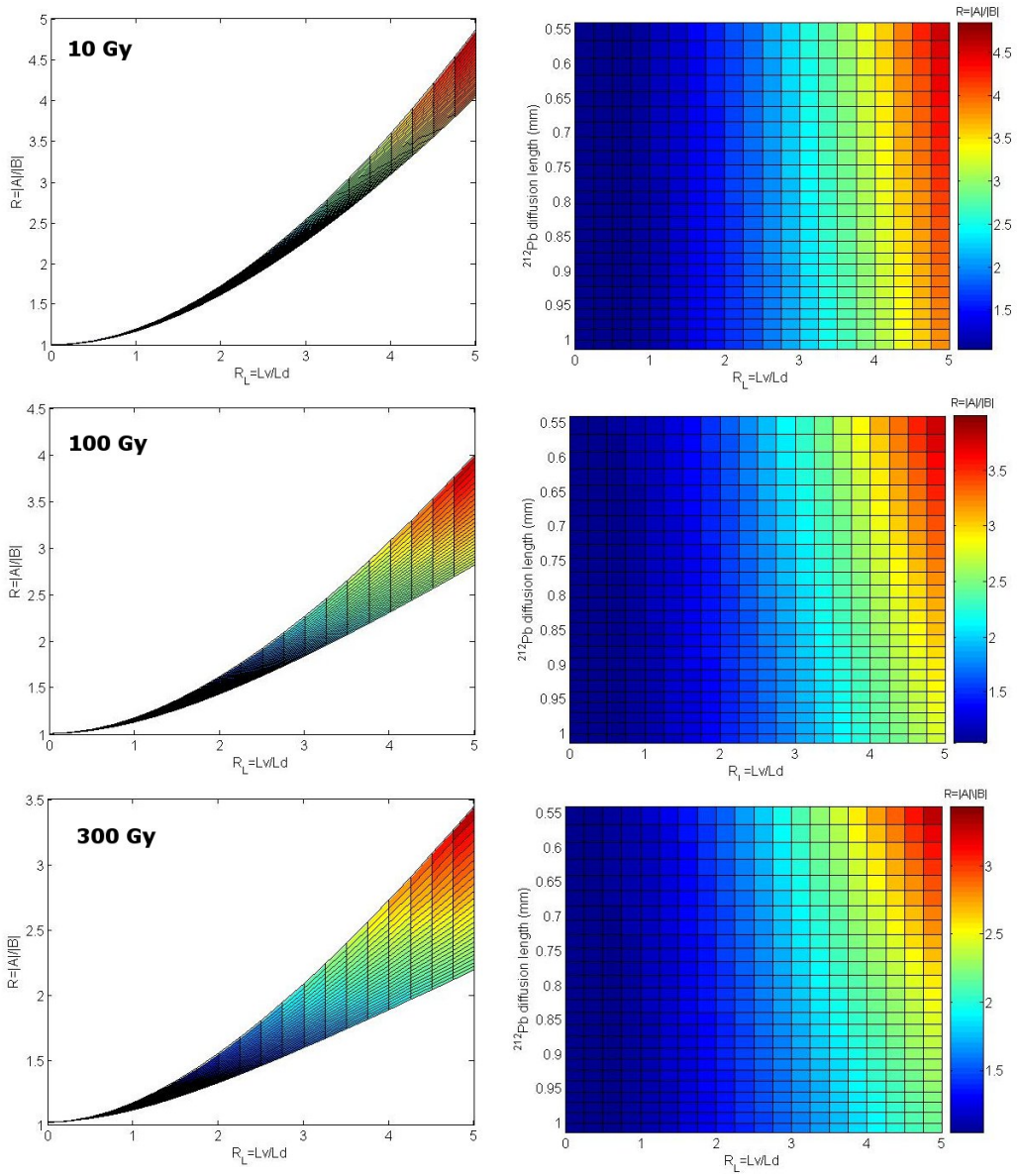

Figure 5.11: The relation between r_L, r and the effective diffusion length in isodose curves of 10,100 and 300 Gy.

5.3.4 ^{212}Bi convection in the tumor

As detailed in section 5.3 we assume that ^{212}Bi and ^{212}Pb in the tumor are in secular equilibrium. Therefore, the possibility of independent ^{212}Bi atoms drift inside the tumor as a result of the blood or interstitial fluid flows is neglected. We assume that ^{212}Bi atoms drift inside the tumor can only result from its parents (^{212}Pb atoms) drift.

5.4 Dose distribution measurements

In order to explore the spatial distribution of the diffusing isotopes inside real tumors several HRA experiments were conducted on SQ2, PANC02 and LL2 tumors. In this section we first describe the experimental procedure involved in these experiments. Then we explain the analysis steps used, based on the theoretical background described above. Finally we present the results obtained from the experiments and discuss their meaning.

5.4.1 Experimental procedure

HRA experiments included the following steps:

- *Source preparation* - sources were prepared according to the procedure described in section 2.3. The source ^{224}Ra activity ranged between 0.4-1.5 μCi, with ^{220}Rn desorption probabilities in the range 0.25-0.44.

- *Tumor cell inoculation and source insertion* - were conducted according to descriptions at sections 2.1 and 2.2. SQ2, PANC02 and LL2 cells were injected into the proper mice type. The entire experimental and analysis procedure was completed for 5 SQ2 tumors, 6 PANC02 tumors and 5 LL2 tumors.

- *Tumor treatment* - Tumors were treated with a single DART source inserted parallel to the tumor base when their average lateral diameter was typically in the range 8 - 10 mm. The treatment duration ranged between 3-4 days in all cases.

- *Tumor and source removal* - Four days after source insertion the tumors were removed. The tumors were placed in dry ice and carefully cut to expose the rear end of the source in order to enable its extraction. The extracted source was placed in a capped scintillation vial in 0.5 ml of deionized water for subsequent gamma measurements.

- *Tumor fixation* - The tumors were placed in 4% formaldehyde for fixation at 4^{o}C for 24-48 hours. The exact fixation time represented a tradeoff between higher ^{224}Pb activity for short times and better fixation for long fixation times. Usually, bigger tumors were fixated for 48 hours.

- *Histological section preparation* - After fixation the tumors were cut to 3-5 blocks, perpendicularly to the their base (i.e., perpendicularly to the source axis). The tumor blocks were processed and embedded in paraffin following standard procedures. Histological sections (5 or 10 μm thick) were cut using a Leica RM2055 microtome (Leica, Nussloch, Germany) and placed on glass slides. All blocks were cut to sections in a plane perpendicular to the source axis. In order to enable later identification of each section, small stickers marked with ^{212}Pb were placed on each glass slide after its preparation. The marked slide was scanned using an optical flatbed scanner (EPSON V750).

- *Activity record* - The slides were laid on the Fujifilm imaging plate (BAS-TR2040S, Fujilm, Japan) over a 12 mm Mylar foil to prevent direct contact with the plate. In the majority of cases, slides were measured twice, over the first night after its preparation (15 hours) and over the next night. The local ^{212}Pb activity of the slide was recorded by the Fuji plate. Following each measurement, the imaging plate was scanned by an image reader. Two machines were used during this research - BAS-2500 and FLA-9100. Some measurements were scanned with a pixel size of $100\mu m$ and others with a pixel size of $200\mu m$.

- *Histological section staining* - The histological sections used in the experiments were all stained at a later stage with Hematoxylin-Eosin (H&E) (Surgipath, Richmond, IL, USA) for tissue damage detection. Photographs of the stained sections were obtained by an optical flatbed scanner (EPSON V750).

5.4.2 Analysis Procedure

The analysis of the images obtained by the image reader at the end of the described procedure was composed of many steps. Some of the steps involved were discussed thoroughly in [14] and are only summarized here. Additional analysis procedures that were added are described to detail below. The analysis steps were performed by using the software developed as part of the preclinical work on DART treatment. Additional steps were performed by using a computer code written for the analysis purpose. Generally we divide the analysis procedure into 3 main logical steps that are described below.

Image restoration

In many imaging applications the imaging system introduces a slight distortion. Often images are slightly blurred due to the system internal properties and the record of each point source is spread over a few pixels instead of being recorded in one pixel only. In our case the blurring effect can be attributed to several mechanisms such as light scattering

inside the phosphor layer, a 'memory' effect in the electronics and a contribution from beta particles emitted by some of the radioactive isotopes to the neighboring pixels.

Image restoration is a general field that involves deblurring techniques. Different methods can be used for that purpose when the imaging system PSF (point spread function) is known. The PSF describes the image resulting when a point source is placed directly on the plate. In general, every image that is produced by the scanner (represented by $I(x, y)$) results from the convolution of the real image (the pattern of stored energy on the plate) $I_{real}(x, y)$ and the PSF.

Like in every other field the first basic analysis step in our image analysis is image deblurring. In order to do that the PSF of FLA-9100 was measured using a procedure described in [14]. In order to deblur the image that was obtained in the image reader we used the Lucy - Richardson algorithm supplied with MATLAB's image processing toolbox. This is an iterative method that maximizes the likelihood that the resulting image, when convoluted with the PSF, is consistent with the blurred image, assuming Poisson noise statistics. We analyzed each image by using 1,2 and 5 iterations in order to estimate the possible error range [14].

Translation of measurements to activity

As explained in section 2.7 the raw images obtained by the image reader contain data about the PSL intensity recorded on each pixel. In order to use this data it should be converted to the activity at the time of tumor removal and to the required dose pattern. We did this by the following steps:

- *Identification of the individual tumor sections on the image* - The marked stickers that were placed on the glass slides left strong and clearly identifiable marks on the fujifilm plate, allowing the geometric identification of their position. Registration between the images of the scanned slide and the fujifilm record was conducted by identification of the sticker locations in both images and a proper placement of one image on top of the other. The contour of each tumor section over the Fuji plate image was then marked by using the original slide scan.

- *Image calibration using calibration samples* - The conversion from PSL to ^{212}Pb activity required the use of ^{212}Pb calibration samples. Such samples were routinely prepared for the HRA experiments by recoil implantation of ^{212}Pb atoms inside a circular region (5.5 mm diameter) of a polyester film at a typical depth of a few nm. After implantation the sample activities were measured by the gamma counter. The calibration samples were then placed over a glass slide that was placed over the fujifilm plate together with the slides containing the histological sections. In order to avoid saturation the ^{212}Pb activity of the calibration samples (at the beginning of the

exposure) had to be limited to a typical range of 0.005 - 0.5 nCi. The samples were therefore prepared several days ahead of time, with an initial ^{212}Pb activity of several nCi, allowing for accurate measurement in the gamma detector.

In order to perform the image calibration a few calibration samples with different activities were placed over the fuji plate at each exposure. The PSL in the region of each calibration sample was calculated and fitted as a function of the sample measured activity by a straight line. The line slope was marked as C_{Pb} (units PSL/^{212}Pb decay). This coefficient represents the PSL resulting from a single decay of ^{212}Pb directly above the pixel. It was assumed that this coefficient is constant across the imaging plate.

- *Conversion of PSL to activity* - Assuming that there is no ^{224}Ra inside the tissue[3], the energy stored in each pixel is the result of the time dependent process involving ^{212}Pb decays above the pixel and the fadeout of the recorded signal[4]. The PSL value at the scan time that represents the activity in each pixel region is given by:

$$I(t_{scan}) = f_{Mylar}(d_M) f_{tissue}(d_T) C_{Pb} \int_{t_{start}}^{t_{end}} \Gamma_{Pb}(\mathrm{t}) f(t_{scan} - t) dt \tag{5.29}$$

where $\Gamma_{Pb}(t)$ is the time dependent ^{212}Pb activity , $f(t_{scan} - t)$ is the fadeout factor and C_{Pb} represents the PSL resulting from a single decay. $f_{Mylar}(d_M)$ and $f_{tissue}(d_T)$ are attenuation factors, representing the decrease in PSL resulting from the presence of the Mylar foil (with thickness d_M) and from the fact that the ^{212}Pb activity inside the tissue is distributed along various depths, which are non-negligible in comparison to the alpha particle range. The times in the integral limits (t_{start}, t_{end}) are the start and the end time of the exposure. As explained above, C_{Pb} is calculated in each experiment by using the calibration samples. $f(t_{scan} - t)$ was measured experimentally [14] and is given by:

$$f(t) = a_1 e^{-\alpha_1 t} + a_2 e^{-\alpha_2 t}$$

$$a_1 = 0.37 \pm 0.08, a_2 = 0.63 \pm 0.02, \alpha_1 = 2.7 \pm 0.9 h^{-1}, \alpha_2 = 0.02 \pm 0.03 h^{-1}$$

$f_{Mylar}(d_M)$ was also measured experimentally and is given by:

$$f_{Mylar}(d_M) = 0.982 e^{-d_M/18.9} + 0.018 e^{-d_M/1695}$$

$f_{tissue}(d_T)$ was calculated numerically by comparing the total transmitted energy for

[3] An explanation of a possible analysis when it is the case will be given below

[4] ^{220}Rn and ^{216}Po decays within a very short time after tumor removal and therefore are not found in the slide

the case of a point source placed on a Mylar surface with a case of a tissue with a given depth [14]. In each experiment, the initial ^{212}Pb activity above a given pixel at the start time of the exposure was calculated by substituting these expressions into equation 5.29 . The ^{212}Pb activity at tumor removal time was then calculated by straightforward back extrapolation of the activity at exposure start time: $\Gamma_{Pb}(t_{TR}) = \Gamma_{Pb}(t_{start})e^{\lambda_{Pb}(t_{start}-t_{TR})}$.

- *Estimation of $^{224}Ra/^{212}Pb$ ratio* - The possible presence of ^{224}Ra in the tissue poses two problems. First, it might change the spatial activity pattern due to the alpha decays of it and of its daughters, ^{220}Rn and ^{216}Po. Second, it changes the calculation for ^{212}Pb activity at tumor removal based on the ^{212}Pb activity at exposure start. Therefore, the contribution of ^{224}Ra activity inside the tumor was taken into account in the calculation of ^{212}Pb activity assuming that each ^{224}Ra decay results in C_{Ra} PSL in the same pixel and that the PSL is proportional to the incident alpha particle energy. The introduction of $f_{leak}(Rn)$ as the ^{220}Rn leakage factor (^{220}Rn can leak out of the tissue during the exposure - this factor range between 0-1) leads to the following ratio:

$$\frac{C_{Ra}}{C_{Pb}} = \frac{E_\alpha(Ra) + (1 - f_{leak}(Rn))(E_\alpha(Rn) + E_\alpha(^{216}Po))}{E_\alpha(BiPo)} \tag{5.30}$$

The PSL itself was related to the ^{212}Pb and the ^{224}Ra activities through:

$$I(t_{scan}) = f^{Pb}_{Mylar}(d_M) f^{Pb}_{tissue}(d_T) C_{Pb} \int_{t_{start}}^{t_{end}} \Gamma_{Pb}(\mathrm{t}) f(t_{scan} - t) dt \tag{5.31}$$

$$+ f^{Ra}_{Mylar}(d_M) f^{Ra}_{tissue}(d_T) C_{Ra} \int_{t_{start}}^{t_{end}} \Gamma_{Ra}(\mathrm{t}) f(t_{scan} - t) dt \tag{5.32}$$

The average^{224}Ra/^{212}Pb activity ratio for a given tumor section was calculated by summing the net PSL that was measured inside the section at the two exposures, and calculation of both isotopes activities at first exposure start by using equations 5.32, 5.30 and an equation describing these isotopes activities. Then both activities were propagated to the second exposure times assuming no ^{212}Pb buildup inside the section. The ^{212}Pb activity at tumor removal time was calculated from the activities calculated for the first exposure start by assuming a ^{212}Pb buildup during fixation time and no buildup between the section cut and the exposure start[5]. It was calculated for various values of the $f_{leak}(Rn)$ parameter.

[5]no buildup is assumed between tumor cut to exposure and between exposure since slides were held in an open air. it is assumed that ^{220}Rn escaped from the tissue

- *Conversion of ^{212}Pb activity to dose*- The calculation of alpha particle dose contributed by ^{212}Bi and ^{212}Po was done by the approximation suggested in section 5.2.1. We factorize the local activity into a pure time-dependent and a pure space dependent part. The dose from source insertion to tumor removal in the j-th voxal was calculated by:

$$Dose_{\alpha}(BiPo;j,t_{TR}) = \frac{E_{\alpha}(BiPo)}{m_j}\int_0^{t_{TR}}\Gamma^j_{Pb}(t^{'})dt^{'} =$$

$$\frac{E_{\alpha}(BiPo)}{m_j}\frac{\Gamma^j_{Pb}(t_{TR})}{e^{-\lambda_{Ra}t_{TR}}-e^{-(\lambda_{Pb}+\alpha_{Pb})t_{TR}}}(\tau_{Ra}(1-e^{\lambda_{Ra}t_{TR}})-\tau^{eff}_{Pb}(1-e^{-(\lambda_{Pb}+\alpha_{Pb})t_{TR}}))$$

where m_j is the voxal mass given by $\rho d_T a^2$, ρ is the tissue density, d_T is the section thickness and a is the side of the pixel. α_{Pb} was calculated by a measurement of the ^{212}Pb leakage for each tumor. The asymptotic dose was calculated by changing the integral limit to $t \to \infty$ that gives:

$$Dose^{asy}_{\alpha}(BiPo;j,t_{TR}) = \frac{E_{\alpha}(BiPo)}{m_j}\frac{\Gamma^j_{Pb}(t_{TR})}{e^{-\lambda_{Ra}t_{TR}}-e^{-(\lambda_{Pb}+\alpha_{Pb})t_{TR}}}(\tau_{Ra}-\tau^{eff}_{Pb})$$

The normalized asymptotic dose was calculated by dividing the asymptotic dose by the initial ^{220}Rn release rate from the source.

Distribution pattern analysis

As discussed in sections 5.2.1 and 5.3 the dose distribution pattern is determined by the isotopes diffusion and convection inside the tissue. In order to get a general idea regarding these processes in different tumors we first calculated the effective diameter for dose exceeding 10 Gy by using the dose patterns measured in each tumor. Then, we choose the sections with the longest effective diameter, assuming that their original location was at the source midplan. For this sections, we calculated the effective diffusion lengths of ^{212}Pb and ^{220}Rn and tried to estimate the drift effect.

- *Effective diameter calculation* - The effective diameter corresponding to a specific dose D_0 was calculated by summing all the pixels inside the section contour with a dose higher than D_0. The total area $A(dose > D_0)$ was then inserted into the equation defining the effective diameter:

$$D_{eff} = 2\sqrt{\frac{A(dose > D_0)}{\pi}}$$

The effective diameter was calculated for the asymptotic and normalized asymptotic

dose image of each section. Also, it was calculated for various number of iterations, which is the parameter used in applying the Lucy-Richardson deconvolution algorithm.

- *Estimating the effective ^{212}Pb and ^{220}Rn diffusion lengths*- The effective diffusion length was calculated by analyzing the statistical properties of the dose. A few steps were conducted for each section

  - **Calculation of the dose properties at various distances from the source**- For each section, the location of the source was estimated by calculating the center of gravity of the most active pixels. The asymptotic dose map was then sampled inside the external contour along circles surrounding the source at regular angular intervals (1^0). At each radial distance from the source, we calculated the mean value of the dose distribution, its median, 68% confidence interval and 95% confidence interval.
  - **Calculation of the background noise and limitation of the dose calculation results** - The image obtained by the image reader was created by a signal originating in the isotopes radioactive decay and by a signal originating in the background radiation. The latter signal depends on many parameters that may change for different experiments such as the exposure time, the exposure location and the light intensity during the positioning of the measured slides over the fuji plate. Therefore, the estimation of the noise was done separately for each tumor section analysis. First, a region in the fuji image located near but outside the tumor section contour was selected. Then, a cumulative histogram of the PSL values inside this region was calculated. The threshold was selected as the PSL value below which 90% of the values were located. The curves describing the mean and median dose were then limited to values higher than the selected threshold.
  - **Fitting the dose curve by the diffusion-leakage model** - The curve describing the median value of the asymptotic dose as a function of the radial distance from the source was fitted by the diffusion-leakage model, which was used to calculate the asymptotic dose generated by the source across its midplane. The calculation relied on the measured ^{224}Ra activity, the effective ^{212}Pb desorption probability and the calculated ^{212}Pb leakage probability. This left the ^{220}Rn and ^{212}Pb effective diffusion lengths as adjustable parameters in most cases. In some cases, where the values obtained were not realistic, the ^{220}Rn diffusion length was set to be 0.2 or 0.3 mm and only the ^{212}Pb diffusion length remained as an adjustable parameter. Fitting was performed over a typical ra-

dial range starting at 0.3-0.5 mm from the source and ending where the activity values became lower than the determined noise threshold.

- *Estimating the effective velocity inside the tumor* - In order to estimate the drift effect in the tumor, the ratio between the long axis and the axis perpendicular to the long axis of 10 and 100 Gy isodose curves was calculated for each section. The long axis was determined by the following algorithm :

  - The isodose curves for 10 Gy was extracted from the calculated dose distribution
  - A straight line that crossed the source location was drawn from each point on the curve to a second point located on the other side of the curve ("A")
  - A second straight line perpendicular to the first line and crossing the source location was drawn between two other points on the isodose curve ("B")
  - Four lines parallel to "A" and crossing "B" were added at various distances from "A"
  - The sum of the "A" and the four line lengths was calculated
  - The long axis was determined to be the "A" line for which the calculated total length was maximal

  This algorithm was chosen since it allows an intuitive identification of a drift direction. For illustration of this phenomenon and the selected algorithm results see figure 5.12.

5.4.3 HRA experiments results

In this section we present the entire set of experimental results for the SQ2, PANC02 and LL2 tumors which have undergone the HRA analysis process. For each tumor, we present the calculated dose maps, the results of fitting the data with the diffusion-leakage model, the correlation between calculated dose and the tissue damage and the results of the long axis search algorithm. In addition to the results obtained for each tumor we present the integrated results. First, we compare the normalized asymptotic dose of two representative tumors from each tumor type . Second, the effective diameter for different dose levels is shown as a function of the initial ^{220}Rn release rate. Finally, the average asymptotic dose as a function of the distance from the source for each tumor type is presented.

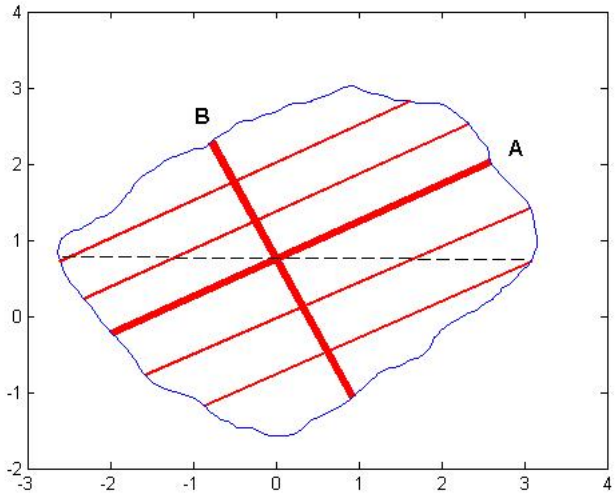

Figure 5.12: The long axis (A) and the axis perpendicular to the long axis (B) determined for a 10 Gy isodose curve (the blue line) measured in a treated tumor. The black dotted line is the longest calculated A line.

5.4.4 Discussion

The data gathered in HRA experiments shows that the radiation distribution pattern is different in different tumor types. It can be easily observed in the asymptotic and normalized asymptotic dose images that the radiation distribution in SQ2 tumors is much wider than in PANC02 tumors. Also, the radiation distribution in LL2 tumors is more similar to that of SQ2 tumors than to that of PANC02 tumors. In addition to the images, the effective diameters and the diffusion lengths calculated for each tumor section demonstrate the differences between the tumors. The effective diameters range between 1-3 mm in PANC02 tumors and between 3.2-6 mm in SQ2 tumors. The ^{212}Pb diffusion lengths calculated in PANC02 tumors range between 0.1-0.3 mm and between 0.5-1 mm in SQ2 tumors. Similar diffusion length values were calculated for additional SQ2 tumors in a previous work conducted by L. Arazi [14]. Also, the effective diameters of SQ2 tumors presented in figure 5.28 include tumors measured in the current research and in L. Arazi research.

The diffusion-leakage model provides a good description for the average dose fields measured in all tumor types. This agrees with the relatively low values calculated for the ratio between the long axis and its perpendicular axis in different tumor sections. These results imply that the movement of the radioactive atoms inside the tumor is dominated by diffusion and that the convection part can be incorporated into an effective diffusion coefficient. Still, it is important to remember that at this time our knowledge regarding the blood and fluid flows effect on the radioisotopes movement is very limited. Theoretically,

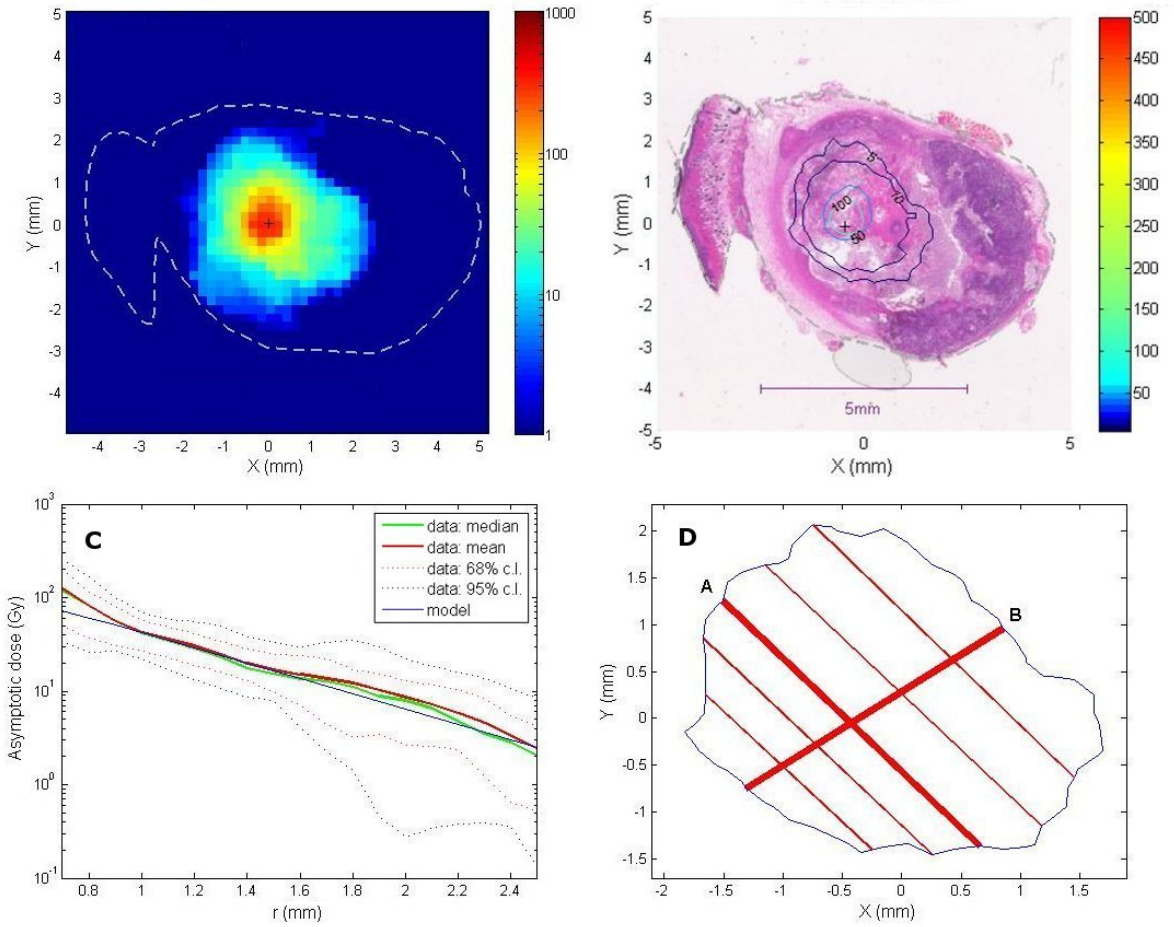

Figure 5.13: Experiment HRA-SQ2-1. The SQ2 tumor was removed 3.8 days after being treated with a 0.92 μCi ^{224}Ra source (P_{des}(Rn)=0.33). The tumor mass after removal was 695 mg. The calculated ^{212}Pb leakage probability is 0.47. (A) The calculated asymptotic dose (logarithmic scale) (b) The calculated isodose curves (from source insertion to removal) overlaid on the stained section (c) The average and the median values of the asymptotic dose sampled over circles centered on center of gravity of the most active region. Also shown are the 68% and 95% confidence intervals. The median dose curve is fitted by the diffusion-leakage model with L_{Rn} and L_{Pb} as the adjustable parameters, resulting in L_{Rn}= 0.39 mm and L_{Pb}= 0.57 mm. (d) The long axis and the axis perpendicular to the long axis obtained for the 10Gy isodose curve (extracted from the asymptotic dose). The ratio between the axes is 1.2.

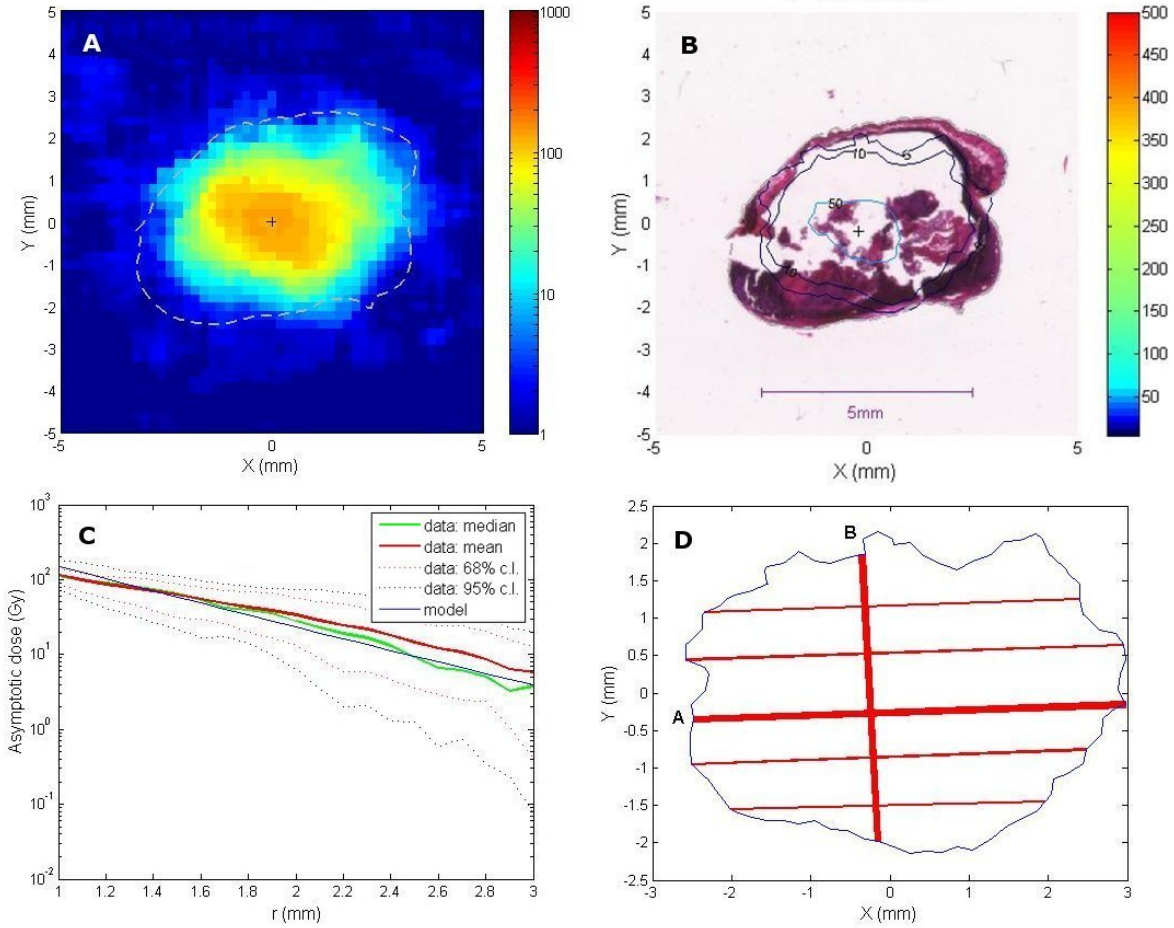

Figure 5.14: Experiment HRA-SQ2-2. The SQ2 tumor was removed 3.6 days after being treated with a 0.65 μCi ^{224}Ra source (P_{des}(Rn)=0.28). The tumor mass after removal was 417 mg. The calculated ^{212}Pb leakage probability is 0.53. (A) The calculated asymptotic dose (logarithmic scale) (b) The calculated isodose curves (from source insertion to removal) overlaid on the stained section. The section was almost completely destroyed as a result of the staining procedure (c) The average and the median values of the asymptotic dose sampled over circles centered on center of gravity of the most active region. Also shown are the 68% and 95% confidence intervals. The median dose curve is fitted by the diffusion-leakage model with L_{Rn} set as 0.3 mm and L_{Pb} as the adjustable parameters, resulting in L_{Pb}= 1.03 mm. (d) The long axis and the axis perpendicular to the long axis obtained for the 10Gy isodose curve (extracted from the asymptotic dose). The ratio between the axes is 1.43.

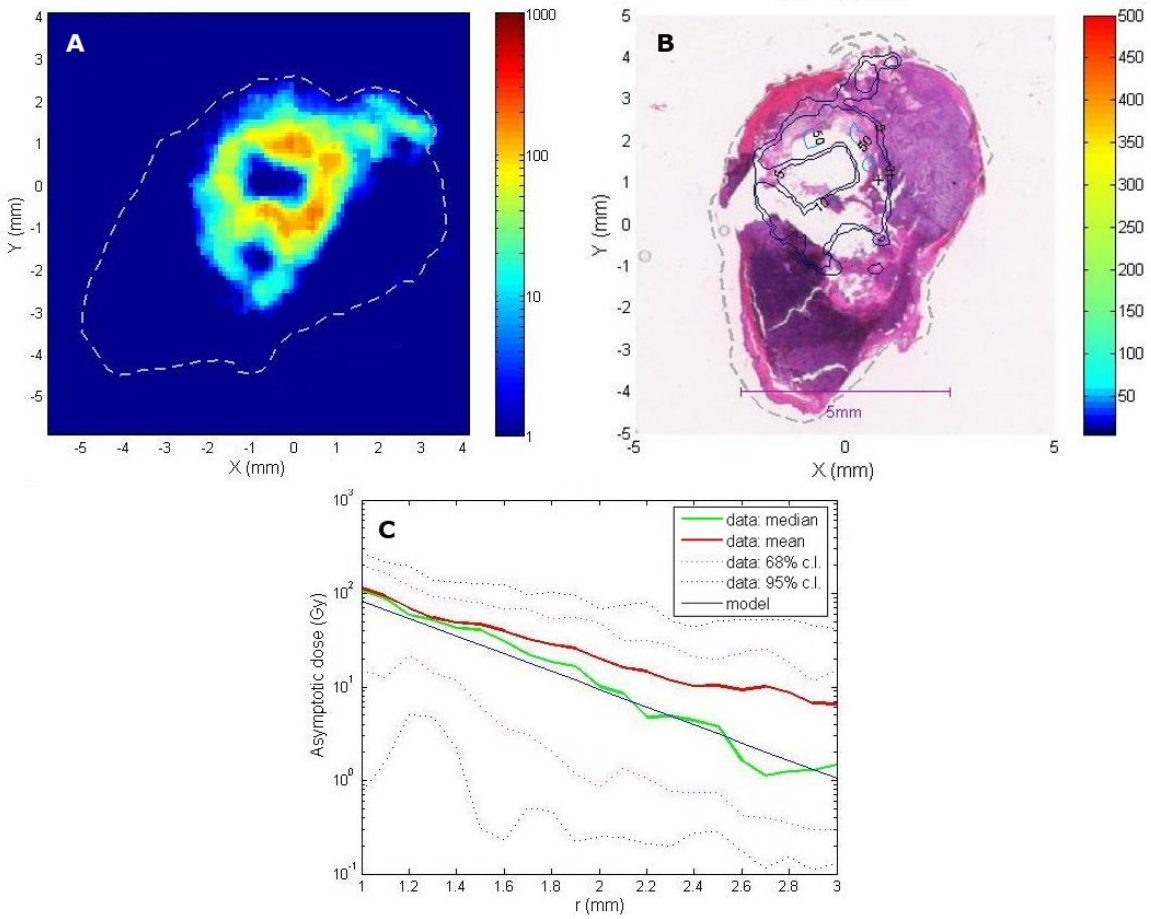

Figure 5.15: Experiment HRA-SQ2-3. The SQ2 tumor was removed 3.8 days after being treated with a 0.63 μCi ^{224}Ra source (P_{des}(Rn)=0.33). The tumor mass after removal was 728 mg. The calculated ^{212}Pb leakage probability is 0.32. (A) The calculated asymptotic dose (logarithmic scale) (b) The calculated isodose curves (from source insertion to removal) overlaid on the stained section (c) The average and the median values of the asymptotic dose sampled over circles centered on center of gravity of the most active region. Also shown are the 68% and 95% confidence intervals. The median dose curve is fitted by the diffusion-leakage model with L_{Rn} and L_{Pb} as the adjustable parameters, resulting in L_{Rn}= 0.37 mm and L_{Pb}= 0.48 mm. (d) The long axis and the axis perpendicular to the long axis were not calculated since the isodose curve obtained for 10Gy was not ellipsoid shaped.

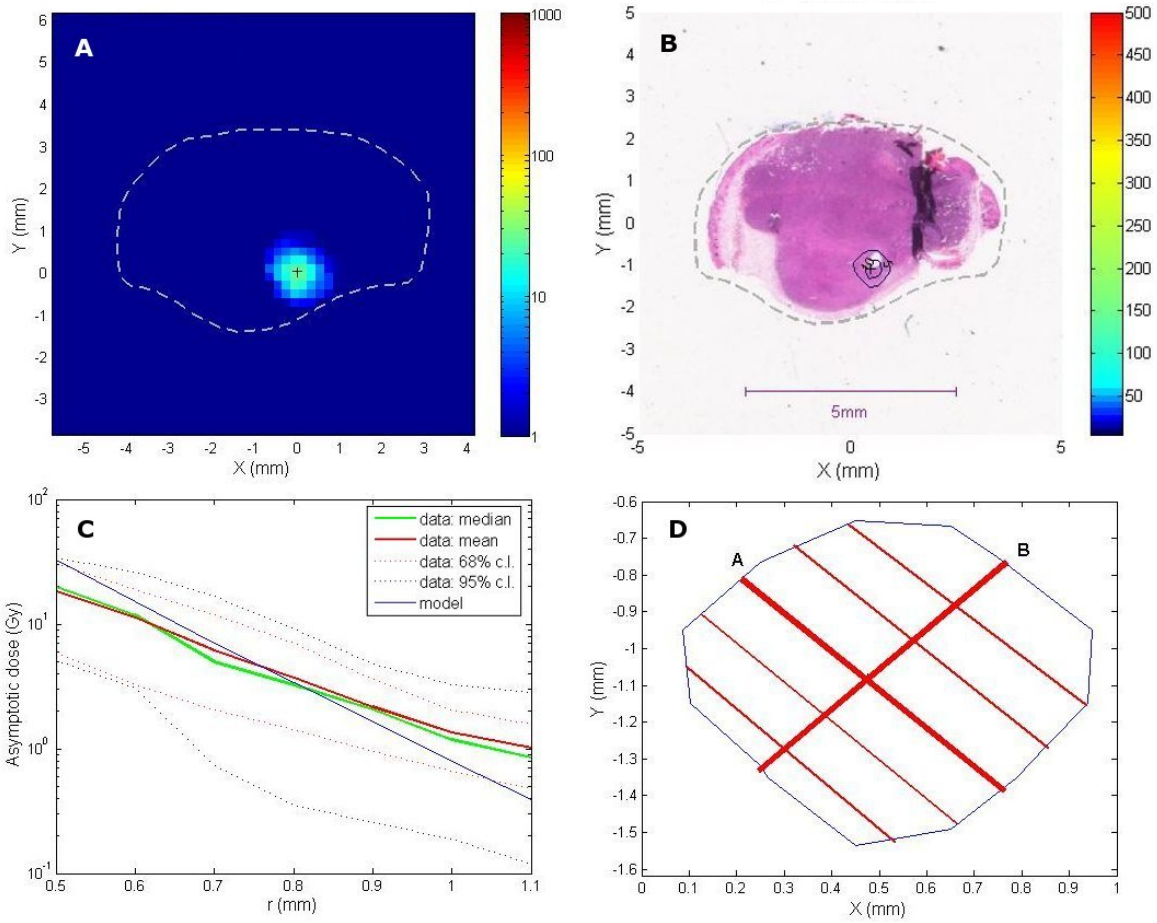

Figure 5.16: Experiment HRA-PANC02-1. The PANC02 tumor was removed 3.9 days after being treated with a 0.58 μCi ^{224}Ra source (P_{des}(Rn)=0.25). The tumor mass after removal was 174 mg. The calculated ^{212}Pb leakage probability is 0.77. (A) The calculated asymptotic dose (logarithmic scale) (b) The calculated isodose curves (from source insertion to removal) overlaid on the stained section (c) The average and the median values of the asymptotic dose sampled over circles centered on center of gravity of the most active region. Also shown are the 68% and 95% confidence intervals. The median dose curve is fitted by the diffusion-leakage model with L_{Rn} and L_{Pb} as the adjustable parameters, resulting in L_{Rn}= 0.15 mm and L_{Pb}= 0.08 mm. (d) The long axis and the axis perpendicular to the long axis obtained for the 10Gy isodose curve (extracted from the asymptotic dose). The ratio between the axes is 1.06.

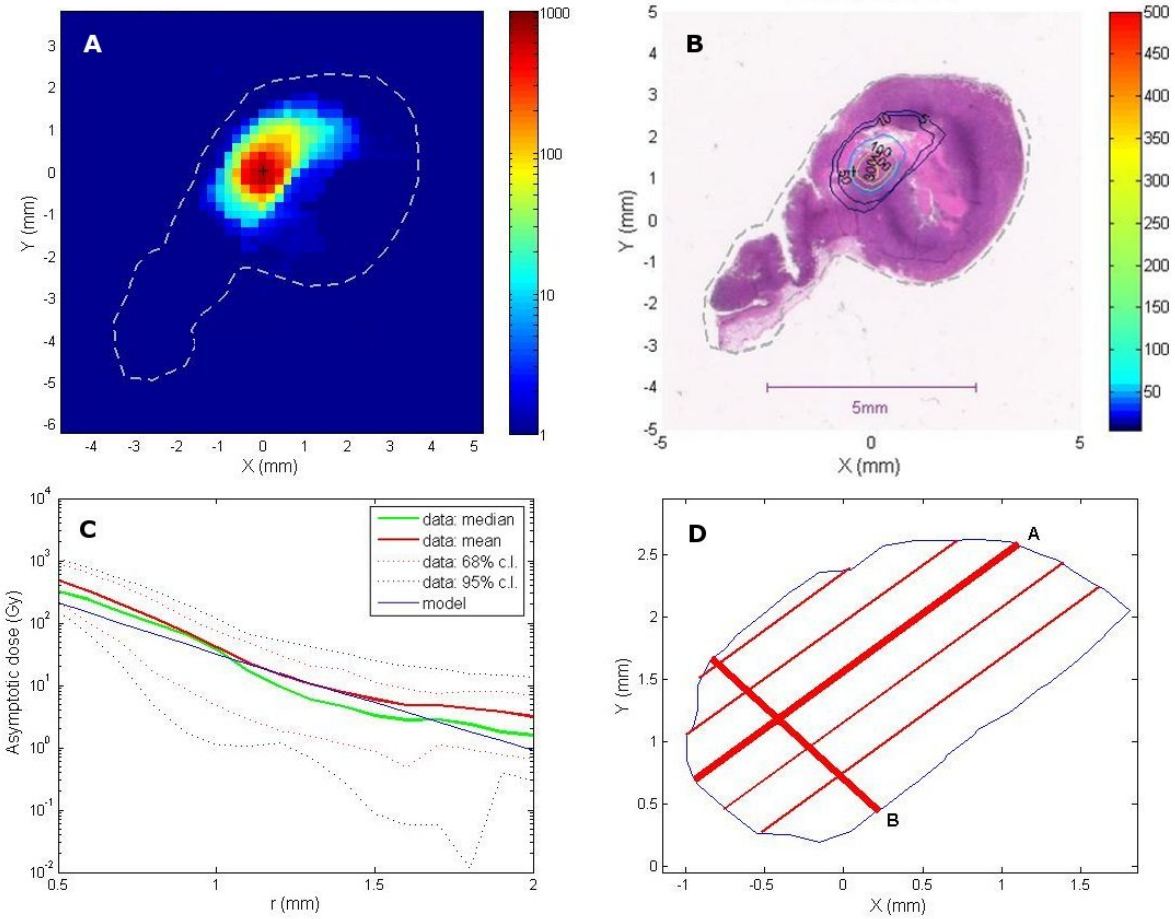

Figure 5.17: Experiment HRA-PANC02-2. The PANC02 tumor was removed 3.7 days after being treated with a 1.01 μCi ^{224}Ra source (P_{des}(Rn)=0.25). The tumor mass after removal was 208 mg. The calculated ^{212}Pb leakage probability is 0.72. (A) The calculated asymptotic dose (logarithmic scale) (b) The calculated isodose curves (from source insertion to removal) overlaid on the stained section (c) The average and the median values of the asymptotic dose sampled over circles centered on center of gravity of the most active region. Also shown are the 68% and 95% confidence intervals. The median dose curve is fitted by the diffusion-leakage model with L_{Rn} and L_{Pb} as the adjustable parameters, resulting in L_{Rn}= 0.16 mm and L_{Pb}= 0.29 mm. (d) The long axis and the axis perpendicular to the long axis obtained for the 10Gy isodose curve (extracted from the asymptotic dose). The ratio between the axes is 1.73.

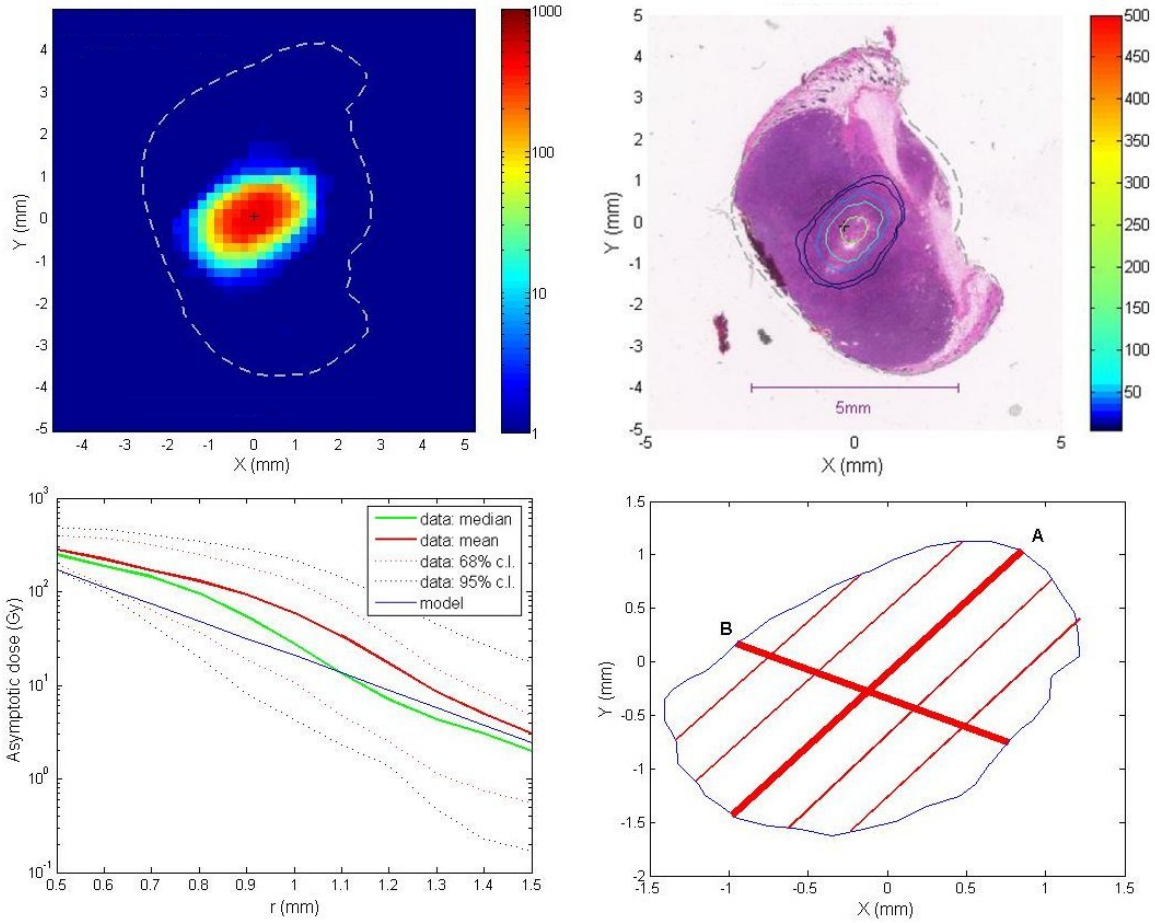

Figure 5.18: Experiment HRA-PANC02-3. The PANC02 tumor was removed 3.9 days after being treated with a 0.47 μCi ^{224}Ra source (P_{des}(Rn)=0.39). The tumor mass after removal was 365 mg. The calculated ^{212}Pb leakage probability is 0.55. (A) The calculated asymptotic dose (logarithmic scale) (b) The calculated isodose curves (from source insertion to removal) overlaid on the stained section (c) The average and the median values of the asymptotic dose sampled over circles centered on center of gravity of the most active region. Also shown are the 68% and 95% confidence intervals. The median dose curve is fitted by the diffusion-leakage model with L_{Rn} and L_{Pb} as the adjustable parameters, resulting in L_{Rn}= 0.2 mm and L_{Pb}= 0.24 mm. (d) The long axis and the axis perpendicular to the long axis obtained for the 10Gy isodose curve (extracted from the asymptotic dose). The ratio between the axes is 1.4.

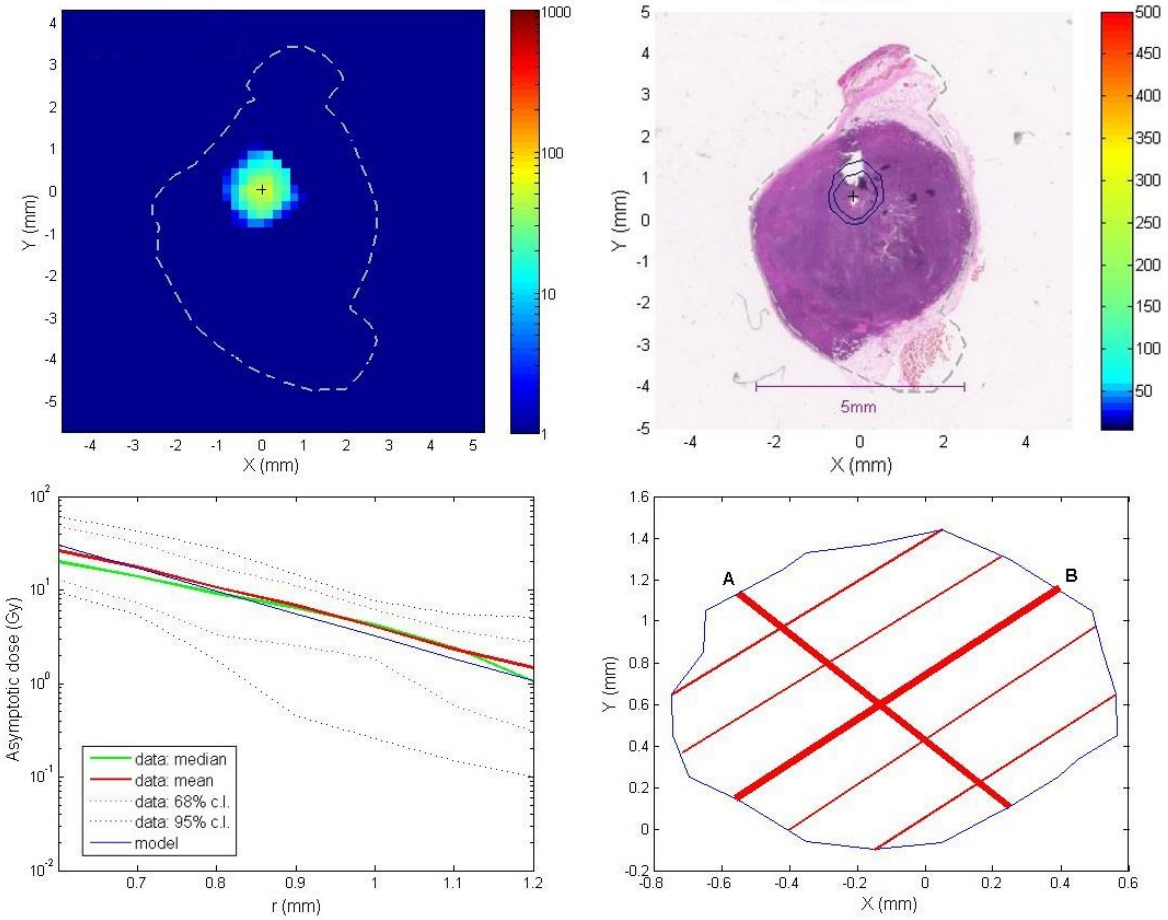

Figure 5.19: Experiment HRA-PANC02-4. The PANC02 tumor was removed 3.9 days after being treated with a 0.39 μCi ^{224}Ra source (P_{des}(Rn)=0.4). The tumor mass after removal was 194 mg. The calculated ^{212}Pb leakage probability is 0.74. (A) The calculated asymptotic dose (logarithmic scale) (b) The calculated isodose curves (from source insertion to removal) overlaid on the stained section (c) The average and the median values of the asymptotic dose sampled over circles centered on center of gravity of the most active region. Also shown are the 68% and 95% confidence intervals. The median dose curve is fitted by the diffusion-leakage model with L_{Rn} fixed to be L_{Rn}= 0.2 mm and L_{Pb} as the adjustable parameter, resulting in and L_{Pb}= 0.1 mm. (d) The long axis and the axis perpendicular to the long axis obtained for the 10Gy isodose curve (extracted from the asymptotic dose). The ratio between the axes is 1.1.

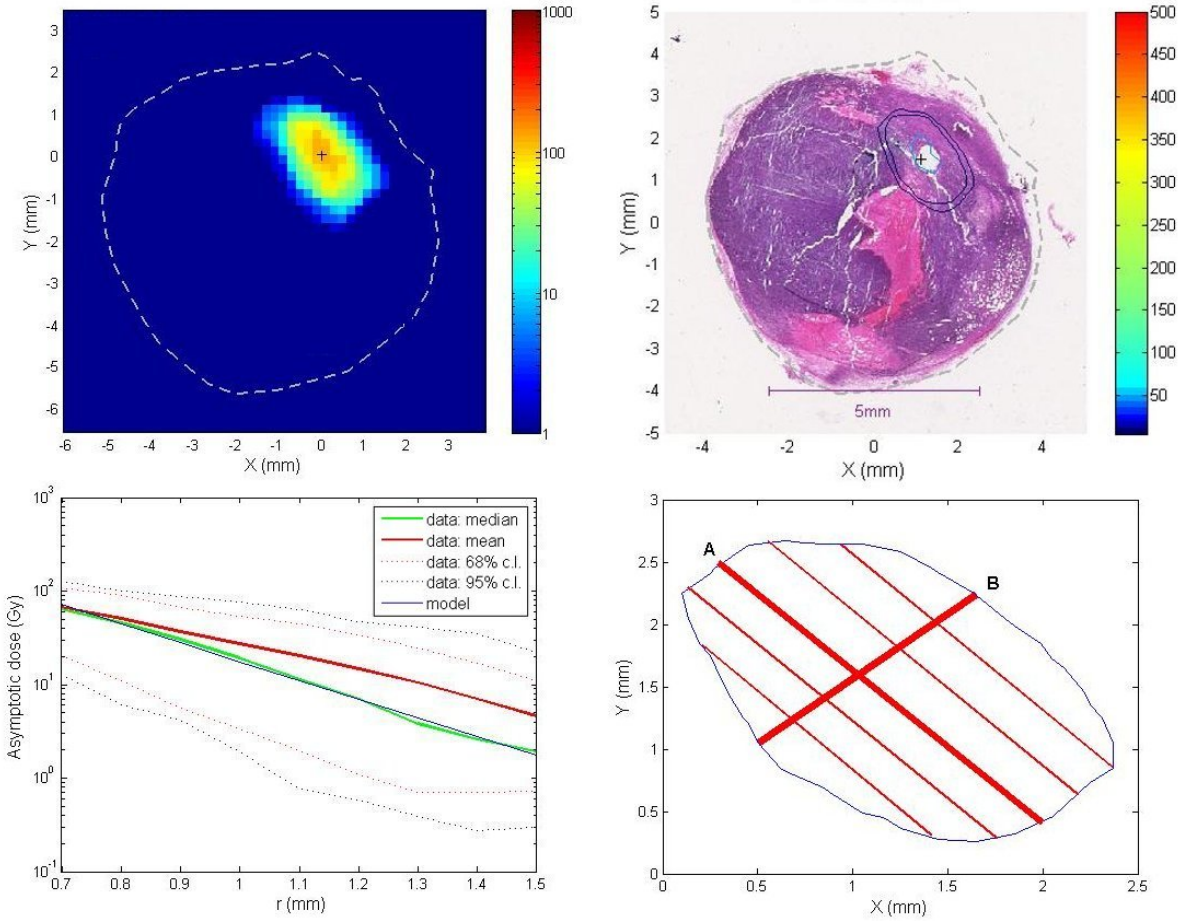

Figure 5.20: Experiment HRA-PANC02-5. The PANC02 tumor was removed 4.03 days after being treated with a 0.99 μCi ^{224}Ra source (P_{des}(Rn)=0.44). The tumor mass after removal was 490 mg. The calculated ^{212}Pb leakage probability is 0.69. (A) The calculated asymptotic dose (logarithmic scale) (b) The calculated isodose curves (from source insertion to removal) overlaid on the stained section (c) The average and the median values of the asymptotic dose sampled over circles centered on center of gravity of the most active region. Also shown are the 68% and 95% confidence intervals. The median dose curve is fitted by the diffusion-leakage model with L_{Rn} and L_{Pb} as the adjustable parameters, resulting in L_{Rn}= 0.24 mm and L_{Pb}= 0.1 mm. (d) The long axis and the axis perpendicular to the long axis obtained for the 10Gy isodose curve (extracted from the asymptotic dose). The ratio between the axes is 1.5.

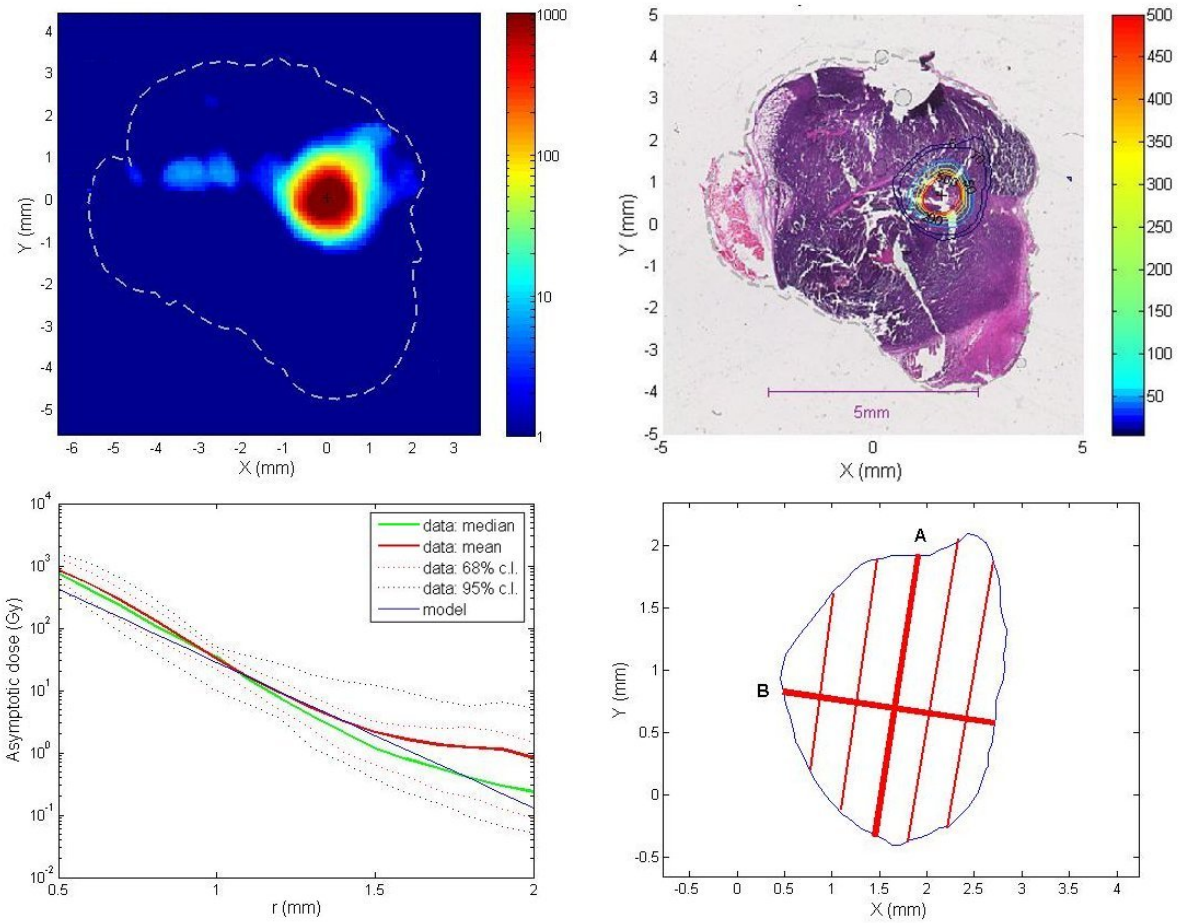

Figure 5.21: Experiment HRA-PANC02-6. The PANC02 tumor was removed 3.7 days after being treated with a 1.51 μCi ^{224}Ra source (P_{des}(Rn)=0.34). The tumor mass after removal was 700 mg. The calculated ^{212}Pb leakage probability is 0.6. (A) The calculated asymptotic dose (logarithmic scale) (b) The calculated isodose curves (from source insertion to removal) overlaid on the stained section (c) The average and the median values of the asymptotic dose sampled over circles centered on center of gravity of the most active region. Also shown are the 68% and 95% confidence intervals. The median dose curve is fitted by the diffusion-leakage model with L_{Rn} and L_{Pb} as the adjustable parameters, resulting in L_{Rn}= 0.13 mm and L_{Pb}= 0.2 mm. (d) The long axis and the axis perpendicular to the long axis obtained for the 10Gy isodose curve (extracted from the asymptotic dose). The ratio between the axes is 1.3.

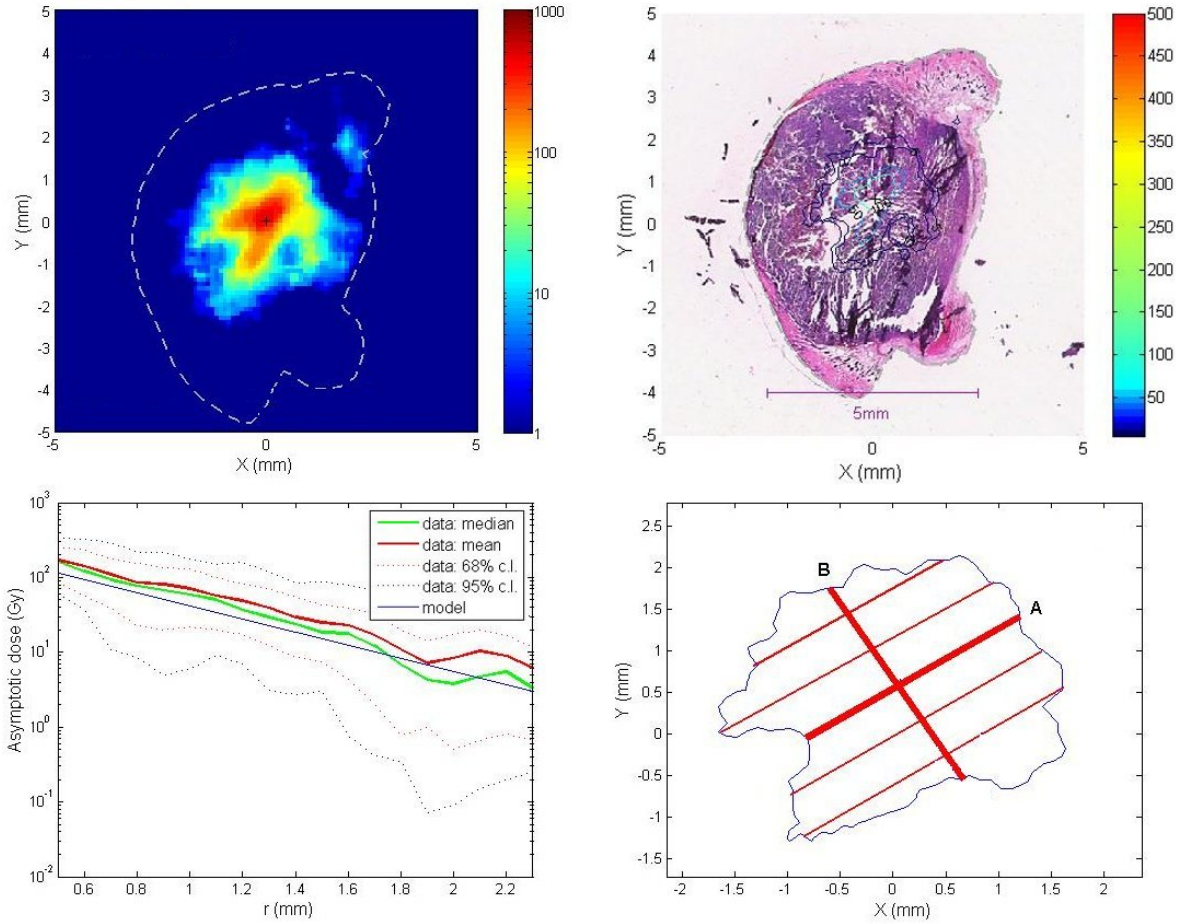

Figure 5.22: Experiment HRA-LL2-1. The LL2 tumor was removed 3.3 days after being treated with a 0.64 μCi ^{224}Ra source (P_{des}(Rn)=0.34). The tumor mass after removal was 492 mg. The calculated ^{212}Pb leakage probability is 0.68. (A) The calculated asymptotic dose (logarithmic scale) (b) The calculated isodose curves (from source insertion to removal) overlaid on the stained section (c) The average and the median values of the asymptotic dose sampled over circles centered on center of gravity of the most active region. Also shown are the 68% and 95% confidence intervals. The median dose curve is fitted by the diffusion-leakage model with L_{Rn} and L_{Pb} as the adjustable parameters, resulting in L_{Rn}= 0.36 mm and L_{Pb}= 0.54 mm. (d) The long axis and the axis perpendicular to the long axis obtained for the 10Gy isodose curve (extracted from the asymptotic dose). The ratio between the axes is 1.05.

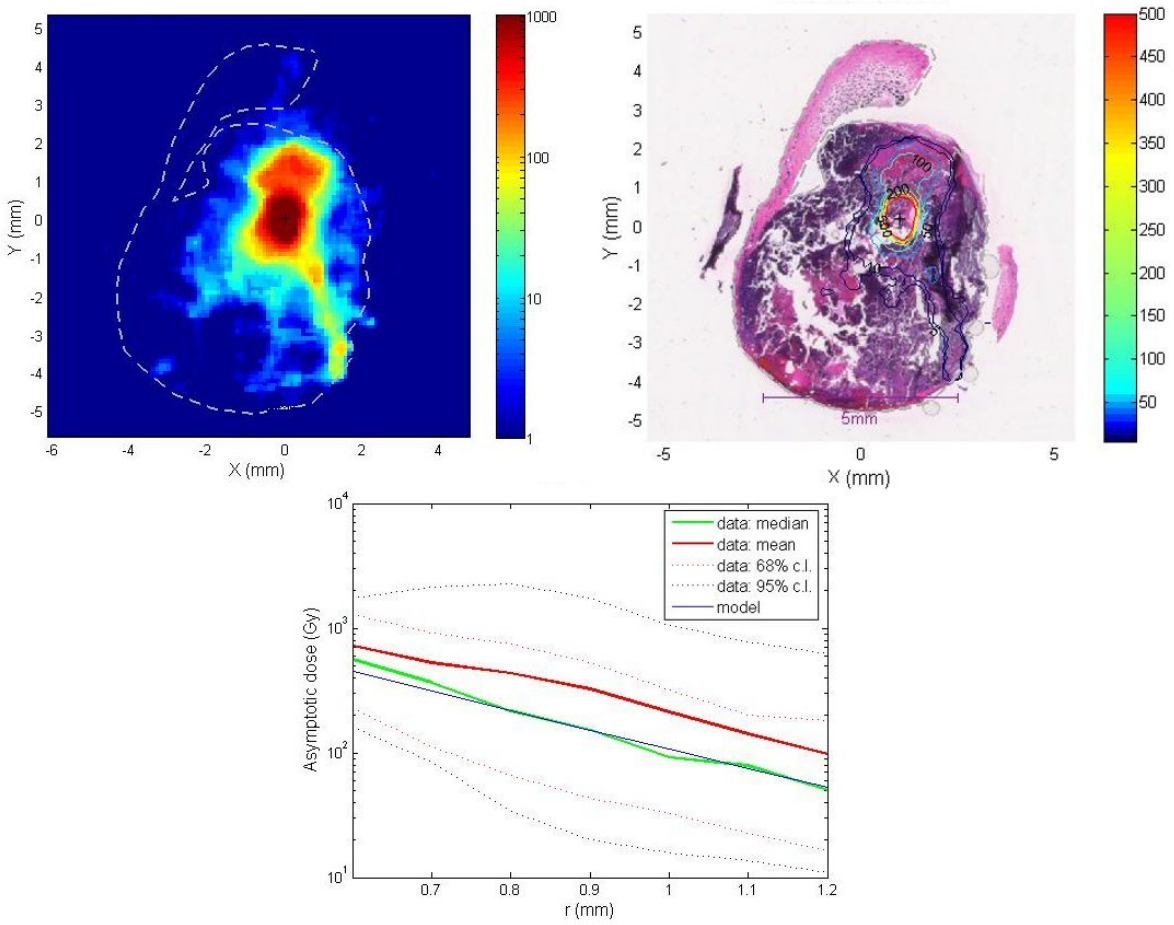

Figure 5.23: Experiment HRA-LL2-2. The LL2 tumor was removed 3.9 days after being treated with a 1.55 μCi ^{224}Ra source (P_{des}(Rn)=0.37). The tumor mass after removal was 1051 mg. The calculated ^{212}Pb leakage probability is 0.45. (A) The calculated asymptotic dose (logarithmic scale) (b) The calculated isodose curves (from source insertion to removal) overlaid on the stained section (c) The average and the median values of the asymptotic dose sampled over circles centered on center of gravity of the most active region. Also shown are the 68% and 95% confidence intervals. The median dose curve is fitted by the diffusion-leakage model with L_{Rn} fixed to be L_{Rn}= 0.3 mm and L_{Pb} as the adjustable parameters, resulting in and L_{Pb}= 0.23 mm. (d) The long axis and the axis perpendicular to the long axis were not calculated since the isodose curve obtained for 10Gy was not ellipsoid shaped.

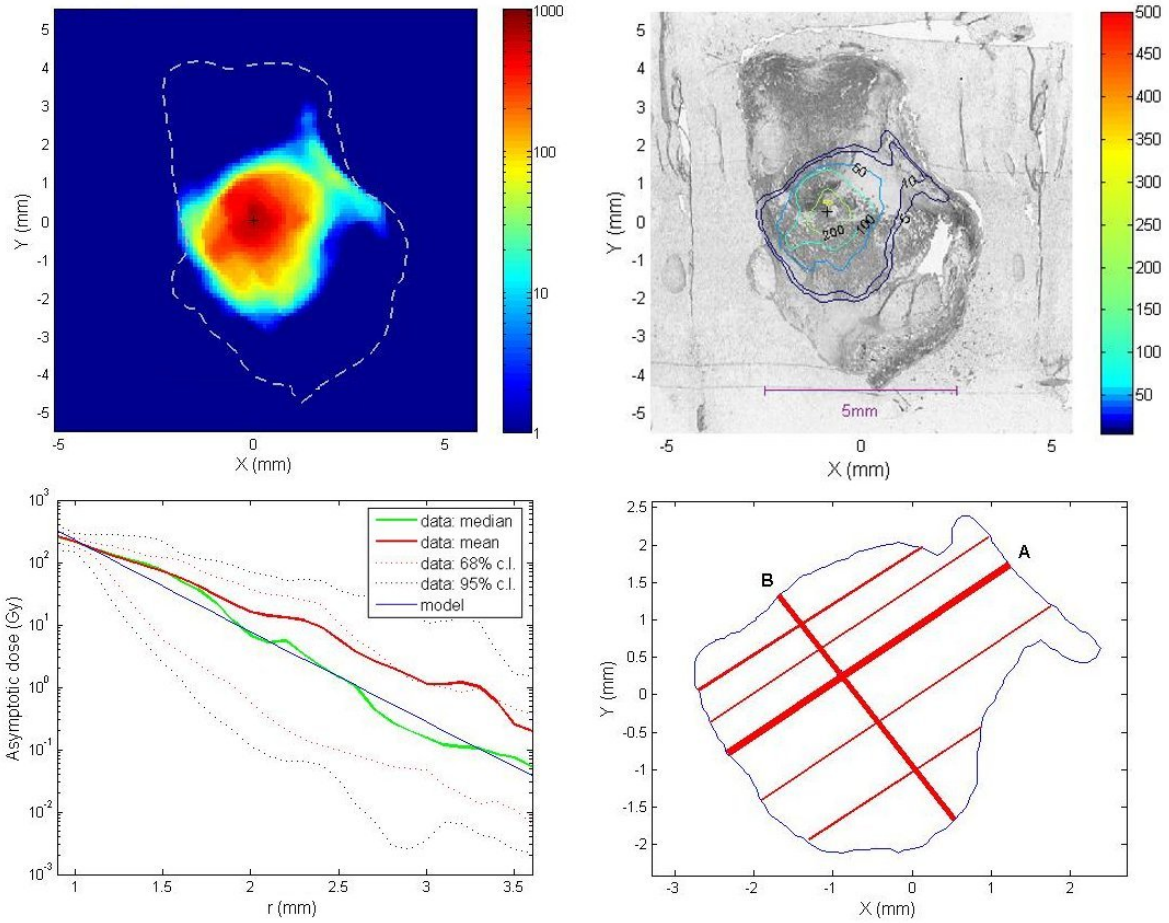

Figure 5.24: Experiment HRA-LL2-3. The LL2 tumor was removed 3.7 days after being treated with a 1.07 μCi ^{224}Ra source (P_{des}(Rn)=0.36). The tumor mass after removal was 753 mg. The calculated ^{212}Pb leakage probability is 0.27. (A) The calculated asymptotic dose (logarithmic scale) (b) The calculated isodose curves (from source insertion to removal) overlaid on the original section. In this case, the staining procedure did'nt succeded and the section was totally destroyed (c) The average and the median values of the asymptotic dose sampled over circles centered on center of gravity of the most active region. Also shown are the 68% and 95% confidence intervals. The median dose curve is fitted by the diffusion-leakage model with L_{Rn} and L_{Pb} as the adjustable parameters, resulting in L_{Rn}= 0.29 mm and L_{Pb}= 0.34 mm. (d) The long axis and the axis perpendicular to the long axis obtained for the 10Gy isodose curve (extracted from the asymptotic dose). The ratio between the axes is 1.2.

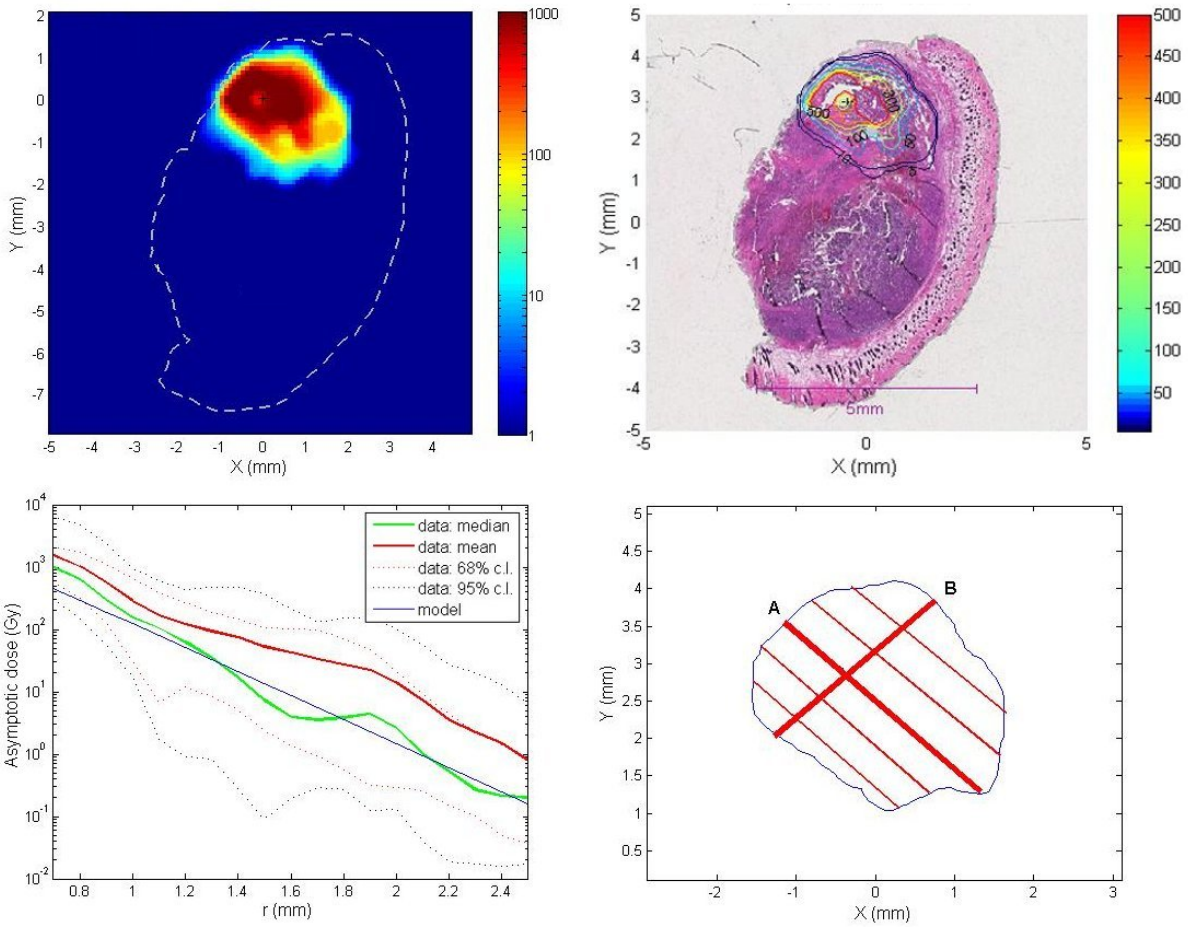

Figure 5.25: Experiment HRA-LL2-4. The LL2 tumor was removed 3.6 days after being treated with a 2.65 μCi ^{224}Ra source (P_{des}(Rn)=0.43). The tumor mass after removal was 712 mg. The calculated ^{212}Pb leakage probability is 0.52. (A) The calculated asymptotic dose (logarithmic scale) (b) The calculated isodose curves (from source insertion to removal) overlaid on the stained section (c) The average and the median values of the asymptotic dose sampled over circles centered on center of gravity of the most active region. Also shown are the 68% and 95% confidence intervals. The median dose curve is fitted by the diffusion-leakage model with L_{Rn} and L_{Pb} as the adjustable parameters, resulting in L_{Rn}= 0.2 mm and L_{Pb}= 0.23 mm. Note that in this tumor the source was very close to the tumor periphery. It is therefore reasonable that these diffusion lengths are short in comparison to the 'real' lengths. (d) The long axis and the axis perpendicular to the long axis obtained for the 10Gy isodose curve (extracted from the asymptotic dose). The ratio between the axes is 1.25.

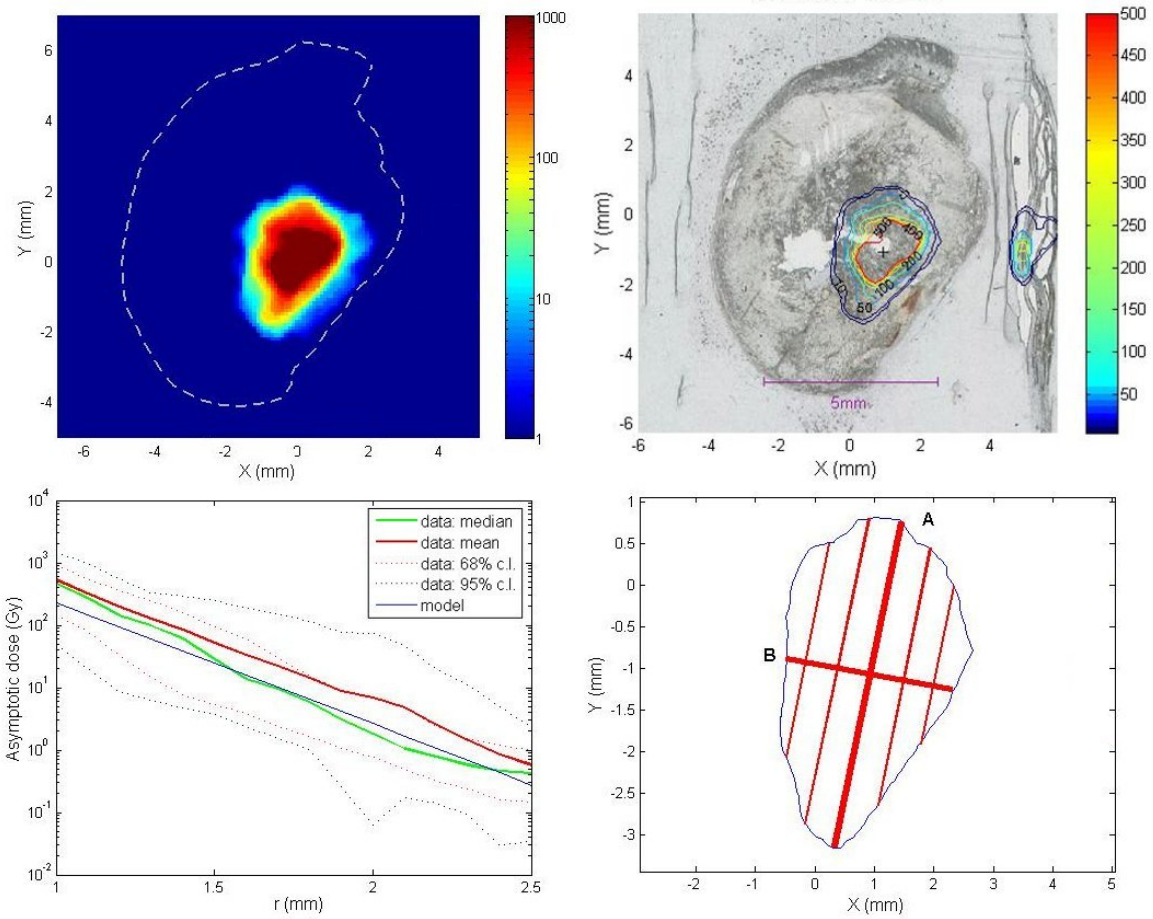

Figure 5.26: Experiment HRA-LL2-5. The LL2 tumor was removed 3.6 days after being treated with a 2.98 μCi ^{224}Ra source (P_{des}(Rn)=0.43). The tumor mass after removal was 1170 mg. The calculated ^{212}Pb leakage probability is 0.2. (A) The calculated asymptotic dose (logarithmic scale) (b) The calculated isodose curves (from source insertion to removal) overlaid on the original tumor section. In this case, the staining procedure did'nt succeded and the section was totally destroyed (c) The average and the median values of the asymptotic dose sampled over circles centered on center of gravity of the most active region. Also shown are the 68% and 95% confidence intervals. The median dose curve is fitted by the diffusion-leakage model with L_{Rn} and L_{Pb} as the adjustable parameters, resulting in L_{Rn}= 0.2 mm and L_{Pb}= 0.22 mm. Note that in this tumor the source was very close to the tumor periphery. It is therefore reasonable that these diffusion lengths are short in comparison to the 'real' lengths. (d) The long axis and the axis perpendicular to the long axis obtained for the 10Gy isodose curve (extracted from the asymptotic dose). The ratio between the axes is 1.9.

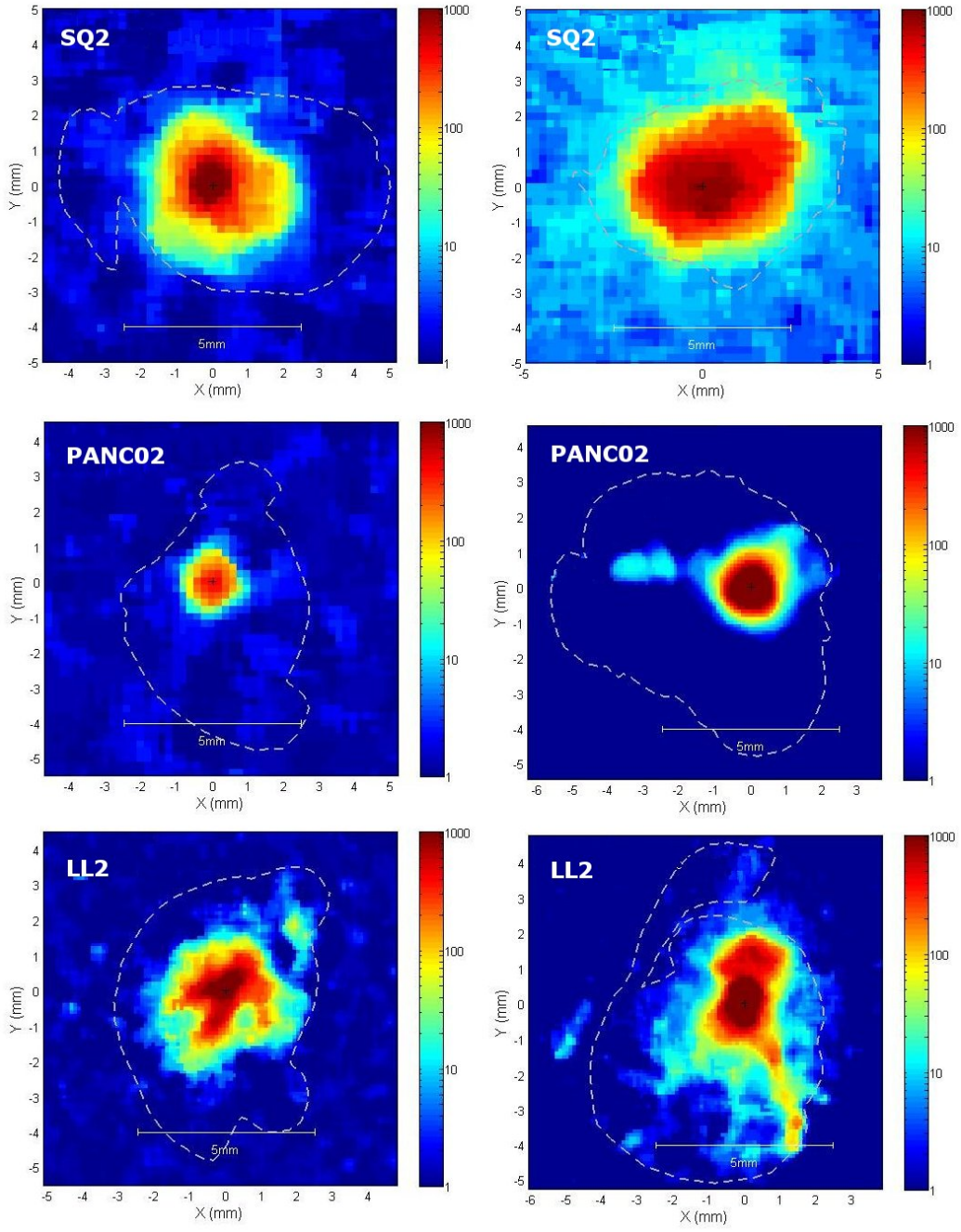

Figure 5.27: The calculated normalized asymptotic dose (Gy) for representetive sections of each tumor type. The sections were taken from (From top left to buttom right): hra-SQ2-1, hra-SQ2-2, hra-PANC02-4, hra-PANC02-6, hra-LL2-1, hra-LL2-2.

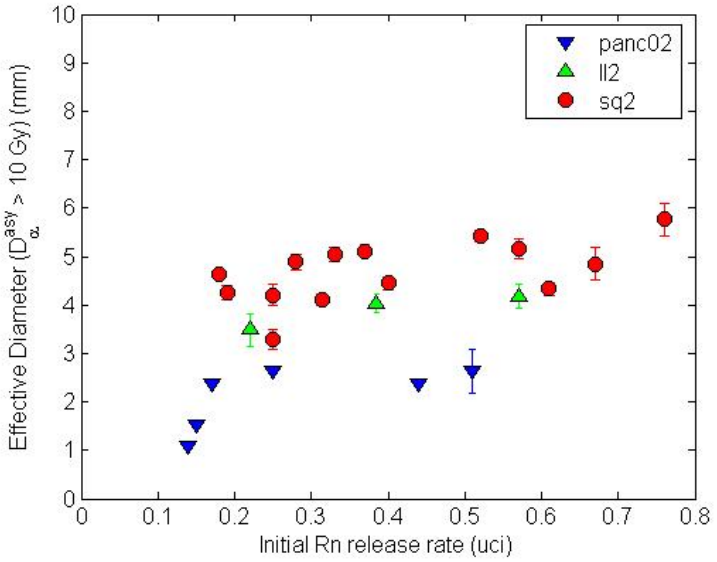

Figure 5.28: The effective diameters corresponding to an asymptotic ^{212}Bi/^{212}Po alpha particle dose exceeding 10 Gy as a function of the initial ^{220}Rn release rate from the source for different tumor types.

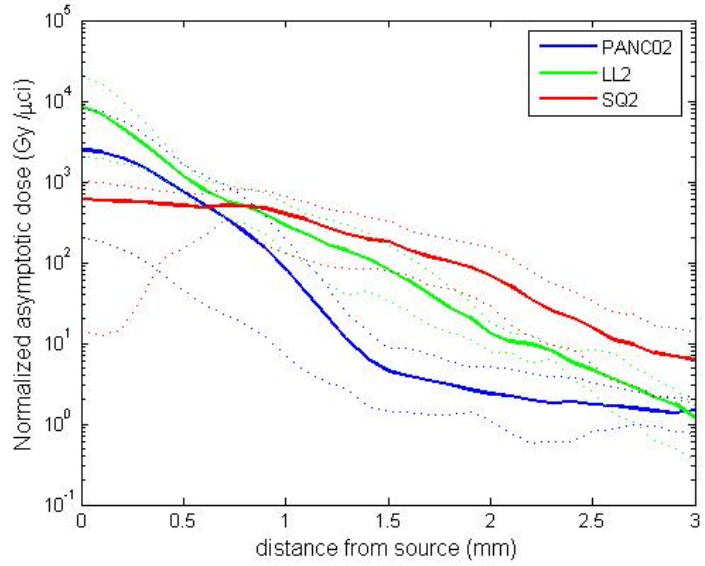

Figure 5.29: Integrated results of the normalized asymptotic ^{212}Bi/^{212}Po dose as a function of the radial distance from the source. Shown are the mean values of the normalized dose for each tumor type as well as the 95% confidence interval.

this effect might vary between different tumors leading to high effective diffusion coefficients in tumors in which the flows enhance the radionuclides distribution in the tumor and to a lower coefficient when the effect is negligible. Therefore, in order to have a better estimate of the blood and fluid flows effect, additional measurements of the tumor properties should be conducted.

The necrotic damage observed in the treated tumors generally correlates with the radiation distribution pattern. As discussed in chapter 4 the necrotic damage in PANC02 tumors before and after treatment is very limited in comparison to SQ2 tumors. This corresponds to the radiation distribution pattern which is limited in PANC02 tumors in comparison to SQ2 tumors. This phenomena supports the assumption made in chapter 4 regarding the relation between the diffusion coefficient and tissue viability. It seems that the movement of the diffusing atoms is easier inside a necrotic tissue. Moreover, a wider spread in necrotic tissue leads to an increase in the necrotic area which again helps to an easier movement of the radionuclides in the tissue. It is therefore very reasonable to assume that these two processes, radionuclide transport and tissue necrosis, are inter-related.

This explanation raises a question regarding the linearity of the processes occurring inside the tumor. The effective diameter calculation is based on a single measurement taken from each tumor assuming that the diffusion of the radionuclides inside the tumor does not depend on the source activity or on the duration of treatment. However, the real processes inside the tumor might depend on these parameters. The validity of this assumption was examined in the work of L. Arazi with regard to SQ2 tumors [14]. No difference was found between the effective diameters that were calculated for tumors treated for different durations or with different source activities. Figure 5.30 shows a similar examination of the effective diameter corresponding to the normalized asymptotic dose of different tumor types treated with different source activities. It is shown that for all tumor types, the effective diameter is relatively constant as a function of the source activity.

The differences found between radiation distribution patterns in different tumor types can be the result of many factors, in addition to those already suggested. One of them is the difference in tumor cell sensitivity to alpha radiation. In a study that was conducted in parallel to this research the relative sensitivity of different tumor cell lines to alpha radiation was examined in vitro. The results showed that of all cell lines compared (among which were SQ2 and PANC02), the SQ2 cells appeared to be the most sensitive to alpha radiation. These results may imply, that the inter-relation between the tissue necrosis and the radionuclide transport inside the tumor is more complex than suggested. In addition to the difficulty involved in the atoms movement inside a viable tissue in comparison to a necrotic tissue, the formation of the necrotic area in panc02 tumors requires a higher amount of radiation than in SQ2 tumors. This is another possible explanation for the limited distribution detected in PANC02 tumors compared to SQ2 tumors.

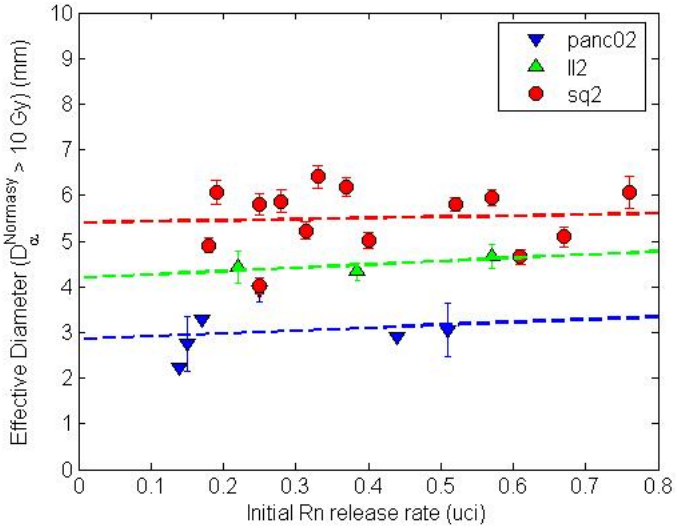

Figure 5.30: The effective diameter corresponding to the normalized asymptotic ^{212}Bi/^{212}Po alpha particle dose exceeding 10 Gy as a function of the initial ^{220}Rn release rate from the source for different tumor types. The data is fitted with a linear curve, whose slope is 0.25 for SQ2, 0.72 for LL2 and 0.59 for PANC02.

Chapter 6

DART safety - activity measurements in the organs

Treating cancer with DART sources may lead to various side effects. These effects will probably be the result of the leakage of radioactive isotopes out of the tumor and an uptake of these isotopes in different organs inside the body. As explained in chapter 3, we can safely assume that isotopes with a short half-life do not leave the tumor and decay inside it (^{220}Rn, ^{216}Po). ^{212}Pb, in contrast, leaks out of the tumor during the treatment and as will be shown below, concentrates in different organs or leaves the body with secretions. With regard to ^{212}Bi, we assume that its atoms are in secular equilibrium with ^{212}Pb atoms inside the tumor, and that they leave the tumor in secular equilibrium too. Finally, we assume that less then 0.5% of the total source ^{224}Ra activity is shed from the source into the tumor. This amount is negligible in comparison to ^{212}Pb activity cleared from the tumor and therefore we disregard it.

In this chapter we present the preclinical data gathered from mice on the uptake of the leaking ^{212}Pb atoms in various organs. First, we treat the uptake of ^{212}Pb atoms in selected organs after different treatment times. Then we present the uptake in these organs as measured in mice bearing different tumor types.

It can be assumed that DART treatment in human cancer will result in different ^{212}Pb uptake in organs than that found in mice. This is due to many possible reasons such as the organs size, its size in relation to the whole body and its molecular composition. Still, the phenomena shown in the mice preclinical data are very relevant for human cancer treatment too. They should be taken into account in the future, when considering DART safety aspects as part of treatment planning.

6.1 Measurements of the ^{212}Pb activity in mice organs

During the experiments for ^{212}Pb leakage measurements (described in chapter 3) several organs were taken out of the mice for measurement in the gamma counter in addition to the tumor and the source. The organs - kidney, spleen, liver and leg were usually taken from the treated mice. In several cases lung and a blood sample of about 300 μl were taken too. All organs except for the blood were excised after the mouse was sacrificed. The blood sample was taken after tumor removal, while the mouse was under anesthesia.

The excised organs were weighed and inserted into a capped scintillation vial taken for gamma measurements. Each sample was measured for several times over a period of 24-72 hours. The measurement results were analyzed using the procedure described in chapter 2 in order to get the sample ^{224}Ra and ^{212}Pb activity content at tumor removal time.

6.2 ^{212}Pb uptake probability in organs for different treatment times

6.2.1 Experimental data

The data on ^{224}Ra and ^{212}Pb activities in mice organs was gathered during the experiments described in chapter 3 conducted on mice bearing SQ2 tumors treated for different time periods. Organs were taken from 18 mice treated for two days, 7 mice treated for four days and 3 mice treated for eight days. In these experiments the tumor activity was measured and the ^{212}Pb leakage probability calculated. Also, the source and the organs activities were measured.

6.2.2 Data analysis

In order to enable a comparison between the organ activities of different mice treated for varying times with different source activities we define the ^{212}Pb uptake probability of an organ at time t. It represents the instantaneous probability that a ^{212}Pb atom is found in an organ after leaving the tumor. The uptake probability is given by:

$$P_{uptake}^{organ}(t) = \frac{\Gamma_{Pb}^{organ}(t)}{\Gamma_{Pb}^{leak}(t)}$$

where $\Gamma_{Pb}^{leak}(t)$ is the total ^{212}Pb activity that leaked out of the tumor at time t and $\Gamma_{Pb}^{organ}(t)$ is the measured ^{212}Pb activity at the organ at the same time. $\Gamma_{Pb}^{leak}(t)$ is calculated by multiplying the instantaneous ^{212}Pb leaking fraction at time t with the total ^{212}Pb activity released from the source into the tumor. The experimental data was gathered from tumors

that were treated for 2-8 days. Therefore, it is assumed that the system is in equilibrium and $\Gamma_{Pb}^{leak}(t)$ is given by:

$$\Gamma_{Pb}^{leak}(t) = f_{Pbleak}(t) \cdot (1.14\Gamma_{Ra}^{src}(t) - \Gamma_{Pb}^{src}(t))$$

6.2.3 Results

Figure 6.1 shows the uptake probability of the liver, the kidney and the spleen as a function of the instantaneous ^{212}Pb leaking fraction at different treatment ending times. The organs were taken from mice bearing SQ2 tumors. The uptake probability of each organ was calculated at the tumor removal time.

Three interesting phenomena are apparent in these figures:

- The ^{212}Pb uptake probability of an organ depends on the ^{212}Pb leakage probability from the tumor. The uptake probability in the liver and the kidneys very clearly increases as the instantaneous ^{212}Pb leaking fraction increases for all treatment times. This trend also exists for the spleen, though it is less significant.
- The ^{212}Pb uptake probability of an organ for a specific instantaneous ^{212}Pb leaking fraction is similar at different treatment times.
- The highest uptake probability of ^{212}Pb atoms is in the kidneys. The next organ with a relatively high uptake is the liver. The other organs show relatively low uptake, which is of the same order of magnitude in all of them.

6.2.4 Discussion

The dependence of the ^{212}Pb uptake probability of an organ on the ^{212}Pb leakage probability from the tumor is quite surprising. Intuitively we would expect that the probability of a single atom that leaked out of the tumor to reach a specific organ and stay in it, to be constant, as long as the organ does not reach saturation. Since the amount of leaking ^{212}Pb atoms is very small, it is very unlikely that saturation has been reached during our experiments.

However, further analysis of the processes occurring in the tumor during DART treatment may lead to a reasonable explanation of this phenomenon. As explained in chapter 3 we assume that during its stay in the tumor, the ^{212}Pb atom interacts with the tissue proteins and forms various new molecules. It is very reasonable that the characteristic stay time of ^{212}Pb atom inside the tumor influences the probability for the creation of such molecules. We suggest that a longer stay of ^{212}Pb atom inside the tumor, or in other words - lower probability for the leakage of ^{212}Pb atoms outside of the tumor - will result in the

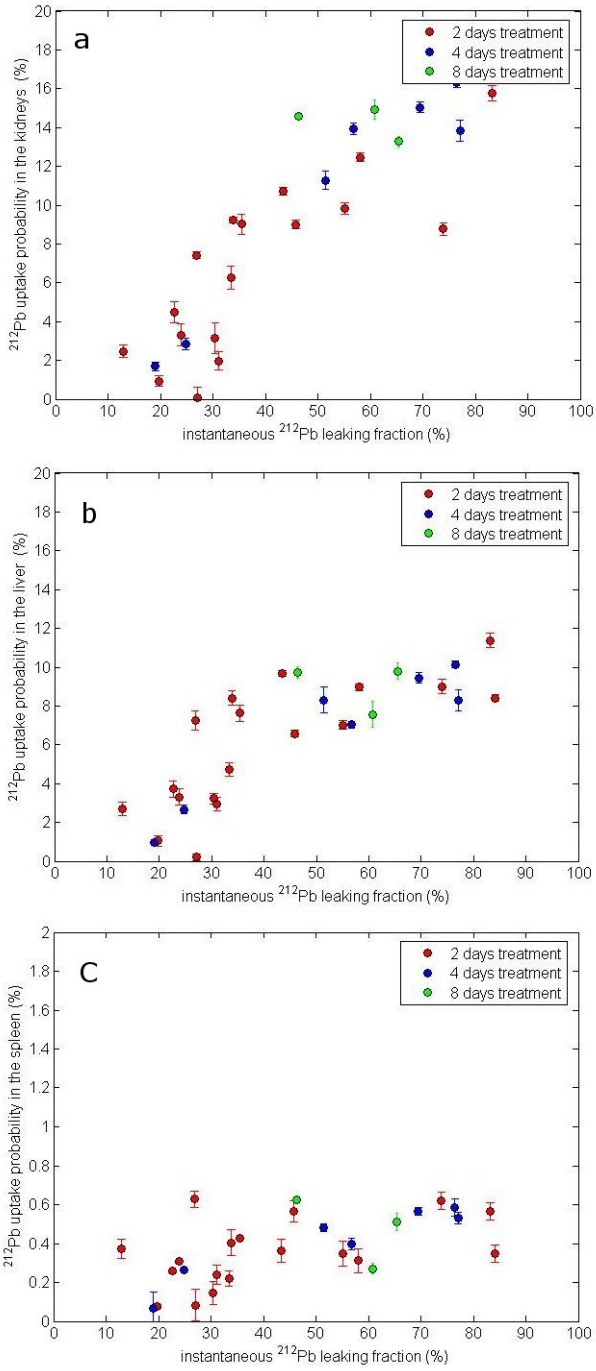

Figure 6.1: The uptake probability of different organs as a function of the instantaneous ^{212}Pb leaking fraction for different treatment times. (a) The uptake probability of the kidneys (b) The uptake probability of the liver (c) The uptake probability of the spleen

creation of many new molecules composed of proteins and ^{212}Pb atoms in the tissue. In such a case, the probability that ^{212}Pb leaves the tumor as part of a complex molecule is high. On the contrary, when ^{212}Pb atom stays inside the tumor with a short characteristic time, we assume the probability that it leaves the tumor as a single atom is high. It is because it does not have enough time to interact with proteins inside the tumor.

Keeping this suggestion in mind we now turn to an interesting piece of information obtained in studies regarding lead bio-availability in animals. According to various works the intracellular bio-availability of lead (Pb) at low dosage levels in major target organs such as the kidney and the brain appears to be largely determined by its complexation with different proteins. For example, it has been shown that lead binding proteins in rats are capable of attenuating the binding of lead to specific proteins in the blood and mediating its movement and chromatin binding to target cells in the kidney [3].

This result together with our suggestion regarding the different leakage forms of ^{212}Pb out of the tumor provides a good explanation to the described phenomenon. We assume that when the ^{212}Pb leakage probability is high, ^{212}Pb leaves the tumor as a single atom and therefore its probability to bind to the relevant molecules in each organ is high . Similarly, when the ^{212}Pb leakage probability is low, it leaves the tumor within a complex molecule and therefore its uptake probability in the organs is low.

With regard to the high uptake of ^{212}Pb in the liver and the kidneys at various times, this result agrees with studies reported in the literature [21]. According to this studies the liver and the kidneys show a substantially higher concentration of lead than most soft tissues. Data on injected lead in human subjects, baboons and beagles indicates that the liver rapidly accumulates 10-15% of the systemic lead and loses much of it within a few weeks. Results of studies in dogs and rodents indicate that the kidneys may accumulate as much as 15-20% of injected lead within a few hours and that a substantial portion of the early accumulation is reabsorbed or lost in urine within a few hours.

The temporal behavior of ^{212}Pb in the mouse is somewhat different than that quoted in the literature. In contrast to the relatively fast removal of ^{212}Pb from the kidneys of dogs and rodents, the high concentration of lead in mice kidneys as a result of the DART treatment still remains after 8 days. There may be various reasons for this difference. First, in our model ^{212}Pb leaks out of the tumor continually, in contrast to the examples quoted. Also, the difference between mouse organs and other animals may lead to different uptake rates and percentages. Regarding the ^{212}Pb uptake in the liver, though we do not have enough information to determine the exact removal and uptake rates, it seems that the behavior in mice is more similar to the quoted information. As shown, after 8 days, the ^{212}Pb concentration in the mice liver is still high as observed in other animals.

The general information regarding ^{212}Pb behavior in mice as a result of the DART treatment is important for future safety considerations of the treatment. The order of

magnitude measured for ^{212}Pb leakage in different tumors and the resulting absorption in organs can be used in order to calculate the limitations and the consequences of treatment with a single or with multiple sources.

6.3 ^{212}Pb activity in organs of mice bearing different tumor types

6.3.1 Experimental data

The data on ^{224}Ra and ^{212}Pb activities in organs of mice bearing different tumor types was gathered during the experiments described in chapter 3 and 5. All mice were treated for 4 days. Organs were taken from 6 BALB/c male mice bearing SQ2 tumors, 6 B57BI/6 female mice bearing PANC02 tumors and 6 B57BI/6 male mice bearing LL2 tumors. Each tumor activity was measured and the ^{212}Pb leakage probability calculated. The source and the organs activities were also measured. The Pb uptake in each organ was calculated by dividing $P_{uptake}^{organ}(t)$ (defined above) by the organ mass.

6.3.2 Results

Figure 6.2 shows the ^{212}Pb uptake probability per unit mass in the liver, kidney, spleen, leg, lung and blood as a function of the instantaneous ^{212}Pb leaking fraction. Three graphs are plotted, each for a different tumor bearing mouse. The uptake probability of each organ was calculated at tumor removal time.

The three graphs shows that the dependence of the ^{212}Pb uptake probability on the ^{212}Pb leakage probability from the tumor exists only in mice bearing SQ2 tumors and not in mice bearing PANC02 or LL2 tumors. The relative uptake of different organs, however, is similar in all mouse types. The high ^{212}Pb uptake per unit mass in the kidneys and blood is observed in all the graphs, together with the relatively low uptake in the liver, spleen, leg and lung. The absolute values of the^{212}Pb uptake probability per unit mass measured in the organs are similar in all mouse types.

6.3.3 Discussion

The differences observed between the ^{212}Pb uptake probability in organs of mice bearing different tumor types may have many reasons, of which we shall consider the two main ones. First, as explained throughout this work, there are many differences between SQ2, PANC02 and LL2 tumors beginning with their size and ending with their tissue composition. Also, as discussed in the previous section, we have good reasons to assume that ^{212}Pb uptake in the organs depends on the way that it leaves the tumor. ^{212}Pb uptake in the

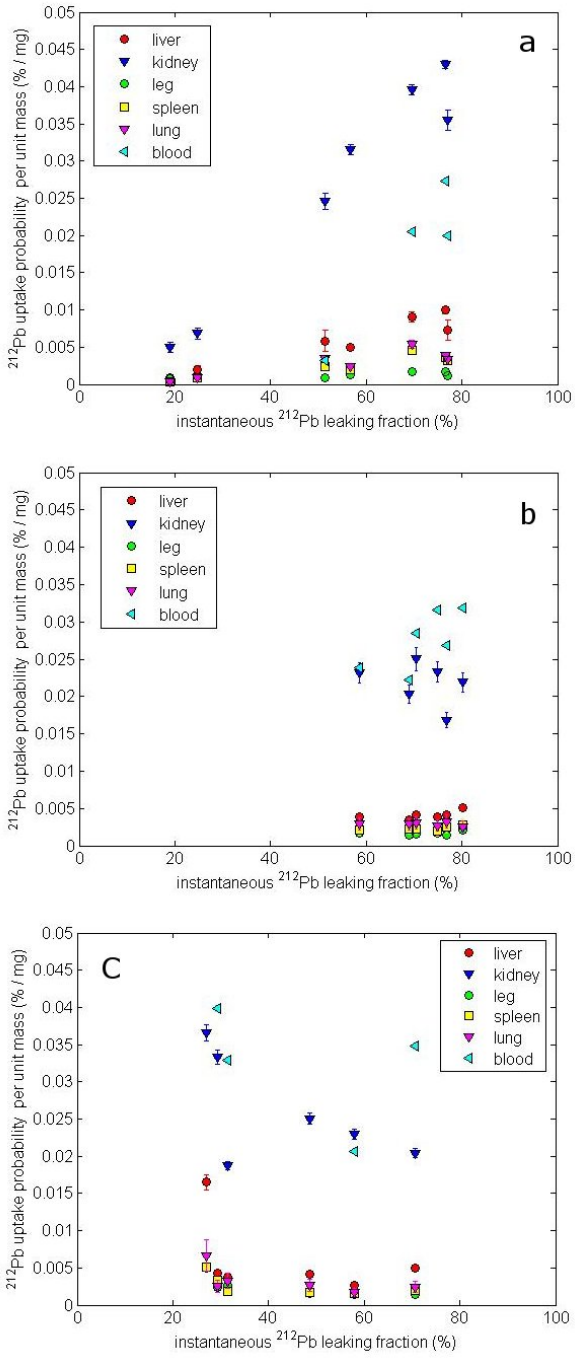

Figure 6.2: The ^{212}Pb uptake probability per unit mass in the liver, kidney, spleen, leg, lung and blood as a function of the instantaneous ^{212}Pb leaking fraction for different tumor bearing mice (a) organs from mice bearing SQ2 tumors (b) organs from mice bearing PANC02 tumors (c) organs from mice bearing LL2 tumors

kidneys, for example, is higher when it arrives as a single atoms than when it is part of a complex molecule. Therefore, the first possible explanation to the detected difference is that ^{212}Pb leaves different tumors in different forms as a result of their composition and the characteristic removal rate.

As detailed above, there are three different mice types involved in this experiment - one for each tumor type. A second reason for the observed difference may result from the organs itself. Organ properties such as size and molecular composition may be different for different mice. Such differences might influence the probability of ^{212}Pb uptake in the tissue. The existence of ^{212}Pb binding proteins in the tissue, for example, would enable lead uptake in the tissue while in their absence less or no uptake will occur.

Bibliography

[1] Jahne B, Heinz G, and Dietrich W. Measurement of the diffusion coefficients of sparingly soluble gases in water. *Journal of Geophysical Research*, 92:10767–10776, 1987.

[2] Fowler B.A. Roles of lead-binding proteins in mediating lead bioavailability. *Environ Health Perspect*, 106:1585–1587, 1998.

[3] Fowler B.A. Roles of lead-binding proteins in mediating lead bioavailability. *Environ Health Perspect*, 106:1585–1587, 1998.

[4] Bremer C, Mustafa M, Bogdanov A.J., Ntziachristos V, Petrovsky A, and Weissleder R. Steady-state blood volume measurements in experimental tumors with different angiogenic burdens–a study in mice. *Radiology*, 226:214–220, 2003.

[5] Eisenberg D.P., Adusumilli P.S., Hendershott K.J., Yu Z, Mullerad M, Chan M.K., Chou T.C., and Fong Y. 5-fluorouracil and gemcitabine potentiate the efficacy of oncolytic herpes viral gene therapy in the treatment of pancreatic cancer. *Journal of Gastrointestinal Surgery*, 9:1068–1079, 2005.

[6] Goodhead D.T. Mechanisms for the biological effectiveness of high-let radiations. *J Radiat Res (Tokyo)*, 40:1–13, 1999.

[7] Hall E.J., Gross W, Dvorak R.F., Kellerer A.M., and Rossi H.H. Survival curves and age response functions for chinese hamster cells exposed to x-rays or high let alpha-particles. *Radiat Res*, 52(1):88–98, 1972.

[8] Horev G. Treatment of malignant pancreatic tumors by intratumoral 224-ra loaded wires releasing alpha emitting atoms combined with chemotherapy. *MasterThesis. Sackler School of Medicine, Tel Aviv University, Tel Aviv, Israel*, 2008.

[9] http://www.cancer.gov/statistics/ National Cancer Institute.

[10] Payne J.C., Horst T., Marc A., and Godwin H. A. Lead fingers; pb2+ binding to structural zinc-binding domains determined directly by monitoring lead2212-thiolate

charge-transfer bands. *Journal of the American Chemical Society*, 121:6850–6855, 1999.

[11] Jain R. K. Transport of molecules in the tumor interstitium: a review. *Cancer Res*, 47:3039–3051, 1987.

[12] Jain R. K. Determinants of tumor blood flow: A review. *Cancer Res*, 48:2641–2658, 1988.

[13] Jain R. K. Delivery of molecular and cellular medicine to solid tumors. *Journal of Controlled Release*, 53:49–67, 1998.

[14] Arazi L. Diffusing alpha-emitters radiation therapy: Theoretical and experimental dosimetry. *Ph.D thesis. School of Physics and Astronomy, Raymond and Beverly Sackler Faculty of Exact Sciences, Tel Aviv University, Israel*, 2008.

[15] Arazi L, Cooks T, Schmidt M, Keisari Y, and Kelson I. Treatment of solid tumors by interstitial release of recoiling short-lived alpha emitters. *Phys Med Biol*, 52:5025–5042, 2007.

[16] Schmidt M. Development and preparation of sources for controlled release of alpha-emitting isotopes in malignant tumors. *MaterThesis. School of Physics and Astronomy, Raymond and Beverly Sackler Faculty of Exact Sciences, Tel Aviv University, Tel Aviv, Israel*, 2005.

[17] Schmidt M. Advanced methods for dart source preparation. *Ph.D. research proposal, School of Physics and Astronomy, Raymond and Beverly Sackler Faculty of Exact Sciences, Tel Aviv University, Tel Aviv, Israel*, 2007.

[18] Luigi Preziosi, editor. *Cancer modeling and simulation.* Chapman & Hall/crc, 2003.

[19] Lide D. R., editor. *CRC handbook of chemistry and physics 88th ed.* Taylor and Francis Group, Boca Raton, FL., 2008.

[20] Wilkowski R, Thoma M, Bruns C, Wagner A, and Heinemann V. Chemoradiotherapy with gemcitabine and continuous 5-fu in patients with primary inoperable pancreatic cancer. *JOP. J Pancreas*, 7(4):349–360, 2006.

[21] Leggett R.W. An age-specific kinetic model of lead metabolism in humans. *Environ Health Perspect*, 101(7):598–616, 1993.

[22] Chary S.R. and Jain R.K. Direct measurement of interstitial convection and diffusion of albumin in normal and neoplastic tissues by fluorescence photobleaching. *Proc Natl Acad Sci U S A*, 86:5385–5389, 1989.

[23] Cooks T, Horev G, Reitkopf S, Marshak G, Arazi L, Kelson I, and Keisari Y. Intratumoral 224-ra loaded wires combined with chemotherapy can destroy solid malignant tumors of various histological types in mice, and prolong survival. *International Journal of Radiation Oncology Biology Physics*, 72:S718–S719, 2008.

[24] Cooks T, Arazi L, Efrati M, Schmidt M, Marshak G, Kelson I, and Keisari Y. Growth retardation and destruction of experimental squamous cell carcinoma by interstitial radioactive wires releasing diffusing alpha-emitting atoms. *International Journal of Cancer*, 122:1657–1664, 2008.

[25] Cooks T, Arazi L, Efrati M, Schmidt M, Marshak G, Kelson I, and Keisari Y. Interstitial wires releasing diffusing alpha emitters combined with chemotherapy improved local tumor control and survival in squamous cell carcinoma-bearing mice. *Cancer*, 115:1791 – 1801, 2009.

[26] Padera T.P., Kadambi A, Tomaso E, Carreira C.M., Brown E.B., Boucher Y, Choi N.C., Mathisen D, Wain J, Mark E.J., Munn L.L., and Jain R.K. Lymphatic metastasis in the absence of functional intratumor lymphatics. *Science*, 296:1883–1886, 2002.

[27] Boucher Y and Jain R.K. Microvascular pressure is the principal driving force for interstitial hypertension in solid tumors: implications for vascular collapse. *Cancer Res*, 52:5110–5114, 1992.

[28] Boucher Y, Baxter L. T., and Jain R. K. Interstitial pressure gradients in tissue-isolated and subcutaneous tumors: implications for therapy. *Cancer Res*, 50:4478–4484, 1990.